Eye Closure Penalty Based Signal Quality Metric for Intelligent All-Optical Networks

Jonathan C. Li

B.Sc., B.E. (Hons)

A thesis submitted in partial fulfilment of the requirements of the degree of Doctor of Philosophy

August, 2009

Department of Electrical and Electronic Engineering

The University of Melbourne

Produced on archival quality paper

Abstract

Telecommunications network operators have found that traditional optical networks are increasingly unable to cost effectively sustain the inexorable growth of the Internet. New technologies, such as dense wavelength division multiplexing (DWDM) and reconfigurable optical add drop multiplexers (ROADM) enable large capacity increases, service transparency and automated provisioning that are seen to be essential to the evolution of next generation optical networks.

New advances, however, bring new challenges. In traditional optical networks, physical layer signal quality was maintained using of optical-electrical-optical (OEO) regeneration, but the use of DWDM makes this cost ineffective. The replacement of OEO regeneration with ROADMs reduces overall cost, but introduces the need to carefully consider the end-to-end signal quality of provisioned lightpaths that are affected by multiple optical impairments.

In this thesis, a new method for combining the effects of multiple physical layer impairments in all-optical network paths, based on the eye closure penalty, is developed for use as a signal quality metric in automated network provisioning. The accuracy of the method is demonstrated, and the method is then extended to account for time-variation of physical layer impairments, and the effect of user traffic requirements.

Declaration

This is to certify that

1. the thesis comprises only my original work,
2. due acknowledgement has been made in the text to all other material used,
3. the thesis is less than 100,000 words in length, exclusive of tables, maps, bibliographies and appendices as approved by the RHD Committee.

Signature: _____

Date: _____

Acknowledgments

I acknowledge and thank my principal supervisors, Kerry Hinton, Peter Farrell and Sarah Dods, for their patience, guidance, tuition, humour, support and encouragement. In particular, Peter for providing me with the big picture insights and always making sure that the administrative side of my PhD was taken care of and Sarah for always challenging me to improve and grow. My biggest thanks go to Kerry, for always comprehensively answering my questions, no matter how elementary, hours of reading and editing my thesis and papers and providing a great weekly meeting environment.

I also acknowledge and thank my external supervisors, Milosh Ivanovich and Paul Fitzpatrick, for their years of mentoring, friendship, encouragement and insights when working back in Telstra Research Labs that have carried over into this work. Thanks to Milosh for always bringing an infectious, enthusiastic attitude and to Paul for bringing a careful eye and alternate viewpoint to every discussion.

This work would not have been possible without the financial and academic support of the NICTA Victorian Research Laboratories and the University of Melbourne. I especially thank Thas Nirmalathas, for providing me the opportunity to pursue my studies within NICTA and MAMI, and I hope I have repaid his faith in me.

I of course thank and acknowledge family and friends, particularly Mum and Dad who have always been supportive of whatever endeavours I chose to pursue, and who have instilled in me a thirst for knowledge and growth. To Aunty Karen and Grandma for helping to shape me into the person I am today. I thank all of them for their financial support and encouragement that allows me to pursue this work.

PTO…

Most importantly, I thank and acknowledge my wife, Katie, who has courageously taken this journey with me through times of uncertainty. Her caring and sacrificing nature, unreserved support and trust in me have been absolutely vital to the success of this work and my growth as a person. Final, special thanks, goes to the youngest members of our family, Ollie, whose companionship over the last three and a half years has been a welcome distraction, and to Mini-Li whose impending arrival is an absolute joy for us to look forward to.

Table of Contents

1 General Introduction

1.1 Optical Networking

It is an exciting time of unprecedented growth in the world of telecommunications. Demand for bandwidth and connectivity to support evolving user requirements, such as high bandwidth video, mobile internet, online gaming, enterprise VPNs and computational clustering amongst others, has driven the need for more agile and cost-effective optical networks [1].

The deployment of reconfigurable optical add-drop multiplexers (ROADMs) [2] is an important step in realising such networks. ROADMs enable the routing and multiplexing of traffic channels (wavelengths) into, or out of, optical fibres without the need for costly electrical signal regeneration. Importantly, ROADMs can be remotely configured and reconfigured, allowing an operator the flexibility to easily alter its optical network topology to meet customer demand. Networks without signal regeneration are termed "all-optical" or "transparent" networks, and offer advantages such as bit-rate and modulation format transparency providing network operators a measure of future-proofing, and the flexibility to efficiently and rapidly deploy new services whilst maintaining legacy services [3].

There are two standards proposed for the management of these next generation networks, the Automatically Switched Optical Network (ASON) [4] and Generalised Multi-Protocol Label Switching (GMPLS) [5] standards. The standards both specify an automated control plane that oversees efficient, automatic, on-demand allocation of network resources, commonly referred to as "path selection". These path selection processes are traditionally carried out manually and are subject to human error, long provisioning time, inefficient resource utilisation and interoperability issues between different network operators [6].

Path selection in currently deployed networks use the Open Shortest Path First (OSPF) protocol that implements Dijkstra's algorithm [7], which computes the "minimal cost" path between two nodes, with respect to a "cost metric" assigned to network links. Typical cost metrics used in current networks include: hop count, link spare capacity, link propagation delay and economic cost. In most cases, the metric is either un-related or only weakly related to the signal degradation incurred by the path selected by the algorithm.

In current optical networks that do not use ROADMs, the assumption is that an optical signal propagating through the network is regenerated after each link, eliminating the need to consider the effect of the signal degradation in path selection algorithms. This is not the case in all-optical networks, where the absence of signal regeneration means that signal degradation accumulates over multiple links.

An example of this is shown in Figure 1.1. Here, an optical signal propagates from the node TX, through node N, to node RX and is attenuated by an amount A_1 (dB) over the first link, and A_2 (dB) over the second link. Let T (dB) be the maximum attenuation that can be tolerated for error free transmission, and let $A_1 < T$, $A_2 < T$, but $A_1 + A_2 > T$. If node N incorporates signal regeneration (meaning that node N provides signal gain $G = A_1^{-1}$) then the attenuation of the signal at RX is simply A_2 and the signal from node TX is received without error. Suppose that the signal regeneration capability is removed from node N. In this case, the signal leaving N has an attenuation of A_1, and arrives at node RX with attenuation $A_1 + A_2$, resulting in error-prone transmission.

It is well understood [8]-[10] that any reasonable path selection algorithm in an all-

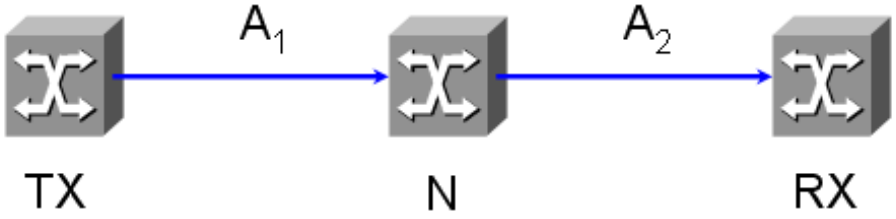

Figure 1.1: An all-optical network.

optical network must simultaneously account for different types of optical transmission impairments that accumulate across multiple optical links, such as amplified spontaneous emission (ASE), fibre residual chromatic dispersion (RCD) and polarisation mode dispersion (PMD).

1.2 THESIS OUTLINE

The objective of this thesis is to develop metrics and algorithms to enable automated path selection in intelligent all-optical networks. A new method for combining multiple physical layer impairments using the Eye Closure Penalty (ECP) in optical links is developed for use as a routing metric. The method is then extended to include the effect of time-variation of physical layer impairments, and applied in network simulations including the effect of user traffic requirements.

The thesis opens in Chapter 2 with an introduction to all-optical networking and a review of the issues associated with routing in all-optical networks. Current techniques and algorithms enabling impairment based routing, and their merits, are discussed. It is shown that routing using multiple cost metrics is a computationally intractable problem, justifying the "single metric" approach.

In Chapter 3, a simple method is presented to capture the effects of multiple optical impairments into a single signal degradation metric, the "eye closure penalty" (ECP). The accuracy of the method is demonstrated via simulation results for 10 Gbit/sec NRZ modulated signal. A relationship is derived algebraically linking the ECP to a signal quality metric, the "Q-Factor", which in turn is related to the optical link "bit error rate" (BER), a quantitative measure of the operational condition of the link. The accuracy of the relationship is also demonstrated via simulation results. The method is refined and additional impairments such as intra-channel crosstalk, inter-channel crosstalk, four-wave mixing and self/cross phase modulation are considered in the framework. The method is also applied successfully to DPSK modulation, 40 Gbit/sec and 100 Gbit/sec NRZ modulation.

Chapter 4 considers the case where the optical impairments are time-varying in nature. It is shown that it is possible to compute a probability that the BER of a link exceeds a certain threshold (due to multiple dynamic optical impairments), termed the "outage probability". A method is presented to compute the outage probability, given the probability distributions of the impairment values over time.

In Chapter 5, the thesis turns the focus to the simultaneous effect of user traffic and physical layer impairments on network availability. A metric, the "failure probability", is developed for a single link using analytic Markov Chain analysis that combines the effect of the outage probability and the "blocking probability" (the probability that a connection cannot be provisioned due to a lack of resources). The failure probability is applied, via simulation, to different networks and topologies, demonstrating the use of the failure probability in network dimensioning and dynamic routing.

Chapter 6 summarises the main findings and conclusions of the thesis, and discusses possible future work. This final chapter is followed by a list of supporting publications and a bibliography.

1.3 ORIGINAL CONTRIBUTIONS

The original contributions of thesis are as follows:

- A method to combine the effect of multiple optical impairments via the signal degradation metric, the eye-closure penalty (ECP) in a single optical link.
- Derivation of a relationship between the ECP and the signal quality metric, the Q-Factor.
- Demonstration of the method on 10 Gbit/sec NRZ modulated signals in the presence of ASE, PMD, RCD, intra-channel and inter-channel crosstalk, FWM and SPM/XPM.
- A method to account for the time-varying nature of optical impairments, culminating in the computation of an "outage probability" from temporal probability distributions of those impairments.
- An analytic method to combine the previously defined outage probability with the blocking probability due to user traffic demands in a single optical link.
- Development of a generalised simulation to compute the "failure probability" of optical paths comprising of multiple links in arbitrary all-optical network topologies.

2 All-Optical Networking

2.1 INTRODUCTION

This chapter provides the context for the work in this thesis by defining and summarising the merits of intelligent all-optical networks and highlighting the challenges associated with the planning and management of such networks. It reviews some of the main optical signal quality impairments that need to be considered in the deployment of all-optical networks and establishes much of the nomenclature used throughout the thesis. A survey of the current techniques and algorithms addressing these issues is presented and the chapter concludes by presenting rationale behind the approach presented in this thesis.

2.2 OPTICAL NETWORK EVOLUTION

The development of the first working laser in 1960 [11], followed by the first low loss (< 20 dB/km) optical fibres [12] and gallium-arsenide semiconductor lasers operating at room temperature [13] in 1970 sparked a concerted effort in the mid 1970s to develop optical fibre optics communication systems that continues through to the present day, in which 100 Gbit/sec per wavelength commercial field trials have recently taken place [14].

Early optical network transmission distances were severely limited by the attenuation and distortion of the propagating signal and required electronics placed at short intervals to re-amplify, reshape and retime ("3R") to the signal [15]. This requires that the signal be converted from an optical signal to an electrical signal, processed in the electrical domain, and converted back to an optical signal for transmission to the next receiver and is referred to as "optical-electrical-optical" or "O-E-O" regeneration. Key disadvantages of O-E-O regeneration are (i) the operating speeds

of electronic circuits limit the maximum bandwidth of the signal that can be processed and (ii) the recovery and processing of the signal is tied to the bit-rate and modulation format and is not transparent to network protocols.

During the 1990s, the bit rate in optical networks was practically limited to 10 Gbit/sec per wavelength by dispersive effects, non-linear effects and the speed of electronic components [16]. In the everlasting quest for higher capacity, "Wavelength Division Multiplexing" (WDM), a concept pursued and developed since the 1980s, allowed multiple optical signals, each modulated on a different optical frequency, to be simultaneously transmitted (multiplexed) over a single optical fibre [17]-[19], theoretically increasing the capacity of a fibre by up to two orders of magnitude. WDM networks were (and still are) seen as the most cost effective way of satisfying the exponential growth in demand for bandwidth resulting from the widespread penetration of the Internet into the consumer market. Key building blocks of modern WDM networks include fixed optical cross connects (OXCs), optical add-drop multiplexers (OADMs) and more recently, reconfigurable optical add-drop multiplexers (ROADMs). These components allow incoming optical signals on one wavelength to be switched between different fibres without the need for O-E-O regeneration.

Simultaneously, advances were made in the fabrication [20] and development of optical signal amplification technologies. These allow an optical signal, attenuated by fibre loss, to be amplified via stimulated emission to power levels adequate for optical to electronic conversion. Foremost amongst these are the erbium doped fibre amplifier (EDFA) [21], that enables signal amplification across a wide range of wavelengths (1530nm - 1565nm) corresponding to the minimal attenuation range in silica fibre. Alternatively, Raman amplification [22] utilises non-linear effects to provide gain across any wavelength range provided an appropriate pump laser is available. These amplification techniques can allow optical signals to be transmitted thousands of kilometres without O-E-O regeneration.

The increased transmission distances made possible using optical amplifiers also increase the amount of accumulated chromatic dispersion between O-E-O regeneration points. The management of this increased dispersion using dispersion

compensating fibre [3] and other techniques was an important part of designing WDM networks as dispersion affects the penalties arising from non-linear effects that are exacerbated by the use of multiple optical channels.

With the maturation of WDM technology and the wideband signal amplification capabilities of EDFAs, Raman amplification and dispersion management, O-E-O regeneration was perceived as less appealing, due to the cost and processing power consumption scaling with the number of wavelengths deployed in the optical network. Additionally, increases in wavelength transmission rates require more stringent timing constraints and increase physical power consumption in O-E-O regenerators [23].

Network providers were attracted to the concept of an "all-optical", or "transparent", network where no O-E-O regeneration is required between the optical transmitter and receiver, or at least all-optical sub-domains within the whole network, with O-E-O regeneration at a minimal number of key network locations. In recent times, ROADMs, more than any other technology, have enabled the deployment of all-optical networks [1], though advances in high speed electronics and cheaper integrated circuit fabrication have driven down prices of O-E-O regeneration hardware, keeping the technology competitive [24]. All-optical WDM networks allow a provider to offer a variety of different services, all using different protocols, bit-rates and modulations formats, over the same infrastructure. This is called "service transparency" [3]. Additionally, this allows a measure of "future-proofing", as the network is likely to be able to support new services without a complete network overhaul, allowing new services to be deployed with minimal disturbance to existing services.

Figure 2.1 shows an example of an all-optical sub-domain, within a larger core network, connected using ROADMs, with O-E-O regeneration at the ingress and egress nodes of the sub-domain (labelled "I" and "E"). Each ROADM or regenerator may be an aggregation point for smaller local and metropolitan area networks. Network traffic traversing the nodes between the ingress and egress nodes does so without signal regeneration. All-optical sub-domains may represent a part of a single operator's network, or the entire network, with the ingress and egress nodes

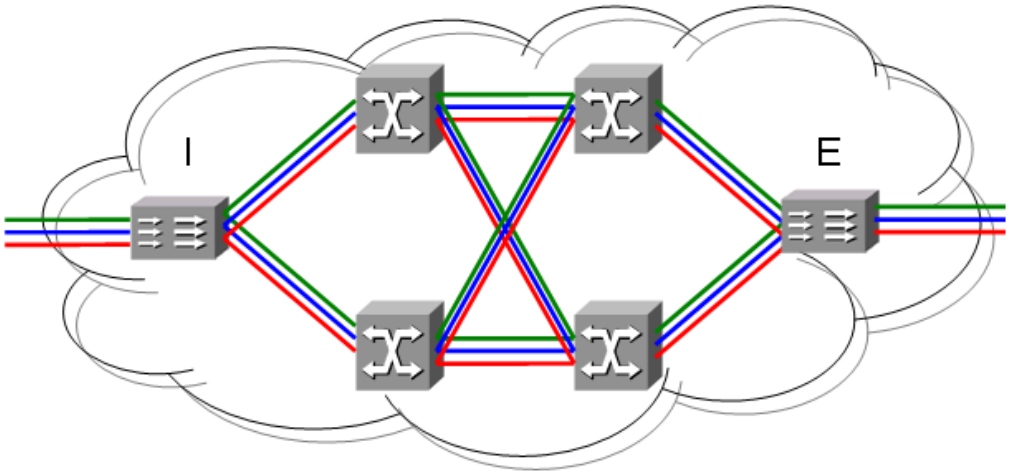

Figure 2.1: An all-optical sub-domain

representing an interface to another operator's network. The problems addressed by this thesis can be applied to either scenario without loss of generality.

2.3 Network Management and Control

In the 1960s, an increase in demand for mainstream voice communications forced network operators to consider a switch from analogue transmission to the more cost-efficient digital transmission that enabled the multiplexing of digitised voice calls over shared infrastructure, with the "Plesiochronous Digital Hierarchy" (PDH) standard emerging as a result. By the 1980s, it became evident that this was only an intermediate solution as demand continued to increase. The lack of clock synchronisation in nodes employing PDH was found to be an insurmountable technical hurdle when faced with the increasingly expensive task of extracting low bit-rate streams from increasingly large bit-rate streams this problem was referred to as the "multiplexing mountain" [25].

The solutions to this problem gave rise to the "Synchronous Digital Hierarchy" (SDH) and "Synchronous Optical NETwork" (SONET) standards in Europe and the USA. The two standards, both employ network synchronised clocks to conquer the multiplexing mountain and have only minor differences between them Apart from addressing the technical issues with PDH, SDH/SONET provided operators with an extremely comprehensive and effective set of network monitoring and management tools that enabled them to quickly locate faults and control network elements, albeit

in a “static” way. This capability has become absolutely essential for operators, so future network standards must provide similar robust monitoring and management tools.

It became evident that the emergence of next generation optical networks must be supported by next generation network monitoring and management tools. The Automatically Switched Optical Network (ASON) [26] and Generalized Multiprotocol Label Switching (GMPLS) [27] standards are frameworks developed by the International Telecommunication Union (ITU) and Internet Engineering Task Force (IETF) to enable fast resource provisioning, easier network operation, higher network reliability, scalability and simpler planning and design in next generation optical networks, by separation of the control and transport planes [28], as shown in Figure 2.2. The control plane interoperates with the transport and management planes through a set of standardised interfaces, dynamically configuring network elements to establish, maintain and tear down light paths through an optical network, and may or may not share the same infrastructure as the transport plane. Control planes between different sub-domains must be able to communicate via another set of standardised interfaces and are responsible for providing essential mechanisms such as discovery functions, routing, signalling and protection and restoration schemes.

The standards specify suites of protocols pertaining to signalling between network nodes for resource reservation (RSVP-TE and CR-LDP), for maintaining up-to-date network topology information (LMP), and path selection (OSPF-TE and ISIS-TE).

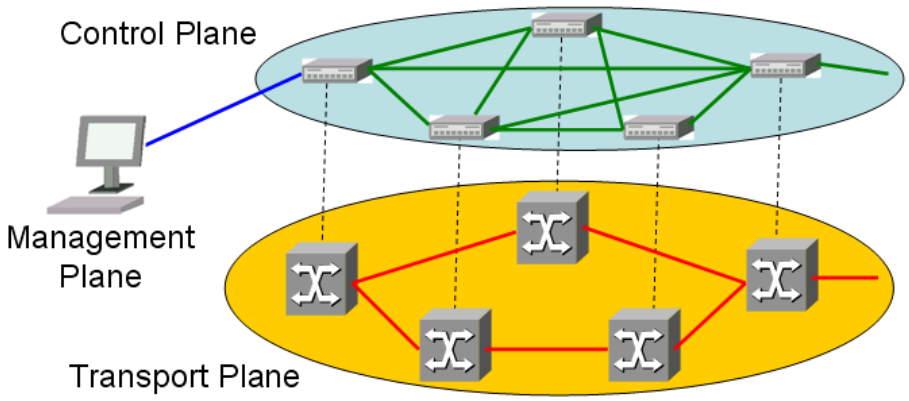

Figure 2.2: ASON Planes

Together with the management plane, these protocols and their extensions enable the use of information provided by optical performance monitors for intelligent network management.

The two frameworks have found common ground through input into the Optical Internetworking Forum (OIF) that promotes the development of interoperable network solutions through the creation of "Implementation Agreements" [29]. The purpose of bringing focus to these standards is to note that the next generation of optical networks is expected to be "intelligent" and able to provide a level of automation to the provisioning and management of resources that will in all likelihood include all-optical networks or sub-domains.

2.4 PATH SELECTION IN INTELLIGENT ALL-OPTICAL NETWORKS

As shown in section 2.2, all-optical networks are rapidly moving towards reality with the increasingly widespread deployment of ROADMs. However, the ASON and GMPLS standards have been developed from an IP perspective, and do not accurately reflect the physical limitations of the optical fibre transport medium, or the effect of concatenated, un-regenerated light paths in all-optical networks. Current path selection algorithms within ASON and GMPLS focus on network availability given the network load and/or service requirements. A selected path is considered to be either "on" or "off", with no indication as to the sustainability or reliability of that path due to physical layer degradations. Furthermore, ever-increasing link transmission rates (40Gbit/s and beyond) can dramatically reduced the resilience of optical signals to errors.

If the present protocols are not modified correctly to account for physical layer degradations, the network will have to be significantly over-designed to avoid the possibility of a selected path being unusable, resulting in unnecessarily increased capital and operational expenditure. The consideration of physical layer degradation will require information about these degradations being provided to the control plane for use by the path selection protocols, using technologies such as, for example, described in [30]. The network elements deployed in a network will typically come from a range of vendors and the total path in a network may cross through multiple

carrier networks, therefore some form of standardised protocol (likely within the ASON/GMPLS framework) will be required to provide these data to the control plane, but this is outside of the scope of this work.

The work in this thesis is focused on improving the routing functionality of next generation intelligent all-optical networks, the requirements for such are described by the ITU in [31] and studied by the IETF in [27], by developing better routing metrics that are closely related to physical layer impairments and, later on, user traffic requirements. The ASON framework has adopted the Open Shortest Path First (OSPF-TE) and Intermediate System to Intermediate System (ISIS-TE) [32] protocols with Traffic Engineering extensions as a basis for route automation. Both of these are "link state protocols" that use Dijkstra's algorithm [33] to compute the "shortest" route between two nodes in a network, relative to some routing metric. This provides the starting point for this work.

2.5 ROUTING ALGORITHMS

This section introduces some of the key algorithms used in network routing or path selection in modern day computer networks.

2.5.1 COMPUTATIONAL COMPLEXITY

The following discussion requires a brief explanation of the notion of "computational complexity", also called "time complexity". The "time complexity function" of an algorithm expresses, as a function of the problem input parameter size(s), the worst case time required to solve any instance of the problem that the algorithm is designed to solve. Of course, the absolute time required varies with the computational capabilities of the hardware that the algorithm is executed on and the particular implementation of the algorithm, so the time complexity function is expressed in terms of "required number of computations", rather than units of time. The time complexity of a problem is the time complexity of the most efficient algorithm able to solve any instance of the problem.

Consider the problem of determining if a particular playing card, the ace of spades, is contained in an unordered set of n unique playing cards. The simple algorithm to

solve this is to check through each card in the deck sequentially, and at worst, this requires checking through n cards (or n "computations") before finding the ace of spades. This algorithm thus has a time complexity function $f(n) = n$ which can be expressed in "big O" notation, that represents an asymptotic upper bound of the magnitude of $f(n)$, as $O(n)$. Formally, a function $f(n)$ is $O(g(n))$ if there exists a constant c such that $f(n) \leq c \cdot |g(n)|$ [34].

If a problem is determined to have a time complexity $O(p(n))$ where $p(n)$ is a polynomial function in the variable n, where n denotes the problem input size, then it is said to solvable in "polynomial time". Any problem that has complexity that cannot be bounded by a polynomial function is said to be solvable in "exponential time". The consequences of having a problem with exponential complexity is that as the problem input size becomes large, the number of computations required to solve it becomes unfeasibly large. As an example, if a problem has complexity $O(n)$, then as n increases from 1 to 100, the solution time increases by a factor of 100, but if the complexity is $O(2^n)$, the solution time increases by a factor of $2^{100} = 1.27 \times 10^{30}$. In the context of computation, a problem is said to be "intractable" if no polynomial time algorithm exists that can possibly solve the problem [34].

It is important to note that while a particular algorithm may theoretically have exponential time complexity, that "complexity" is a worst case measure. The algorithm may run much more quickly for most instances of the problem, and may still be useful and run more quickly than polynomial time algorithms when the input size is limited. However, these cases are rare, and often exponential time complexity algorithms are variations on an inefficient exhaustive search of all possible solutions.

2.5.2 DIJKSTRA'S ALGORITHM

Dijkstra's algorithm is an algorithm used in graph theory, and commonly applied to computer networks, to compute the shortest path from a source node to every other node (known as the "shortest path problem") for any weighted, directed graph with single, non-negative edge path costs. The result is called a "shortest path tree".

An example of such a graph is shown in Figure 2.3. The graph vertices represent network nodes, while the directed edges (bi-directional in this case) represent

network links. Let the cost (or "weight") of using a link between nodes A and B be denoted by c_{AB}. The computational complexity of the algorithm for a graph with V vertices and E edges can range from O(log(V)) to O(V^2) depending on the number of edges in the graph [35].

The algorithm can be summarised in four steps as follows:

1. *Permanently* label the source node: [-,0] and *temporarily* label every other node: (-,∞) as shown in Figure 2.3a. Each node label (p,d) is a 2-tuple, where d is the current cost of the candidate shortest path back to the source node, and p is the previous node in the shortest path.

2. Consider all temporarily labelled nodes which are directly connected to the *most recently* permanently labelled node n: [p_n,d_n]. This is initially the source node. For each such temporarily labelled node m: (p_m,d_m), if $d_n + c_{nm} < d_m$ then change p_m to n, and d_m to $d_n + c_{nm}$, otherwise do not change the labelling. This check is called the "relaxation" of the edge m-n.

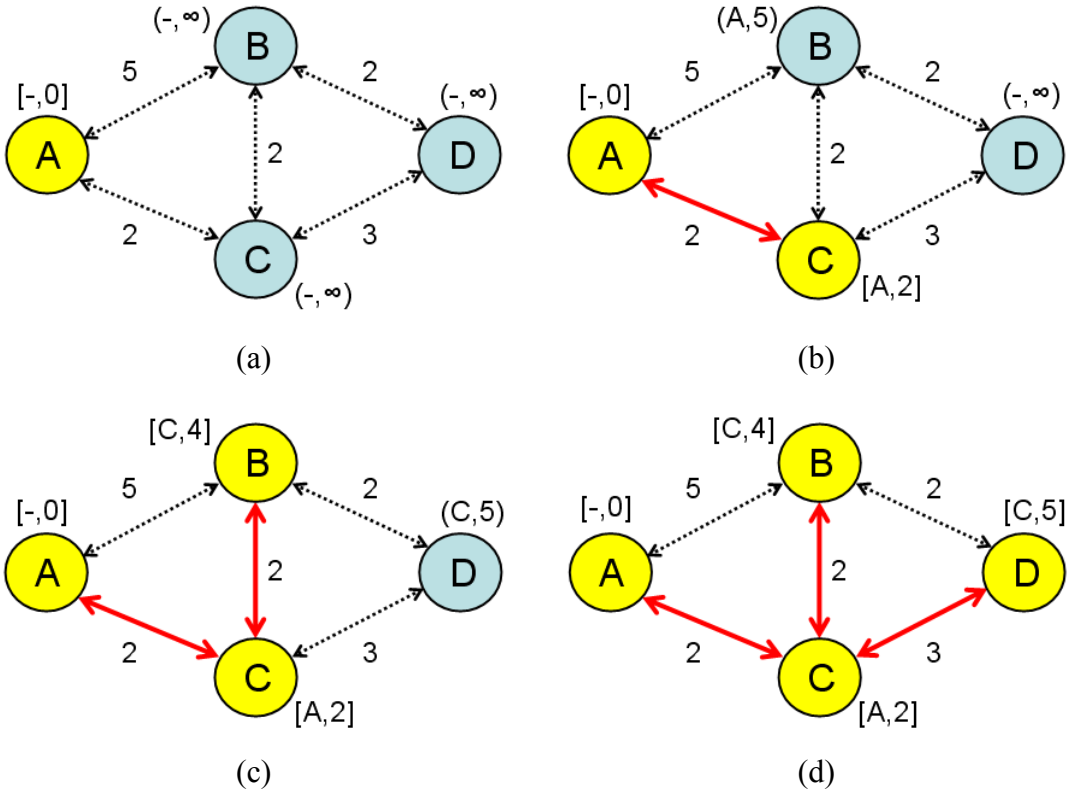

Figure 2.3: Dijkstra's Algorithm

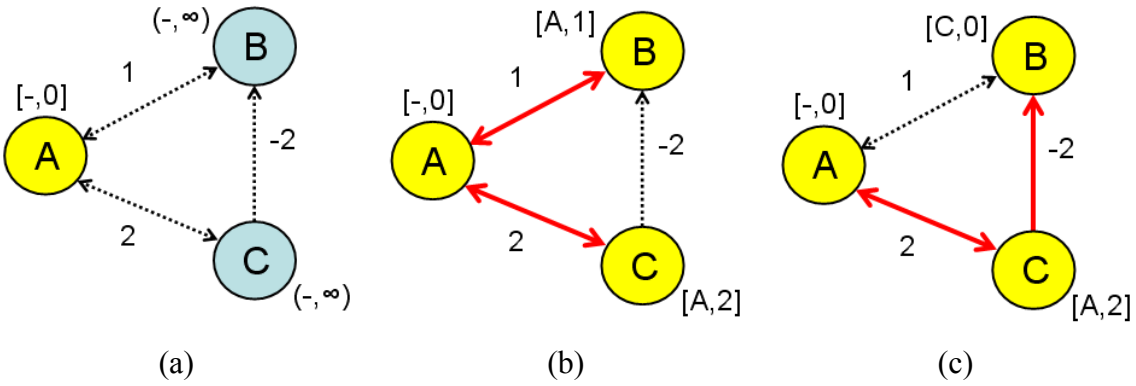

Figure 2.4: Incorrect Dijkstra

3. Examine all the temporarily labelled nodes, choose the one that has least cost from the source node and make it a permanent label, and thus the *most recently* permanently labelled node. In Figure 2.3b, this is node *C*.

4. If there remain temporarily labelled nodes, repeat the process from step 2. Stop otherwise.

Figure 2.3c and Figure 2.3d show the steps required to find the shortest paths from node *A* to the other nodes in the example four node network. At the conclusion of the algorithm, each node *n* has a permanent label that contains the minimal cost d_n from the source node, and the previous node p_n that must be traversed from the source node along the shortest path. The actual shortest path from node *A* to node *D*, for example, is found by recursively tracing the path backwards from *D* using values of the previous nodes p_n. In this case, p_D is *C*, and p_C is *A*, so the shortest path is *ACD* with a cost of 5.

2.5.3 BELLMAN-FORD ALGORITHM

Dijkstra's algorithm is guaranteed to compute the shortest path from the source node to the destination node when each of the edge weights is a non-negative value. However, in cases where negative valued edge weights are allowed, it may not converge to the correct solution.

Consider the network in Figure 2.4a with source node *A*, where the uni-directional link from *C* to *B* has a cost of -2. Figure 2.4b shows the shortest paths computed by Dijkstra's algorithm for this network, but Figure 2.4c shows the correct solution, where the path to node *B* is *ACB* with cost 0. The discrepancy arises because the label at node *B* is made permanent before the algorithm can account for the negative weight cost between nodes *C* and *B*. This problem can be solved by modifying the step 2 of the algorithm to check the relaxation condition for edges connected to *all* nodes connected to the most recently permanently labelled node, rather than just the *temporarily* labelled nodes. This generalisation of Dijkstra's algorithm results in the Bellman-Ford algorithm [36], [37], which has a computational complexity of O(*VE*) where *V* is the number of vertices and *E* is the number of edges in the graph.

Negative edge weights introduce an additional problem. Consider the graph in Figure 2.5, where both the uni-directional edge weights between nodes *B* and *C* are -1. In this case, it is not possible to find a shortest path from node *A*, as any candidate path can be arbitrarily "shortened" by cyclically traversing the negative weight edges between nodes *B* and *C* in what is termed a "negative weight cycle". In addition to computing the correct solution to the shortest path problem with negative edge weights, the Bellman-Ford algorithm detects if a network contains any negative weight *cycles*. If such a condition exists, there can be no solution to the shortest path problem.

2.5.4 OPTIMAL SUBSTRUCTURE PROPERTY

The Bellman-Ford and Dijkstra's algorithms, and in fact any optimal "shortest path"

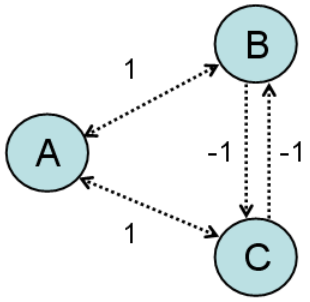

Figure 2.5: Negative Weight Cycle

algorithm, are computationally efficient "greedy" algorithms, meaning that they make the locally optimum choice at each stage with the hope of finding the global optimum. In general, greedy algorithms are not guaranteed to converge to globally optimal solution because they usually do not operate exhaustively on all the available data [35]. An example of this is Dijkstra's algorithm used on a graph with negative edge weights, already seen in the example associated with Figure 2.4.

In the specific case of the shortest paths problem for a graph with positive (and in the case of the Bellman-Ford algorithm, negative) edge weights that concatenate via linear addition (the weight of a path is the sum of all the weights of the edges on that path), both algorithms are guaranteed to converge to a globally optimal solution. This is because the problem exhibits the "optimal substructure property". Put simply, a problem is said to have "optimal substructure" if an optimal solution can be constructed efficiently from optimal solutions to its sub-problems.

Consider Figure 2.6 that demonstrates a graph routing problem satisfying the optimal substructure property. The wavy lines represent shortest paths between two nodes, the dotted lines represent individual edges and the edge weights add linearly. To find the shortest path between nodes A and Z (the global problem), the shortest paths between nodes A and X, and nodes A and Y (both sub-problems) can be found and the corresponding edge weights between nodes X and Z, and nodes Y and Z added to the results. This is possible because the path weights are computed as the sum of the weights of the edges in the path, so it is not possible for the path AXZ to be "shorter" than the path AYZ. An important corollary of the optimal substructure property is that, in this example, if the path AYZ is a shortest path between nodes A and Z, then the path AY must also be a shortest path between nodes A and Y.

2.5.5 MULTIPLE CONSTRAINT SHORTEST PATHS

To this point, the shortest path problem has been considered for graphs that have single edge weights. Modern computer networks, however, often have multiple parameters that are required to satisfy a range of constraints, e.g. choosing an adequate bandwidth path that also satisfies a delay constraint. This "multiple constraint shortest path" problem has been proven to belong to the intractable "NP-Complete" class of problems [34] and consequently this means that no algorithm currently exists that can guarantee an optimal solution to this problem much more efficiently than an exhaustive search of all possible solutions.

In the context of this thesis, the multiple constraint shortest paths problem is relevant because there are numerous physical layer impairments that degrade optical signal quality. For any given path, each of these impairments may independently, or in combination with other impairments, cause a connection along that path to become unsustainable if their accumulation along the path causes the connection bit error rate (BER) to exceed some threshold.

2.6 PHYSICAL IMPAIRMENTS IN OPTICAL NETWORKS

This section outlines some of the physical phenomena that act upon optical signals to degrade optical signal quality. It is not by any means an exhaustive examination of all possible optical impairments, but is intended as an example of the impairments that need to be considered in all-optical networking.

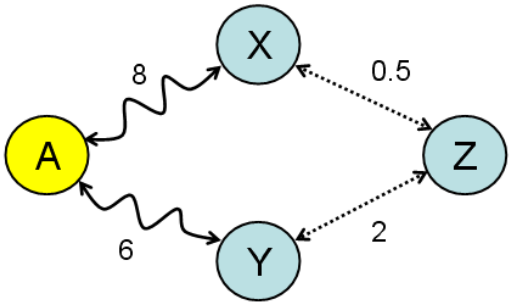

Figure 2.6: Optimal substructure property

2.6.1 LINEAR IMPAIRMENTS

Optical fibre communication systems that operate below a certain input power threshold will exhibit a linear relationship between the input and output signal powers, i.e. the loss and refractive index of the fibre are independent of the signal power. The key phenomena in this category are optical noise introduced by signal amplification used to overcome loss and optical pulse shape distortion giving rise to pulse broadening that may cause inter-symbol interference.

2.6.1.1 SIGNAL ATTENUATION (LOSS)

Signal attenuation refers to the loss of power of a signal propagating through optical fibre as distance increases. There are two main mechanisms that cause loss of signal power in optical fibre. The first is material absorption, where impurities within optical fibre absorb propagating signal power, often converting the energy into heat. This has been reduced to negligible levels in using better fibre production techniques, and signal attenuation is instead dominated by the second mechanism, "Rayleigh scattering" [38].

As an optical signal propagates through optical fibre, photons can interact with the atoms in the fibre causing energy to be scattered in all directions, in a process called "Rayleigh scattering". If a scattered photon does not propagate in the same direction as the original signal, then signal attenuation, or loss, occurs. The magnitude of attenuation is dependent on the material and the wavelength of the optical signal [39].

For a given material and wavelength, the relationship between the input and output signal powers, P_{in} and P_{out}, the length of material, L, and the loss coefficient, α, is:

$$P_{out} = P_{in} \exp(-\alpha L) \tag{2.1}$$

The coefficient α is often expressed in the units of dB/km, while in optical networking, L is often expressed in km.

Modern communications networks are engineered to transmit signals on wavelengths that coincide with the bands of wavelengths that have the locally minimal signal attenuation in optical fibre. At signal wavelengths of 1550 nm, 1300 nm and 800 nm

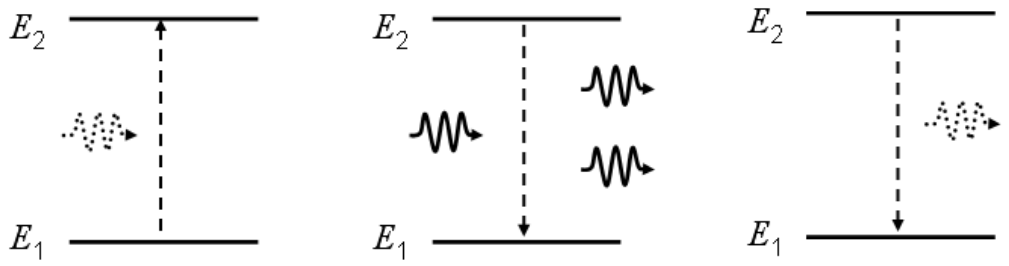

(a) (b) (c)

the signal attenuation coefficients are approximately 0.25, 0.4 and 2.5 dB/km respectively.

2.6.1.2 AMPLIFIED SPONTANEOUS EMISSION (ASE)

Doped fibre optical amplifiers, particularly the "erbium doped fibre amplifier" (EDFA), enable efficient transmission of optical signals over long distances to overcome loss, with significant cost savings. However, optical amplifiers can introduce significant amounts of noise into the amplified optical signals, commonly referred to as "amplified spontaneous emission" (ASE) noise. To comprehend the origin of ASE noise, a basic understanding of the quantum mechanical operation of optical amplifiers is required.

Consider Figure 2.7 that shows some permissible electron energy levels (E_1, E_2) in erbium-doped silica fibre. An electron may be excited from E_1 to E_2 if it gains enough energy to do so via interaction with an input light field that is used to "pump" the electrons from E_1 into the excited state E_2. For example, to excite an electron from energy level E_1 to E_2 would require a photon with energy $h \cdot f = (E_2 - E_1)$ to interact with the electron, where h is Planck's constant and f is the photon frequency. Transferring energy from the photon to the electron is a process known as photon "absorption" [40], and is shown in Figure 2.7a.

Figure 2.7: Absorption, Stimulated Emission and Spontaneous Emission

If an electron is in an excited state, E_2, it may decay to a lower state, E_1, by emitting a photon with energy $h{\cdot}f = (E_2 - E_1)$, which can occur in two ways. An incoming photon with energy $h{\cdot}f = (E_2 - E_1)$ may interact with the excited electron and stimulate it to emit a duplicate photon. This photon will have exactly the same characteristics (e.g. phase, direction) as the incoming photon. This process known as "stimulated emission" and is shown in Figure 2.7b. Alternatively, the excited electron may spontaneously decay and emit a photon with energy $h{\cdot}f = (E_2 - E_1)$ but with random characteristics. This process is called "spontaneous emission", shown in Figure 2.7c.

Erbium (Er^{3+}) ions placed into the structure matrix of silica fibre allow electrons in the Erbium to occupy a band of energy levels that corresponds to energy level gaps (e.g. $E_2 - E_1$ in Figure 2.7) enabling stimulated emission of photons with wavelengths ($\lambda = c/f$, where c is the speed of light) in the range of 1525nm – 1565nm. This is fortuitous, as silica fibre has minimal attenuation for optical signals in this wavelength range, and as a result, most long distance optical networks operate in this band of wavelengths.

Consider a length of erbium doped fibre depicted in Figure 2.8, with an incoming (solid) signal photon of wavelength 1550nm entering from the left of the fibre. Assuming the length of fibre is "optically pumped" with enough energy so that most electrons within the Er^{3+} are in an excited state, the initial photon will cause stimulated emission of duplicate photons, which in turn may cause further stimulated emission of more duplicate photons, thus amplifying the original signal. This is the

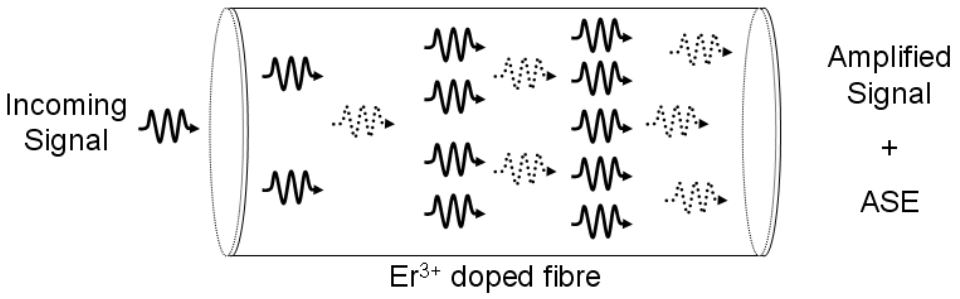

Figure 2.8: Amplification in erbium doped fibre

principle behind doped fibre optical amplifiers.

There is, however, a drawback to using the doped fibre optical amplifier. Recall that while an excited electron can emit a photon via stimulated emission, that it may also emit a photon via spontaneous emission (shown as dotted photons in Figure 2.8). Spontaneously emitted photons have random characteristics and manifest in the amplified signal as noise. Furthermore, as they propagate down the amplifier, spontaneously emitted photons are then subject to stimulated emission further into the amplifier. This is called "amplified spontaneous emission", commonly referred to as ASE noise. ASE noise within the signal bandwidth cannot be removed and is subject to gain from any other amplifiers downstream in the optical link.

The amount of ASE noise in an optical signal, P_{ase}, can be measured in linear units of power (Watts), or logarithmic units relative to 1 mW (dBm). Figure 2.9 shows an example of a power spectrum in an optical fibre after a signal of wavelength 1550 nm and output power 0 dBm has been amplified by an EDFA and a broad spectrum of ASE power introduced. As the propagating signal and ASE power passes through more EDFAs, each EDFA adds yet more ASE. Consequently the ASE noise level increases until such a time that the signal is unrecoverable.

The effect of ASE on signal quality depends on the relative powers of the signal and the ASE. The optical signal-to-noise ratio (OSNR), computed as the ratio of signal

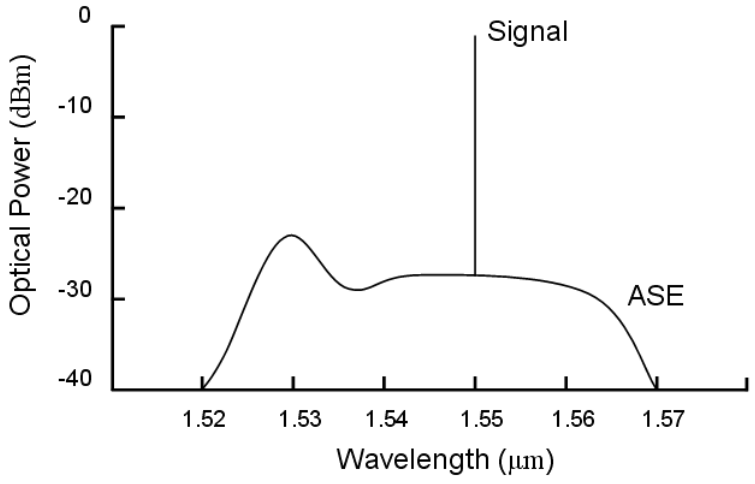

Figure 2.9: ASE spectrum

power (P_{sig}) to ASE power in dB per 0.1 nm of optical bandwidth, is a useful measure of the effect of ASE noise [41]:

$$OSNR = 10\log_{10}\left[\frac{P_{sig}(Watts)}{P_{ase}(Watts)}\right] = P_{sig}(dBm) - P_{ase}(dBm) \qquad (2.2)$$

The OSNR is correlated to the bit error rate (BER) experienced by an optical signal, and so if it drops below a threshold, the BER may increase to unacceptable levels. However, a high OSNR does not guarantee a low BER. The relationship between OSNR and BER will be covered in later sections.

As the effects ASE cannot be removed from a signal, network designers must ensure that the OSNR at the destination node must exceed a threshold corresponding to an acceptable BER. Intelligent placement of EDFAs within the network can also reduce overall end to end ASE levels.

2.6.1.3 RESIDUAL CHROMATIC DISPERSION (RCD)

Optical sources emit light not only at a nominal wavelength, but also a range of wavelengths around it, and modulated light that carries information intrinsically has a non-zero spectral width. This means the energy of the light beam is spread of a range of wavelengths $\Delta\lambda$ and any pulse of light representing information has a finite spectral emission width, α_λ, as shown in Figure 2.10a, usually characterised by the root-mean-squared (RMS) value. Figure 2.10b shows the total signal power of a single light pulse in the time domain.

Chromatic dispersion is a consequence of different wavelengths of light travelling at different phase velocities through optical fibre, because the refractive index $n(\lambda)$ of fibre is wavelength dependent [43]. Since an optical pulse contains energy over a range of wavelengths, the pulse "spreads" out in the time domain, as slower photons arrive at the receiver at later times relative to faster ones. This is best illustrated in Figure 2.11. In Figure 2.11a, two distinct pulses (possibly representing "1" bits) are sent one after another into an optical fibre. As the pulses propagate through the fibre, they spread and begin to overlap as shown in Figure 2.11b. In Figure 2.11c the two pulses can still be identified, but by Figure 2.11d, the two pulses have become

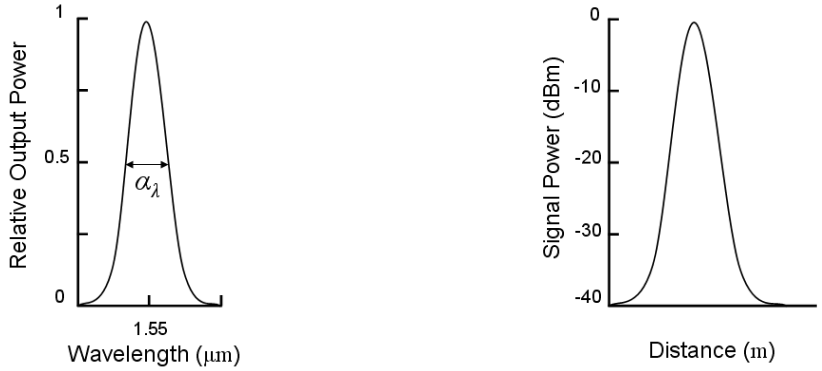

(a) (b)

Figure 2.10: (a) Optical pulse power spectrum
(b) Optical pulse time domain snapshot

indistinguishable to the optical receiver, and can cause errors in the received data stream. This phenomenon is called "inter-symbol interference" and, using standard modulation techniques, limits the maximum bit rate at which an optical transmission system may operate error free.

Assuming the RMS spectral width is not large and is symmetrical about the central wavelength λ, the amount of pulse spread, $\Delta\tau$, as a function of fibre dispersion, D, the spectral width of the signal $\Delta\lambda$ and length of the fibre L is [42]:

$$\Delta\tau = D \cdot \Delta\lambda \cdot L \tag{2.3}$$

and

$$D = -\frac{\lambda}{c}\left(\frac{d^2 n}{d\lambda^2}\right) \tag{2.4}$$

where λ is the nominal wavelength, c is the speed of light and n is the refractive index of the material (which varies with wavelength). The chromatic dispersion is measured in units of ps/(nm·km).

Unlike ASE, the effects of chromatic dispersion can be reversed. Because $d^2n / d\lambda^2$ can be positive or negative, the dispersion D can also be positive or negative dependent on the type of fibre the optical pulse travels through. As an example, if a span of optical fibre introduces a total RCD of D ps/nm into an optical pulse, the pulse can be transmitted through a span of "dispersion compensating fibre" (DCF) to

introduce a total RCD of -*D* ps/nm cancelling the original pulse spreading. Practically, though, this is a sub-optimal solution because while the net residual chromatic dispersion has been reduced, the pulse would have experienced additional attenuation through the dispersion compensating fibre. This requires optical amplification (and consequently injection of ASE) to recover the original pulse power. Nonetheless, this is a common method of dealing with dispersion in modern day optical networks.

Finally, it is of interest to note that any effect that modifies the refractive index of the optical fibre will thus also modify the chromatic dispersion of the material. These effects could include changes in temperature of the fibre, as well as non-linear effects caused by signals with sufficiently high output power.

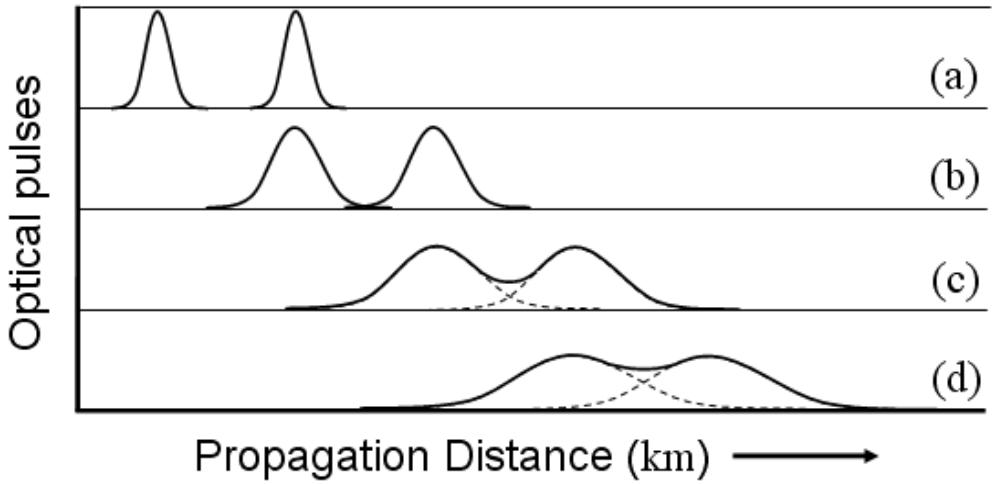

Figure 2.11: Inter-symbol interference due to chromatic dispersion

2.6.1.4 POLARIZATION MODE DISPERSION (PMD)

When light propagates, the orientation of its electric field is called its "state of polarisation". Figure 2.12 depicts a pulse of light propagating in the direction of the *z* axis, with a polarisation state of approximately 45° to the *y*-axis. In this case the components of the electric field in the *y* and *x* axes are shown in yellow and blue respectively.

In an ideal span of optical fibre, the cross section of the fibre core is perfectly circularly isotropic and light pulses propagating down the fibre experience an isotropic medium where there is no preferred axis of propagation. Real fibres, however, are often non-circular, and have bends and imperfections that cause the refractive index of the material to vary slightly along different axes. This results in a preferred "fast" polarisation axis along which light propagates more rapidly than other axes.

Consider Figure 2.13, where an optical pulse, with random polarisation state enters a real fibre propagating along its z-axis. Note that the optical pulse has electrical components in the y-axis and the x-axis. At the start of the fibre, the a_1-axis represents the direction of the "fast" axis and is aligned with the y-axis of the propagating pulse. The component of the optical pulse in the a_1-axis travels faster through the fibre than the component in the orthogonal a_2-axis, resulting in an overall time delay called the "differential group delay" $\Delta\tau$, between the fast and orthogonal axes, at the optical receiver.

This phenomenon is called "Polarisation Mode Dispersion" (PMD) and can cause inter-symbol interference in a similar manner to chromatic dispersion. Furthermore, the preferred "fast" a_1 axis of the fibre varies randomly with time, due to movement and temperature variations, throughout the fibre so the instantaneous value of $\Delta\tau$ for a fibre span must be characterised statistically, and has been shown to fit a Maxwellian distribution [44]. Unlike chromatic dispersion, it is very difficult to compensate for PMD. Examples include the use of expensive fibres that only permit one mode of polarisation propagation, or complex controlled feedback systems with

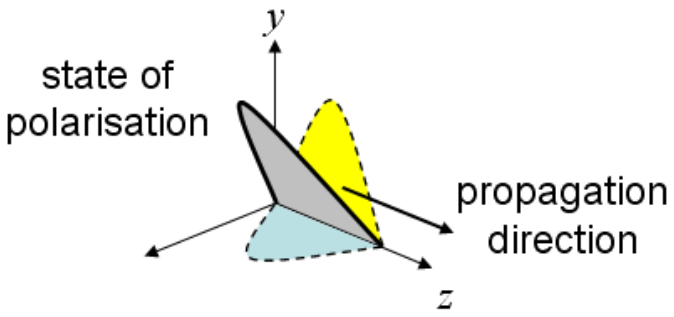

Figure 2.12: Polarisation of propagating light

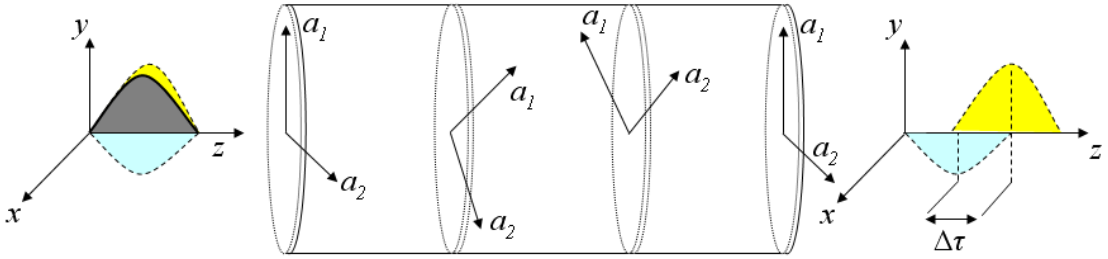

Figure 2.13: Polarisation mode dispersion

polarisation splitters to introduce a delay between the two polarisation axes [44].

PMD and chromatic dispersion have a greater impact in higher bit rate systems, in which the bit period of the optical signals is smaller.

2.6.2 NON-LINEAR IMPAIRMENTS

Light frequencies propagating in a vacuum do not interact with one another, however when light travels in a material, such as optical fibre, they may interact via the material causing undesirable effects. Non-linear impairments refer to phenomena that only occur when the signal energy propagating in a medium attains sufficiently high intensities. This can be due to high launch powers and/or the confinement of energy in extremely small areas, for example in optical fibre core. The overall effect of non-linear impairments is generally to induce phase variation and introduce noise in to the optical signal [45].

In short-haul systems up to around 100km in length, these effects can generally be ignored because required signal launch powers remain below the non-linear threshold (~1 mW). However, long-haul and all-optical systems require higher signal launch powers to overcome the accumulation of ASE [16], and while non-linear effects are small in isolation, they can accumulate to significant levels over large distances.

This section is intended to be a brief background and summary into these highly complex effects. Comprehensive derivations and explanations can be found in [16] and [46].

2.6.2.1 STIMULATED BRILLOUIN SCATTERING (SBS)

Stimulated Brillouin Scattering (SBS) is a result of high power (>3 mW) optical signals, causing mechanical (acoustic) vibrations in the optical fibre that travel along the length of the fibre. These vibrations cause small forward-propagating variations in the refractive index of the fibre, which act like moving mirrors that weakly reflect, or scatter, forward propagating signal light. Back-propagating light is Doppler shifted to lower frequencies (by about 10-11 GHz) that can drain energy from the signal, ultimately resulting in increased noise in and attenuation of the optical signal.

System impairment starts when the amplitude of the reflected wave is comparable to the signal power, which in typical fibres is around 10 mW for single fibre spans. SBS is typically limited to single fibre spans, as there are usually optical isolators to prevent the back-propagating light from entering optical amplifiers [47]. SBS can be mitigated most effectively by rapid dithering of the carrier wavelength over a range of about 1 GHz [48].

2.6.2.2 STIMULATED RAMAN SCATTERING (SRS)

Stimulated Raman Scattering (SRS) is an interaction between light and the vibrational modes of the silica molecules in optical fibre. If a photon with frequency f_1 interacts with a molecule with vibrational frequency f_m, the molecule may absorb some energy from the photon and scatter the photon with a lower frequency f_2, called the "Stokes wave". In both SBS and SRS the presence of a second optical field that can accept energy from the signal field enhances the effect (hence the term "stimulated"). In SRS other WDM channels provide this field.

Typically, this process requires extremely high optical power, and so is not as prevalent in single wavelength systems, but in WDM systems, power from higher frequency channels may be transferred to neighbouring lower frequency channels. SRS can be mitigated by closer spacing between WDM channels, because the coupling between the channels due to SRS increases with channel spacing, peaking at approximately 12 THz in silica [42]. However, narrower channel spacing can intensify other undesirable effects, such as Four Wave Mixing. SRS can also be

deliberately used to provide optical amplification to optical signals in the process called "Raman amplification".

2.6.2.3 SELF AND CROSS PHASE MODULATION (SPM AND XPM)

The refractive index of optical fibre, n, is actually dependent on the optical signal intensity, I, given by [42]:

$$n = n_0 + n_2 I = n_0 + n_2 \frac{P}{A_{eff}} \tag{2.5}$$

where P is optical signal power, A_{eff} is the effective area of the fibre core cross section, n_0 is the linear refractive index of the optical fibre and n_2 is the "nonlinear index coefficient", which in silica varies between 2.2 to 3.4 × 10^{-8} $\mu m^2/W$. When I is large, the nonlinear component of the refractive index becomes significant, resulting in the "Kerr effect". Figure 2.14 shows the change in refractive index of optical fibre caused by a high intensity optical pulse.

The refractive index changes induced by the Kerr effect cause phase changes in different parts of the optical pulse to travel at different speeds, resulting in new frequencies being introduced into the pulse. This frequency ("chirp") broadens the frequency spectrum of the signal. The Kerr effect inducing phase changes of a signal due to its own intensity variation is known as "self phase modulation" (SPM). When the Kerr effect induces phase modulation in a signal due to intensity variations in other channels, this effect is known as "cross phase modulation" (XPM).

Although SPM can mitigate the effect of fibre dispersion, XPM always degrades signal quality in a WDM signal. Additionally, the effects of XPM on WDM channels

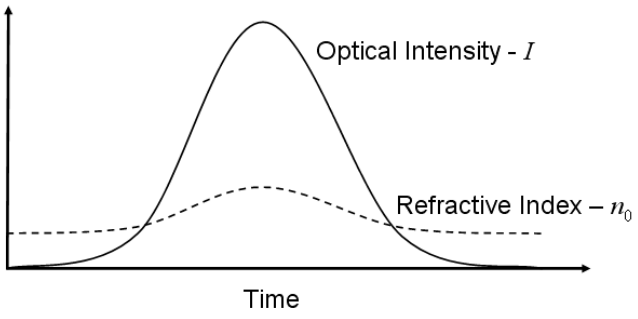

Figure 2.14: Kerr effect

may be somewhat mitigated by a larger channel spacing in the presence of non-zero fibre dispersion. This causes the pulses in different channels to travel at different speeds and therefore to pass through each other thereby mitigating the effect of XPM.

2.6.2.4 FOUR WAVE MIXING (FWM)

In WDM optical networks, multiple channels at different wavelengths (frequencies) propagate down a single fibre. The signals on these channels naturally interact to produce new signals. Figure 2.15a depicts FWM generated by two signals at frequencies f_1 and f_2 to produce new signals at frequencies $2f_1 - f_2$ and $2f_2 - f_1$. Figure 2.15b shows the new signals generated by FWM when there are 3 signal frequencies. In general, for N signal channels, the number of generated mixing products M will be [42]:

$$M = \frac{N^2}{2}(N-1) \tag{2.6}$$

and the generated FWM frequencies are given by:

$$f_{ijk} = f_i + f_j - f_k \quad , i \neq k, j \neq k \tag{2.7}$$

meaning that for $N = 8$, the number of generated channels would be 224! If the FWM signal frequencies fall within WDM channels, intra-channel crosstalk occurs, degrading the quality of those channels.

If signal channels are equally spaced, then the FWM signals will coincide with the WDM signal channels. This can be mitigated by spacing the channels unevenly.

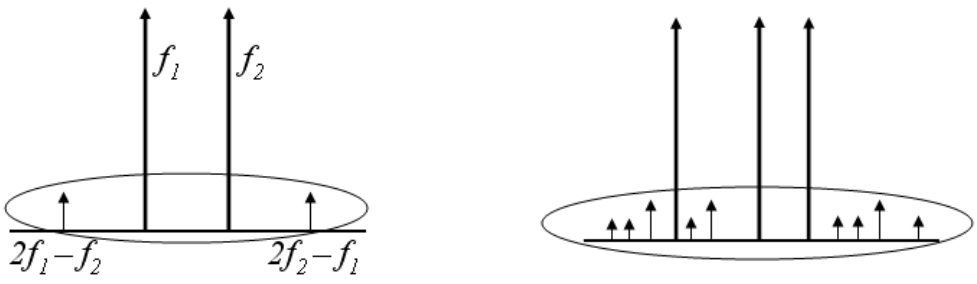

(a) (b)

Figure 2.15: Four Wave Mixing

Furthermore, FWM can be mitigated by increasing the spacing between signal channels. Chromatic dispersion naturally mitigates FWM, because FWM occurs when optical pulses stay in phase over significant distance, and similar to XPM, chromatic dispersion causes optical pulses to "walk away" from each other, thus reducing the instantaneous signal intensity at points in the fibre.

2.6.3 CROSSTALK

Crosstalk generally refers to the effect of other signals on a desired signal. It occurs in almost every component of a WDM network, such as filters, switches, (de)multiplexers and optical fibre through nonlinear effects such as FWM [3], [49].

Two types of crosstalk may occur in WDM networks; "inter-channel" and "intra-channel" crosstalk. Inter-channel crosstalk occurs when the direct beat product of the signal and crosstalk terms that leaks into a reference channel from another channel falls outside of the electrical bandwidth of the reference receiver, leaving only the square-law detection of the optical crosstalk power. Figure 2.16a shows this occurring in a de-multiplexer, where two channels have been imperfectly isolated from one another in the de-multiplexing process. The de-multiplexer filter allows some energy from the signal at λ_1 to enter the output fibre designated for λ_2, resulting in noise that lies outside of λ_1's electrical receiver.

Of more concern is intra-channel crosstalk, which can occur in network elements, such as OXCs. Figure 2.16b shows two independent signals, both modulated at wavelength λ_1, entering an optical switch on ports 1 and 2. In the switching process, if the isolation between the output ports is not ideal, then signal power leaks to the

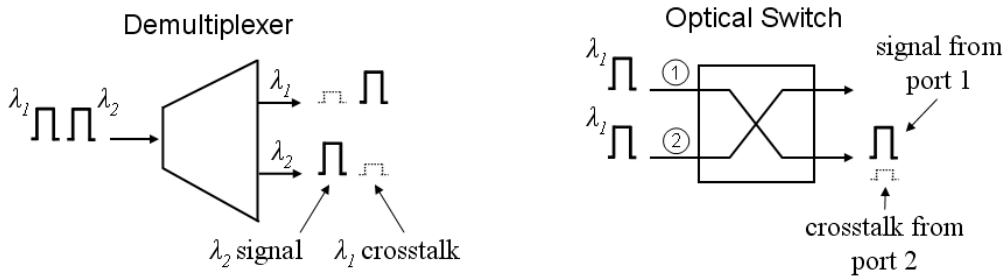

(a) (b)

Figure 2.16: Crosstalk in WDM networks

unintended output port and the result is crosstalk that falls in the same wavelength as the desired signal. This effect can be more severe than inter-channel crosstalk, as some of the beat products of the signal and crosstalk terms fall within the bandwidth of the electrical receiver cannot be filtered out [42].

The simplest way to reduce crosstalk is to improve crosstalk suppression in optical devices [46]. Techniques such as increased spatial and wavelength separation between channels within devices can be used. These require more switch fabric space and use of dummy wavelengths. Adding filters for each wavelength within multiplexers and de-multiplexers is effective, but also adds to the cost of equipment.

2.7 ALL-OPTICAL PATH SELECTION

Conventional path selection in all-optical WDM networks or sub-domains is based upon satisfying two conditions, but does not account for physical layer impairments. The first condition is to obtain a connected route over physical fibre links (called "routing"). The second is the "wavelength continuity constraint", meaning that for any chosen route, the same wavelength must be used on each link [50], [51] and no two connections passing through the same fibre are assigned to the same wavelength ("wavelength assignment"). The overall path selection problem is often referred to as "routing and wavelength assignment" (RWA) [52]. The wavelength continuity constraint can be relaxed with the use of "wavelength conversion" [53], but currently, this technology is expensive and not yet commercially mature [54].

Routing can be considered to be fixed (incoming connections are always assigned to one or more fixed routes) or adaptive (different routes are computed for each incoming connection based on the state of the network). Fixed routing is simpler in terms of analysis, computation and implementation, but adaptive routing results in lower connection blocking probabilities and often more efficient use of resources. Wavelength assignment similarly can be either static or adaptive, and can include varying degrees of wavelength conversion, with many schemes covered in [57].

The RWA problem can be naively formulated in terms of an integer linear program [50], for which the globally optimal solution is an NP-complete algorithm [55], and is therefore unsuitable for dynamic provisioning of connections in an optical

network. More commonly, the problem is simplified by decoupling the routing (R) and wavelength assignment (WA) algorithms to give approximate solutions, the most common of which are comprehensively covered and evaluated in [56] and [57].

In traditional RWA schemes, path selection is based on shortest path algorithms using simple "cost" metrics such as the "number of hops", or "available bandwidth" [7], [56], [57]. These algorithms do not account for the signal degradation that occurs from optical transmission through concatenated links, due to physical layer impairment effects discussed above. Without considering signal degradation, there is no guarantee that a provisioned path will provide and sustain a required signal quality [58], [59]. This problem is widely known and significant work has been done to address the issue. In the literature, the work related to the path selection problem with physical constraints is generally referred to as "impairment constraint-based routing" (ICBR) and "impairment-aware routing and wavelength assignment" (IRWA) [60], [61]. The optimal solution to such a multi-constraint routing problem is a computationally intractable NP-complete problem [34].

A comprehensive summary of the many types of heuristics and developments in IRWA is given in [62]. These include the decoupling of the routing and wavelength assignment problems, the use of meta-heurisitic algorithms such as ant colony optimisation or genetic algorithms, and joint IRWA algorithms involving transformations of the network topology to include wavelength availability.

The authors of [63] recognise that it is difficult to account for multiple physical and system constraints using conventional shortest path algorithms, and instead propose a distributed method of path selection between a source and destination node. The algorithm accomplishes this by sending messages containing path state information from the source node to all its neighbours ("flooding"). When received at intermediate nodes, these messages are updated with the accumulated path state data. Should any of the path constraints be violated (e.g. OSNR, cost, wavelength continuity), the messages are discarded, otherwise they are on-flooded to neighbouring nodes. The messages that eventually reach the destination node are then guaranteed to form a set of feasible paths, and the best of these paths can then be provisioned by the network. The scheme does not combine the effects of multiple

impairments and the authors admit that excessive numbers of messages, of the order of $O(n!m^n\log(n))$ where n is the number of nodes and m the number of wavelengths per link in a worst case mesh network, may be flooded through the network with each connection request. Methods to mitigate this in certain cases are presented. Another distributed approach based on "Ant Colony Optimization" (ACO) is presented in [64], using autonomous computational agents ("ants") that move semi-randomly throughout the network, preferring links with better performance, and populate the routing tables of the OXCs. When an ant reaches its destination node, it travels backward, reinforcing the path that it chose as a "good" path. The more ants that end up choosing a path makes the path more desirable for connections to the destination node. Both of these algorithms originate from a computer networking background, and are not focused on the specific effects of physical layer impairments.

More conventionally, the majority of the prior work into IRWA comes from an optical networking background, with recent contributors [59]-[60], [65]-[78] extending conventional RWA techniques to include physical layer considerations. Figure 2.17 gives an overview of the generic IRWA process. Here, conventional RWA algorithms are used to determine the best candidate path (route and wavelength assignment) for an incoming connection, which is then sent to a signal quality evaluation module. If the candidate path meets the signal quality

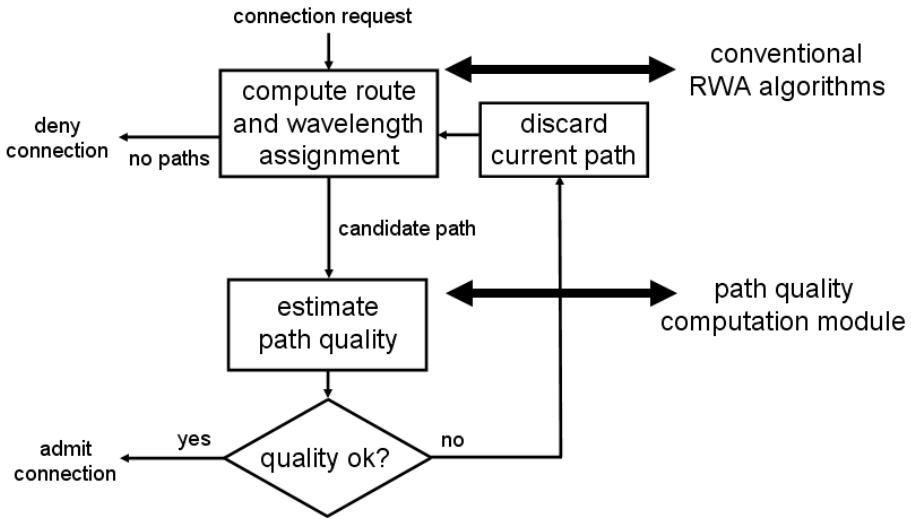

Figure 2.17: IRWA algorithm structures

requirements, then the connection is admitted, otherwise the path is discarded, and the process repeated using the next candidate path. This process continues until a path is found that meets the signal quality requirements and the connection admitted, or there are no paths left to consider and the connection denied. The focus of most prior work has been developing algorithms and signal quality metrics for use in the path quality computation module.

The simple example path quality computation module in [60] separately considers two optical impairments – PMD and ASE (in the form of OSNR). In this case, the total PMD and OSNR are computed independently for the candidate path, and if either exceeds pre-determined thresholds, the path is discarded. This method does not account for the effects of chromatic dispersion, and algorithmically does not consider the combined effect of multiple impairments. The work in [59] combines the effect of ASE and crosstalk on a candidate path received BER, which is then used as the path quality estimate but does not consider PMD or chromatic dispersion. The framework established in [60] is explored in more detail by the same authors in [65] including the effects of distributed Raman amplification. In [66] the authors propose the desirability of being able to capture the impacts of some impairments as a link state parameter for each network link, to enable the use of conventional routing algorithms. Similar works in [67] and [68] incorporate ASE and XPM/FWM as noise variances into either the OSNR or Q-factor for use in the path quality computation module, but ignore the effects of chromatic dispersion and PMD by assuming network engineering solutions to minimise their effects.

Publications [69]-[72] share many principle authors and the early work [69] considered a range of impairments including ASE, PMD, chromatic dispersion, crosstalk and filter concatenation. Each of these effects was considered in isolation, or it was assumed that only one of the impairments was dominant. The work in [70] focussed on studying the effect of chromatic dispersion and filter concatenation. Further evolution of this is presented in [71] where the noise effects such as ASE and crosstalk are combined into a “noise penalty” factor. The effects of PMD, chromatic dispersion and filter concatenation combined into an “eye penalty” factor. These factors were multiplied with the “Q-factor” signal quality metric (which is related to

BER) for use in the path quality computation module described above. In this way, the effect multiple impairments were considered simultaneously. The work presented in [72] introduced a simple model that approximately accounts for the FWM and XPM non-linear effects by adding their noise variance contribution to the ASE and crosstalk variances in computing the Q-factor.

The authors of [73] and [74] also take a "Q-factor" approach in their formulation of the path quality estimation metric, incorporating the effects of ASE, FWM and XPM as "noise variances" in a similar manner to the authors of [71] and [72], but without the consideration of distortion effects (PMD and chromatic dispersion). Of particular note is the inclusion of an extra step in the path quality computation module that accounts for the effect that an incoming candidate path has on the Q-factor of existing connections.

The authors of [75]-[76] focus on the effects of noise generated by, and the effect of gain saturation in optical amplifiers as the dominant factors for in a path signal quality metric. A key difference between these works to those presented above is that the RWA selection phase is also conducted using the signal quality metric, rather than the physical distance. This is possible because the noise figure monotonically increases through multiple links and is expected to satisfy the optimal substructure property, though this is not explicitly shown. These early works do not consider waveform distortion effects, but a derivative work [77] accounts for four wave mixing as an additional noise effect, and considers PMD separately as an additional constraint. Another paper by the same core authors [78] uses a simplified weighting metric for the RWA phase consisting of rudimentary quantities such as link length, link availability, link usage and number of hops. The weighting function consists of two tuneable parameters that are determined through offline simulation for use in online path selection. Once a candidate path is selected, the path quality computation metric evaluates the OSNR of the path using techniques similar to those in the authors' earlier works.

The work in [79] presents a FWM aware RWA algorithm that assumes that FWM is the single dominant impairment in WDM networks. A signal quality metric that is based on computing the FWM power for each link and adding them together is used

to account for the physical layer degradation. The work in [80] assumes that the ASE is the dominant impairment and that it is possible to estimate the Q-factor by subtracting penalties from an initial Q-factor, which may not always be the case.

2.8 IMPROVED ROUTING METRICS FOR ROUTING IN ALL-OPTICAL NETWORKS

The objective of this thesis is to develop improved signal quality estimation methods for use in impairment based routing and wavelength assignment of connection requests in all-optical networks. These methods are based upon the combination of multiple physical layer impairments such as PMD, RCD and ASE into a single signal quality metric that can be used in the path quality computation module within the commonly used framework presented in [60]. Several papers have been published on the work presented in later chapters [81]-[85]. In chapter 3, a rigorous framework for combining multiple optical impairments is presented and tested for accuracy.

2.9 CONCLUSIONS

A detailed overview of the optical networking landscape has been presented, with a progression from legacy optical networks through to next generation intelligent all-optical networks. These networks are expected to provide automated dynamic connection provisioning, which is reliant on effective routing and wavelength assignment in the presence of multiple physical layer impairments.

Conventional shortest path routing algorithms and the problems associated with applying these to multiple constraints were presented, followed by a summary of important linear and non-linear optical signal degradation effects that need to be considered in the IRWA problem. Finally, a survey of the relevant work in the literature was conducted, revealing that the problem is typically tackled by decoupling the routing and wavelength assignment process from the path quality validation process using variants of a two step algorithm presented in [60]. The path quality validation process involves evaluating the signal quality of a candidate path selected by the routing and wavelength assignment process.

Developing improved methods for evaluating signal quality to enable routing in intelligent all-optical networks is the subject of this thesis.

3 Signal Quality Estimation

3.1 INTRODUCTION

This chapter shows that the "Eye Closure Penalty" (ECP) metric can be used to unify the effect of multiple optical impairments. It begins by defining the ECP and its relationship to various linear optical impairments. By assuming independence between impairments, an estimate of the ECP from multiple impairments is proposed and tested via simulation, showing agreement adequate for the purposes of route determination. A relationship between the ECP and the signal quality metric, the Q-factor, is derived, providing a relationship between multiple optical impairments and the bit error rate (BER). A simple and accurate framework unifying multiple impairments into a single quality metric is then proposed and validated.

3.2 OPTICAL COMMUNICATION SYSTEMS

In telecommunications, a "communication system" is a collection of equipment that enables the exchange of information between two or more end points. In its simplest form, a telecommunications link consists of an information transmitter, receiver and a connecting medium that is influenced by noise and other impairments, as shown in Figure 3.1. In optical communication systems, the medium is light, transmitted

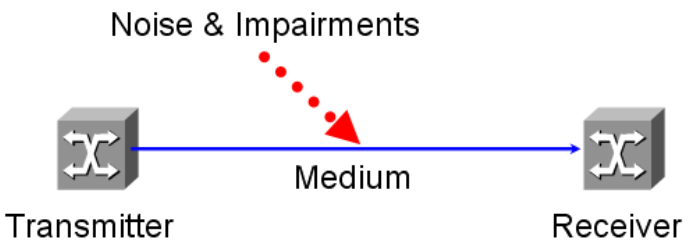

Figure 3.1: Communication system architecture

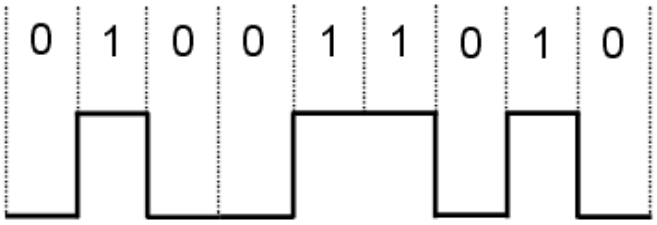

Figure 3.2: NRZ coding scheme

through silica fibres that guide it over long distances. In the context of this work, which is focused on all-optical networking as described in section 2.2, the distance between the transmitter and receiver may be several thousands of kilometres, resulting in accumulation of significant amounts of noise and impairments that could otherwise be ignored or easily mitigated with shorter links. Additionally, the adoption of WDM and ROADMs technologies may introduce crosstalk within intermediate nodes.

Digital data in optical communications is commonly transmitted using the most simple of coding schemes, amplitude modulated "non return-to-zero" (NRZ) scheme [87]. In this scheme, a "mark", or "1" bit is coded as a "high" power level by the transmitting laser, and a "space", or "0" bit is coded as a "low" power level, as shown in Figure 3.2. The light pulse from the transmitter travels through the optical fibre where it experiences noise and distortion. At the receiver a photodiode converts the optical energy into an electrical current using a photodiode [88]. Electronic circuits are then used to sample the level of the electrical current, relative to a threshold, to determine whether a mark or space was received. Ideally, transition

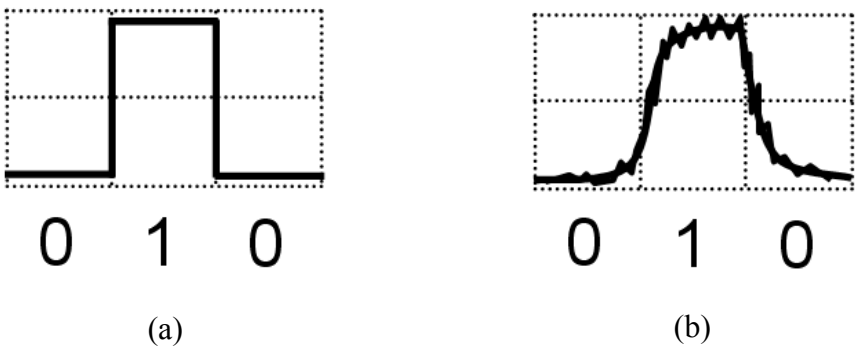

Figure 3.3: Ideal and real data waveforms

between the high and low power levels is effectively instantaneous so that the receiver can unambiguously correctly determine whether a mark or space was transmitted (Figure 3.3a). However, in reality, the switching between high and low levels requires time, and the power level of transmitted bits is altered by the presence of noise, distortion, and other imperfections in the optical path (Figure 3.3b).

3.3 EYE DIAGRAMS

A common technique used to assess the quality of transmission in optical networks is to overlay the received bit stream in the time domain over a three-bit sliding window, resulting in the superimposition of multiple instances of the eight three-bit binary sequences shown in Figure 3.4a. When this is done with real waveforms, the resulting diagram resembles an eye, and is hence called an "eye diagram", as shown in Figure 3.4b.

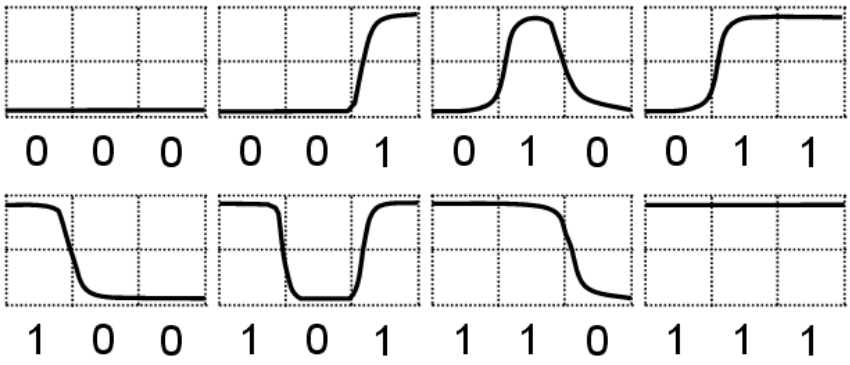

(a)

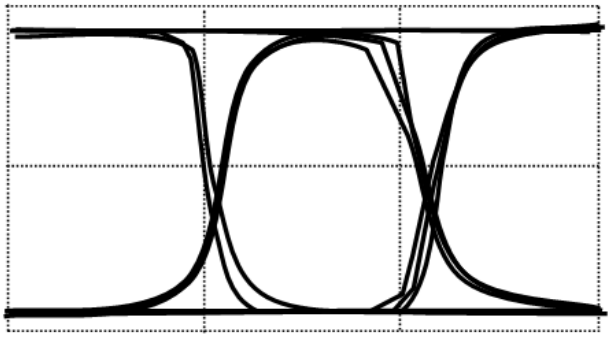

(b)

Figure 3.4: 3-bit sequences and resultant "Eye Diagram"

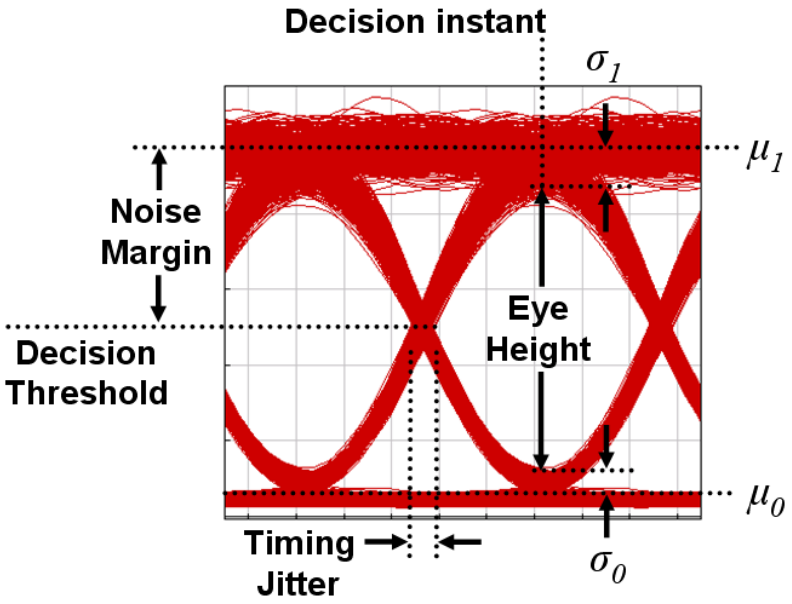

Figure 3.5: Annotated eye diagram in the presence of signal degradation

A great deal of system performance information can be ascertained from an eye diagram, including [89] the optical "decision instant", signal amplitude distortion, timing jitter, noise margin and the presence of asymmetric nonlinear distortion effects. Sampling a large number of bits at the decision instant (often chosen as the instant that the height of the eye is at its widest) provides the statistics of the signal levels generated from the receiver photodiode for marks and spaces. Assuming that the sampled values for these levels are independent and identically distributed, by the central limit theorem, it is reasonable to assume that these current levels can be modelled by Gaussian random variables, with a mean and standard deviation for marks, μ_1 and σ_1, and spaces, μ_0 and σ_0 [90].

When a received signal is degraded by optical impairments, the eye diagram becomes partially closed and distorted. For ASE, this corresponds to an increase in the standard deviation of the mark and space levels, whilst for PMD and RCD, this corresponds to distortions in the slope of the bit transitions and an increase in the timing jitter [90]. It is possible for a waveform to be distorted to such an extent that the received level for a mark may fall below the decision threshold at the decision instant and be interpreted as a space, and vice versa, resulting in a "bit error".

3.4 BIT ERROR RATE

The "bit error rate" (BER), is the number of bits received in error as a ratio of the total number of transmitted bits. The BER is a common measure of the reliability of a connection [90]. It is possible to calculate the BER using the received statistics of the received mark and space current levels.

Consider Figure 3.6, which depicts probability density functions $p_1(i)$ and $p_0(i)$ of the signal level of the received marks with mean value μ_1, and of the received spaces with mean value μ_0. Assuming that the probability of transmitting a mark or space is equal, the probability of a bit error, P_{error}, can be calculated as the sum of the probability that the received signal level for a transmitted mark falls below a decision threshold I_{th} and that the received signal level for a transmitted space falls above a decision threshold I_{th}, which is given by:

$$P_{error} = \frac{1}{2}\left[\int_{-\infty}^{I_{th}} p_1(i_{dec})di_{dec} + \int_{I_{th}}^{\infty} p_0(i_{dec})di_{dec}\right] \tag{3.1}$$

where i_{dec} is the signal level at the decision instant. If we assume that the mark and

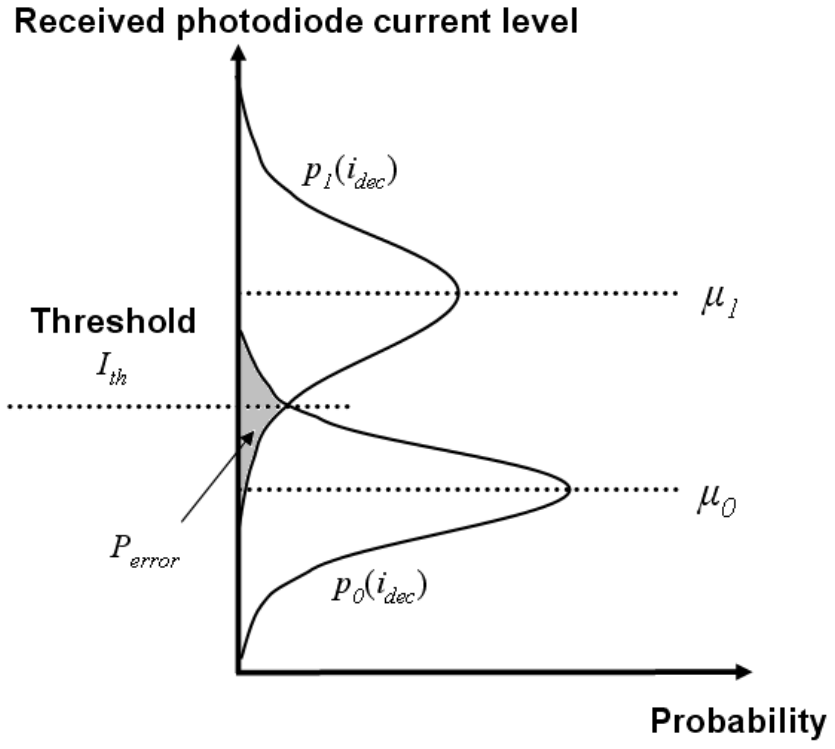

Figure 3.6: Computation of BER from received mark and space probability density functions

space levels at i_{dec} are modelled by Gaussian distributions with mean and standard deviations given by μ_1 and σ_1 for marks and μ_0 and σ_0 for spaces, then:

$$p_1(i_{dec}) = \frac{1}{\sqrt{2\pi\sigma_1^2}} \exp\left[-\frac{(i_{dec} - \mu_1)^2}{2\sigma_1^2} \right] \tag{3.2}$$

$$p_0(i_{dec}) = \frac{1}{\sqrt{2\pi\sigma_0^2}} \exp\left[-\frac{(i_{dec} - \mu_0)^2}{2\sigma_0^2} \right] \tag{3.3}$$

Substituting (3.2) and (3.3) into (3.1) thus yields:

$$\begin{aligned} P_{error} = \frac{1}{2}\int_{-\infty}^{I_{th}} \frac{1}{\sqrt{2\pi\sigma_1^2}} \exp\left[-\frac{(i_{dec} - \mu_1)^2}{2\sigma_1^2} \right] di_{dec} \\ + \frac{1}{2}\int_{I_{th}}^{\infty} \frac{1}{\sqrt{2\pi\sigma_0^2}} \exp\left[-\frac{(i_{dec} - \mu_0)^2}{2\sigma_0^2} \right] di_{dec} \end{aligned} \tag{3.4}$$

It can be shown [90] that (3.4) is minimised when:

$$\frac{(I_{th} - \mu_0)^2}{2\sigma_0^2} = \frac{(\mu_1 - I_{th})^2}{2\sigma_1^2} + \ln\left(\frac{\sigma_1}{\sigma_0}\right) \tag{3.5}$$

In most practical cases, the last term is negligible, and (3.5) reduces to:

$$\begin{aligned} \frac{I_{th} - \mu_0}{\sigma_0^2} &= \frac{\mu_1 - I_{th}}{\sigma_1^2} \\ &\equiv Q \end{aligned} \tag{3.6}$$

giving the optimal decision threshold value of:

$$I_{th} = \frac{\sigma_0\mu_1 + \sigma_1\mu_0}{\sigma_0 + \sigma_1} \tag{3.7}$$

Substituting (3.7) into (3.6) gives:

$$Q = \frac{\mu_1 - \mu_0}{\sigma_0 + \sigma_1} \tag{3.8}$$

The value Q is commonly referred to as the "Q-factor" and measures the distance (in terms of number of standard deviations) the threshold I_{th} is from the mean mark and

space levels. The Q-factor is closely linked with the BER, which can be shown by substituting (3.6) into (3.4) to yield:

$$\begin{aligned} P_{error} &= \frac{1}{\sqrt{\pi}} \int_{\frac{Q}{\sqrt{2}}}^{\infty} \exp(-x^2) dx \\ &= \frac{1}{2}\left[1 - \operatorname{erf}\left(\frac{\mathrm{Q}}{\sqrt{2}}\right)\right] \approx \frac{1}{\sqrt{2\pi}} \frac{\exp(-\frac{Q^2}{2})}{Q} \\ &= \mathrm{BER} \end{aligned} \tag{3.9}$$

where erf(x) is the error function:

$$\operatorname{erf}(x) = \frac{2}{\sqrt{\pi}} \int_0^x \exp(-y^2) dy \tag{3.10}$$

that can be found in tabulated form in mathematical handbooks [91] or through numerical integration. Typical operating BER levels range from 10^{-9} to 10^{-12} [92], but using forward error correction (FEC) technology, a system may be tolerate up to levels of 10^{-3}, corresponding to a Q-factor of 3 [93].

3.5 EYE CLOSURE PENALTY

Another widely used measurement is the "eye height", or the widest opening between the mark and space levels [86]. It is a convenient, experimentally measurable quantity that can easily be extracted from an eye diagram, mentioned in section 3.3. The eye height (*EH*) is defined, for NRZ waveforms, as the distance between β standard deviations below the mark level, and above the space level in an eye diagram:

$$\begin{aligned} EH &= (\mu_1 - \beta\sigma_1) - (\mu_0 + \beta\sigma_0) \\ &= (\mu_1 - \mu_0) - \beta(\sigma_1 + \sigma_0) \\ &= \Delta - \beta\Sigma \end{aligned} \tag{3.11}$$

where $\Delta = (\mu_1 - \mu_0)$, $\Sigma = (\sigma_1 + \sigma_0)$ and common values of β are 1 or 3 [86]. The eye height is related to the Q-factor. Increasing the difference between the mean $(\mu_1 - \mu_0)$ or decreasing the combined variances $(\sigma_1 + \sigma_0)$ of the mark and space levels, increases the eye height, and consequently from (3.8) the Q-factor (and hence the BER).

The "Eye Closure Penalty" (*ECP*) is defined as the ratio of the eye height at the transmitter (EH_T) and the receiver (EH_R), assuming for simplicity (but not necessarily) that the average power levels of the signal are equal (i.e. the net signal gain along the path is zero dB). Note that EH_T is given by placing the receiver immediately next to the transmitter.

$$\begin{aligned} ECP_{T,R} &= \frac{EH_T}{EH_R} \\ &= \frac{(\mu_{1,T} - \mu_{0,T}) - \beta(\sigma_{1,T} + \sigma_{0,T})}{(\mu_{1,R} - \mu_{0,R}) - \beta(\sigma_{1,R} + \sigma_{0,R})} \\ &= \frac{\Delta_T - \beta\Sigma_T}{\Delta_R - \beta\Sigma_R} \end{aligned} \tag{3.12}$$

$$ECP(\text{dB}) = 10\log\left(\frac{\Delta_T - \beta\Sigma_T}{\Delta_R - \beta\Sigma_R}\right) \tag{3.13}$$

The ECP measures the end-to-end effect of optical impairments on the eye height of a transmitted signal, but by itself does not relate to a particular BER - a given ECP (such as ECP = 3dB) may or may not correspond to an acceptable BER.

One benefit of the ECP is that its functional form is well known, or derived for several key impairments, for example ASE [92], RCD [94] and PMD [95]. This means that given a known value for an optical impairment, a value for ECP can be estimated without prior knowledge of the received eye diagram and statistics. It is also important to note that these relationships are dependent on system parameters such as bit rate, modulation format etc, so the appropriate relationships must be used for different systems.

3.6 LINKING ECP AND BER

Given that the ECP has strong relationships to optical impairments, and the most common measure of signal reliability is the BER, it is desirable to link the two. Begin by noting that the BER is calculated (under Gaussian statistical assumptions) using the Q-factor shown in (3.9), and that the Q-factor of a signal at node *m* can be rewritten from (3.8) as:

$$Q_m = \frac{\Delta_m}{\Sigma_m} \tag{3.14}$$

The average power of a signal at node *m* can be expressed as:

$$P_m = \frac{1}{R}\left(\frac{\mu_{1,m} + \mu_{0,m}}{2}\right) \tag{3.15}$$

where *R* includes the photodetector responsivity, receiver filtering and amplification. Let:

$$\frac{1}{r_m} = \frac{\mu_{1,m}}{\mu_{0,m}} \tag{3.16}$$

be the extinction ratio of the signal at node *m*, which for typical systems is 10dB or more, giving $r_m << 1$. Equation (3.15) can be rewritten, using (3.16) as:

$$\begin{aligned} P_m &= \frac{1}{R}\left(\frac{\mu_{1,m} + \mu_{0,m}}{2}\right)\left(\frac{\mu_{1,m} - \mu_{0,m}}{\mu_{1,m} - \mu_{0,m}}\right) \\ &= \frac{1}{2R}\Delta_m\left(\frac{\mu_{1,m} + \mu_{0,m}}{\mu_{1,m} - \mu_{0,m}}\right) \\ &= \frac{1}{2R}\Delta_m\left(\frac{1+r_m}{1-r_m}\right) \end{aligned} \tag{3.17}$$

Now, assuming that $r_m << 1$, and *R* is similar at each node, the net gain G_m of the signal at node *m* from node *n* is:

$$\begin{aligned} G_{n,m} &= \frac{P_m}{P_n} \\ &\approx \frac{\Delta_m}{\Delta_n} \end{aligned} \tag{3.18}$$

Substituting (3.14) and (3.18) into (3.12) thus yields the ECP between the transmitter node *T* and receiver node *R* as:

$$
\begin{aligned}
ECP_{T,R} &= \frac{\Delta_T - \beta\Sigma_T}{\Delta_R - \beta\Sigma_R} \\
&= \frac{\frac{\Delta_T}{\beta\Sigma_T} - 1}{\frac{\Delta_R}{\beta\Sigma_T} - \frac{1}{\beta\Sigma_T}\beta\frac{\Delta_R}{Q_R}} \\
&= \frac{\frac{1}{\beta}Q_T - 1}{\frac{1}{\beta}G_{T,R}\frac{\Delta_T}{\Sigma_T} - G_{T,R}\frac{\Delta_T}{\Sigma_T}\frac{1}{Q_R}} \\
&= \frac{Q_R(\frac{1}{\beta}Q_T - 1)}{\frac{1}{\beta}G_{T,R}Q_TQ_R - G_{T,R}Q_T} \\
&= \frac{Q_R(Q_T - \beta)}{G_{T,R}Q_T(Q_R - \beta)}
\end{aligned}
\tag{3.19}
$$

Finally, rearrangement of (3.19) gives:

$$
\text{Estimated } Q_R \approx \frac{\beta G_{T,R}Q_T ECP_{T,R}}{\beta + Q_T(G_{T,R}ECP_{T,R} - 1)} \tag{3.20}
$$

that allows the calculation of the Q-factor Q_R (and hence BER) at the receiver node, from the easily measureable transmitted Q-factor Q_T, the net path gain $G_{T,R}$ and the ECP of the candidate path, that can be estimated, a-priori, using link impairment values.

3.7 COMBINED EFFECT OF MULTIPLE OPTICAL IMPAIRMENTS

This thesis proposes that the ECP induced by individual optical impairments such as ASE, PMD and RCD can be combined in some way to obtain an a-priori estimate of overall ECP value, to be used in conjunction with (3.20) to estimate the Q-factor and hence, the BER for a connection in an all-optical network. This process assumes that the characteristics of individual links within the network are known and accessible either through a network management database, or real time optical monitoring techniques [96]. Such an estimate has direct application in routing in all-optical networks, as discussed in section 2.7, as well as network dimensioning and performance analysis, covered in later chapters.

To test this proposition, computer simulations were performed using a commercial package [97], firstly at linear operating powers with a single channel in the presence of the ASE, PMD and RCD optical impairments, and secondly with multiple

channels in the presence of optical crosstalk (intra-channel and inter-channel) and at nonlinear operating powers to include the effects of SPM, XPM and FWM. Full details of the simulation parameters are covered in the following sections.

3.7.1 LINEAR IMPAIRMENTS

Figure 3.7 details the simulation configuration to examine the properties of the ECP metric. This approach was used so that each of the degradations could be individually and independently varied. The simulation measures the statistics of the transmitted and received mark and space levels and Q-factor, in the presence of variable ASE, PMD and RCD.

The VPI simulation was set up such that the transmitter is an externally modulated laser using NRZ coding operating at 10 Gbit/s, with centre frequency of 193.1 THz and linewidth of 20 MHz that transmits a total of 2048 random marks and spaces with equal probability. The launch powers can be set to a value between 0 and -9 dBm and the extinction ratio was 14 dB.

The optical medium is 100km of single mode fibre (SMF) with signal attenuation of 0.2 dB/km, dispersion of 16 ps/nm·km at wavelength 1550 nm and dispersion slope of 0.08 ps/nm^2·km. The nonlinear coefficient and PMD in the fibre were set to zero. The fibre introduces a set amount of dispersion into the channel, which is then compensated by a variable length of dispersion compensating fibre (DCF) with 0 dB/km attenuation to set the final amount of RCD in the optical signal.

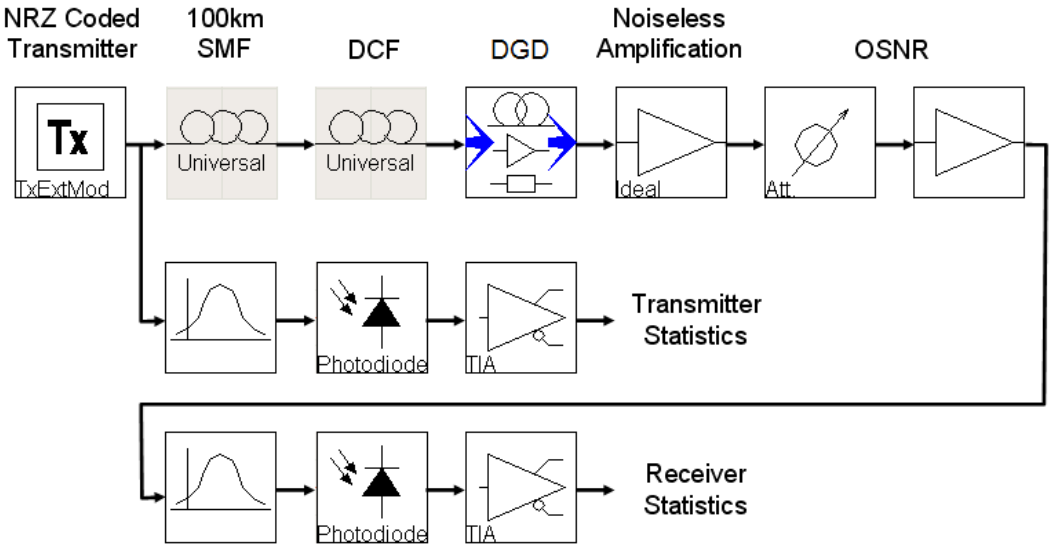

Figure 3.7: Simulation setup for linear impairments

The signal is then put through a PMD module that introduces a set amount of differential group delay (DGD) (in ps), at an angle of 45° to the principal axis of polarisation, and thus provides a worst case scenario PMD effect [98].

A noiseless amplifier is used to bring the signal power level back up to the launch level before the signal is then put through an attenuator of variable loss and then an amplifier of an equal amount of gain, but with a noise figure of 6 dB to add ASE, which is quantified using two power meters, one measuring the signal power, the other measuring noise power (not shown) to produce an OSNR measurement.

Both the launch (transmitted) signal and impaired (received) signal are passed through 5^{th} order Butterworth filters with centre frequency of 193.1 THz and 40Ghz bandwidth, and are then incident upon PIN photodiodes with responsivity of 1 A/W and thermal noise of 10 $pA/Hz^{½}$ then finally through transimpedence amplifiers to produce output voltages.

The mean and standard deviation of the mark and space voltage levels, as well as the Q-factor are measured for both the transmitted and received signals. These statistics enable the calculation of the transmitter and receiver eye heights and hence the ECP at various combinations of launch power, ASE (characterised by the "loss-gain" resulting in output OSNR), DGD and RCD as shown in Table 3.1. These parameter combinations resulted in 4800 data points.

Table 3.1: Linear impairment simulation parameters

Parameter	**Range of values**	**Increments**
Launch power	-9 dBm to 0 dBm	3 dBm
Loss-Gain	0 to 45 dB	5 dB
DGD	0 to 90 ps	10 ps
RCD	-320 to 1600 ps/nm	160 ps/nm

3.7.1.1 Q-FACTOR ESTIMATION USING ACTUAL ECP

The results of the simulations were processed to give values, at the receiver, for the actual Q-factor at the receiver, Q_R, using (3.8), and the actual ECP, $ECP_{T,R}$, using (3.12). Note that any reference to "actual" ECP refers to the ECP calculated from the measured values of $\mu_{1,T}$, $\mu_{0,T}$, $\mu_{1,R}$, $\mu_{0,R}$, $\sigma_{1,T}$, $\sigma_{0,T}$, $\sigma_{1,T}$, $\sigma_{0,T}$. An estimate of the Q-factor was then found using (3.20) with the appropriate values for Q_T and $G_{T,R}$. Figure 3.8 shows the result of plotting the actual Q-factor vs. the estimated Q-factor, with the values of $\beta = 1$ and $\beta = 3$. The solid red lines represent an ideal fit between the actual and estimated Q-factors, and the dotted grey lines represent an actual Q-factor of 3, which corresponds to the lower threshold at which forward error correction (FEC) technology [93] in modern optical communication systems can operate effectively to achieve reliable (e.g. BER < 10^{-12}) transmission of data.

Figure 3.8a shows that for $\beta = 1$, the Q-factor estimate given by (3.20) using the actual ECP consistently gives an underestimate of the actual Q-factor. As the actual Q-factor increases, the error increases significantly. At the critical value of actual Q-factor of 3, the estimated Q-factor has a mean of 2.17, standard deviation of 0.35, and ranges from 1.88 to 3.16. For $\beta = 3$, shown in Figure 3.8b, the results show much

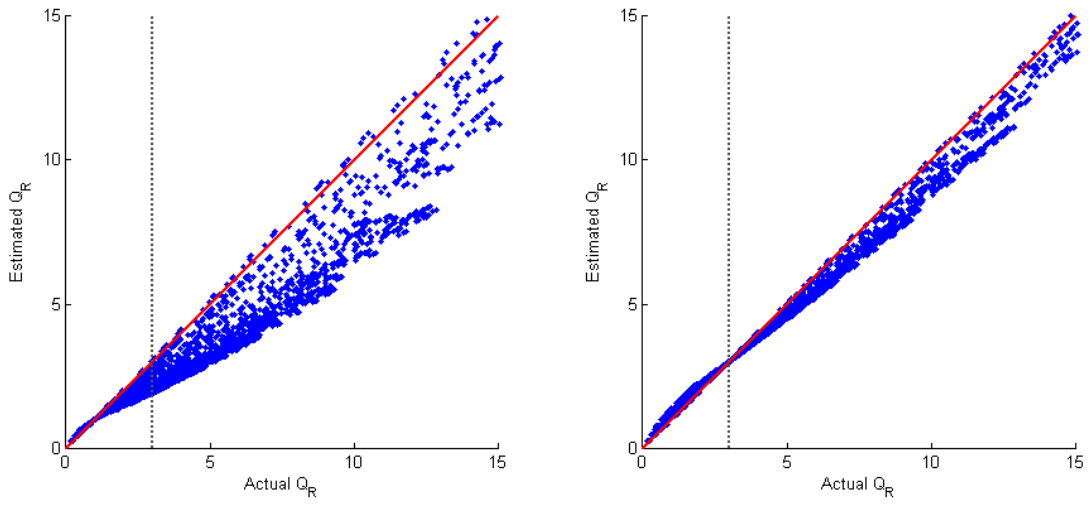

Figure 3.8: Estimated Q vs. actual Q at the receiver, for (a) β = 1 and (b) β = 3

better agreement and at the actual Q-factor of 3, the estimated Q-factor has a mean of 3.01, standard deviation of 0.04, and ranges from 2.92 to 3.09.

To determine the cause of the error between the actual Q_R and estimated Q_R, a 3 dimensional scatter plot, shown in Figure 3.9, was created for $\beta = 1$ that shows, via the colour of the point, the absolute value of the error, |actual Q_R – estimated Q_R|, as a function of the combination of the three linear impairments. The red points indicate a large amount of error, while the blue points indicate a small amount of error. It appears that in regions of low OSNR (corresponding to high levels of ASE), the error diminishes and the estimated from (3.20) is most accurate, regardless of the levels of DGD and RCD. However, as OSNR increases, and DGD and RCD dominate the overall contribution to the signal degradation, the error also increases.

This result is not unexpected. The derivation of the Q-ECP relationship in (3.20) relies on the fact that the Q-factor is calculated under the assumption that the mark

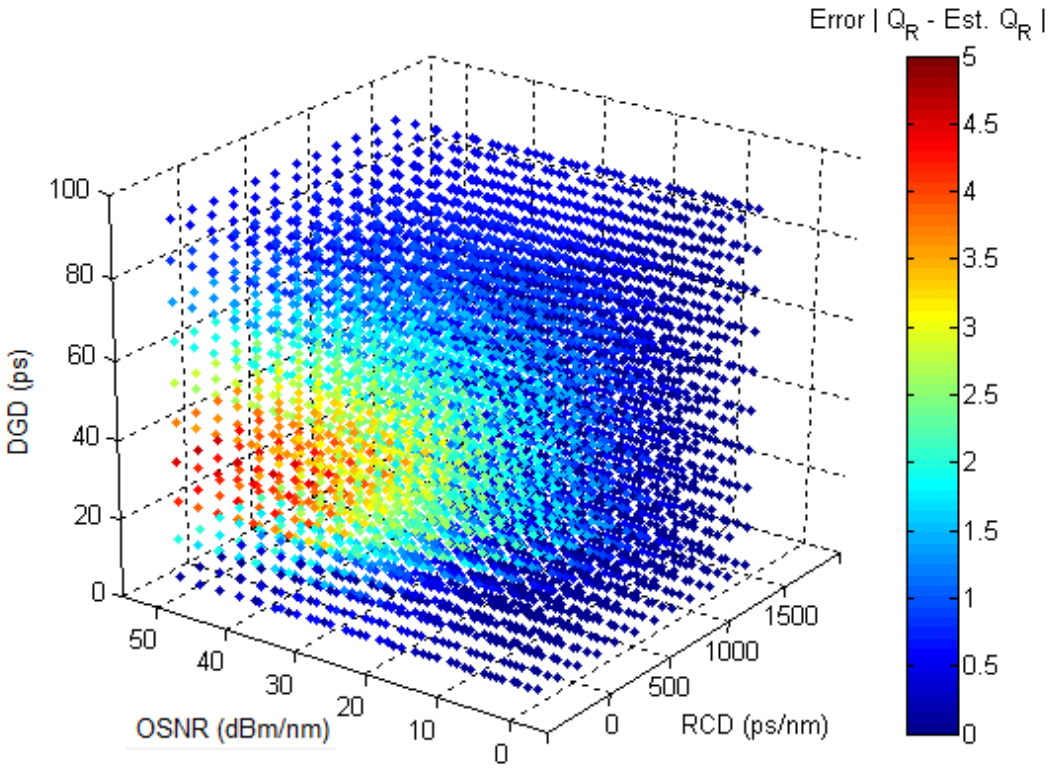

Figure 3.9: Error between actual Q_R and estimated Q_R as a function of individual impairments

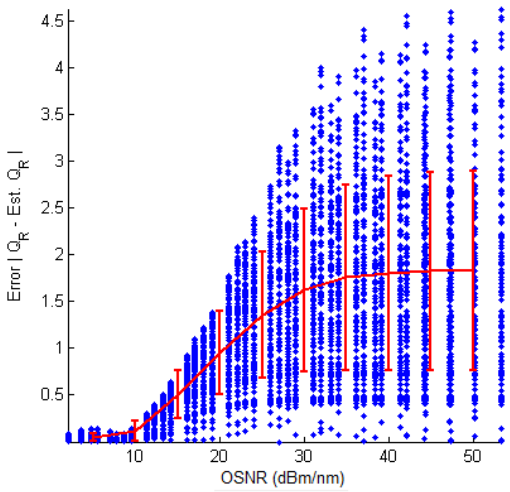

Figure 3.10: Error between actual Q_R and estimated Q_R as a function of OSNR

and space levels follow Gaussian distributions. ASE is also well represented by a Gaussian process [99] that affects the mean received mark and space levels – i.e. ASE increases the standard deviations $\sigma_{1,R}$ and $\sigma_{0,R}$. PMD and RCD are both waveform distortion effects, which interact with the receiver mark and space statistics in a more complicated manner.

Figure 3.10 plots the error for all points against OSNR, with the red line showing the mean error value and error bars of 1 standard deviation for points in a 5 dBm/nm bin around the plotted value. The plot reinforces our analysis, showing that when ASE is the dominant impairment (low OSNR), the estimate for Q_R becomes more and more accurate. Figure 3.11 plots the error in Q_R for individual impairments in the absence of the other two impairments (e.g. for OSNR, both DGD and RCD were zero),

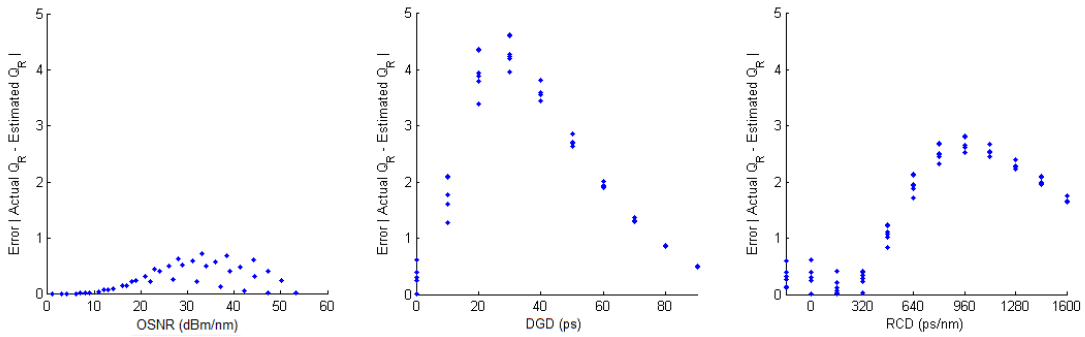

Figure 3.11: Error between actual Q_R and estimated Q_R as a function of individual impairments

showing that DGD and RCD contribute most significantly to the error.

3.7.1.1.1 EFFECT OF β ON Q_R USING ACTUAL ECP

Clearly, in Figure 3.8b, the parameter β has a significant effect on the accuracy of the estimated Q-factor, both reducing its spread, and upon further observation, determining the actual Q-factor value at which the minimum error, |actual Q_R – estimated Q_R|, occurs. This value appears to be at $Q_R = 1$ for $\beta = 1$, and $Q_R = 3$ for $\beta = 3$.

To understand why the spread of points is reduced as β is increased, consider (3.20), with (3.12) substituted for $ECP_{T,R}$:

$$\begin{aligned}\text{Estimated } Q_R &\approx \frac{\beta G_{T,R}\cdot Q_T\left[\dfrac{\Delta_T-\beta\Sigma_T}{\Delta_R-\beta\Sigma_R}\right]}{\beta+Q_T\left(G_{T,R}\left[\dfrac{\Delta_T-\beta\Sigma_T}{\Delta_R-\beta\Sigma_R}\right]-1\right)}\\ &= \frac{\beta G_{T,R}Q_T\left(\Delta_T-\beta\Sigma_T\right)}{\beta\left(\Delta_R-\beta\Sigma_R\right)+Q_T\left(G_{T,R}\Delta_T-\beta\Sigma_T-\Delta_R+\beta\Sigma_R\right)}\\ &= \frac{\beta G_{T,R}Q_T\Delta_T-\beta^2G_{T,R}Q_T\Sigma_T}{\beta\Delta_R-\beta^2\Sigma_R+Q_TG_{T,R}\Delta_T-Q_T\beta\Sigma_T-Q_T\Delta_R+\beta Q_T\Sigma_R}\end{aligned} \tag{3.21}$$

Taking the limit as $\beta \to \infty$ of the estimated Q_R and using (3.14) gives:

$$\begin{aligned}\lim_{\beta\to\infty}\left(\text{Estimated } Q_R\right) &= \frac{G_{T,R}Q_T\Sigma_T}{\Sigma_R}\\ &= G_{T,R}\frac{\Delta_T}{\Sigma_R}\end{aligned} \tag{3.22}$$

Under the assumption that the net path gain $G_{T,R} \approx 1$, and that the transmitter and receiver mean mark and space levels are similar so that $\Delta_T \approx \Delta_R$, (3.22) becomes:

$$\begin{aligned}\lim_{\beta\to\infty}\left(\text{Estimated } Q_R\right) &\approx \frac{\Delta_R}{\Sigma_R}\\ &= Q_R\end{aligned} \tag{3.23}$$

Equation (3.23) demonstrates that an increase in β generally results in a convergence of the estimated Q_R to the actual Q_R. To see why the error seems to be at a minimum

when the actual $Q_R \approx \beta$, consider (3.21) with $\beta = Q_R$ and $\Delta_R = Q_R\Sigma_R$ from (3.14), under the same assumption that $G_{T,R} \approx 1$.

$$\begin{aligned}\text{Estimated } Q_R &\approx \frac{\beta G_{T,R} Q_T\left(\Delta_T - \beta\Sigma_T\right)}{\beta\left(\Delta_R - \beta\Sigma_R\right) + Q_T\left(G_{T,R}\Delta_T - \beta\Sigma_T - \Delta_R + \beta\Sigma_R\right)} \\ &= \frac{Q_R Q_T\left(\Delta_T - Q_R\Sigma_T\right)}{Q_R\left(\Delta_R - Q_R\Sigma_R\right) + Q_T\left(\Delta_T - Q_R\Sigma_T - \Delta_R + Q_R\Sigma_R\right)} \\ &= \frac{Q_R Q_T\left(\Delta_T - Q_R\Sigma_T\right)}{Q_R\left(\Delta_R - \Delta_R\right) + Q_T\left(\Delta_T - Q_R\Sigma_T - \Delta_R + \Delta_R\right)} \\ &= \frac{Q_R Q_T\left(\Delta_T - Q_R\Sigma_T\right)}{Q_T\left(\Delta_T - Q_R\Sigma_T\right)} \\ &= Q_R\end{aligned} \tag{3.24}$$

The results illustrated by (3.23) and (3.24) indicate that while increasing β decreases the spread of the Q-ECP relationship, it also increases the value of actual Q_R for which the relationship is most accurate, so a careful choice of β should be made depending on the critical values of Q_R that are required for a "reliable" correlation.

3.7.1.2 ESTIMATION OF ECP

With the properties of the Q-factor estimate established, this section is focused on the properties and estimation of the ECP parameter, both (i) as a function of individual optical impairments, and (ii) subsequently as an overall measure of signal degradation with respect to multiple simultaneously occurring optical impairments. Additionally, it should be remembered that the overall ECP is to be used as an input parameter in the Q-ECP relationship established in (3.20) to estimate the Q-factor, and subsequently, the BER. A key benefit of the ECP parameter is that it exhibits known relationships with various optical impairments, such as ASE (via OSNR) [92], RCD [94]and DGD [95].

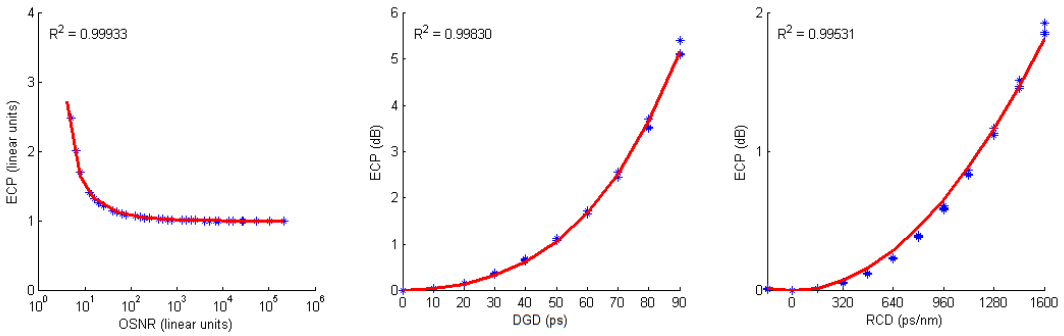

Figure 3.12: Estimated ECP from individual impairments, with β = 1.

The gathered data set was filtered to extract the ECP contribution of individual impairments in the absence of other impairments, and plotted in Figure 3.12. Negative values of ECP were filtered out. These occur when $Q_R \leq 1$ where a connection would be unusable in any case. For DGD and RCD, the values of ECP are in dB, and for OSNR, both axes are in linear units. The red line depicts a curve fit using the equations from Table 3.2 and correlation coefficients R^2 are shown in Figure 3.12. There is excellent agreement with the curve fit equations, with $R^2 > 0.99$ for all impairments, demonstrating that the ECP can be accurately predicted from the values of individual impairments.

It is hypothesised that these individual ECP values can be combined to give an overall value for ECP that represents the total degradation experienced by an optical signal under the influence of all three impairments.

Table 3.2: Linear impairment curve fit equations and constants for β = 1.

Impairment	Curve Fit Equation	Constants
ASE	$ECP_{ASE} = \left(A_1 \left(\frac{A_2}{OSNR} \right)^{A_3} \right)^{-1}$	$A_1 = 2.700270$ $A_2 = 0.497971$ $A_3 = 0.695772$
PMD	$ECP_{PMD}(dB) = B_1 \left(DGD\right)^4 + B_2 \left(DGD\right)^2$	$B_1 = 0.0000000382032$ $B_2 = 0.000327143$
RCD	$ECP_{RCD}(dB) = C_1 \left(RCD\right)^2$	$C_1 = 0.000000708099$

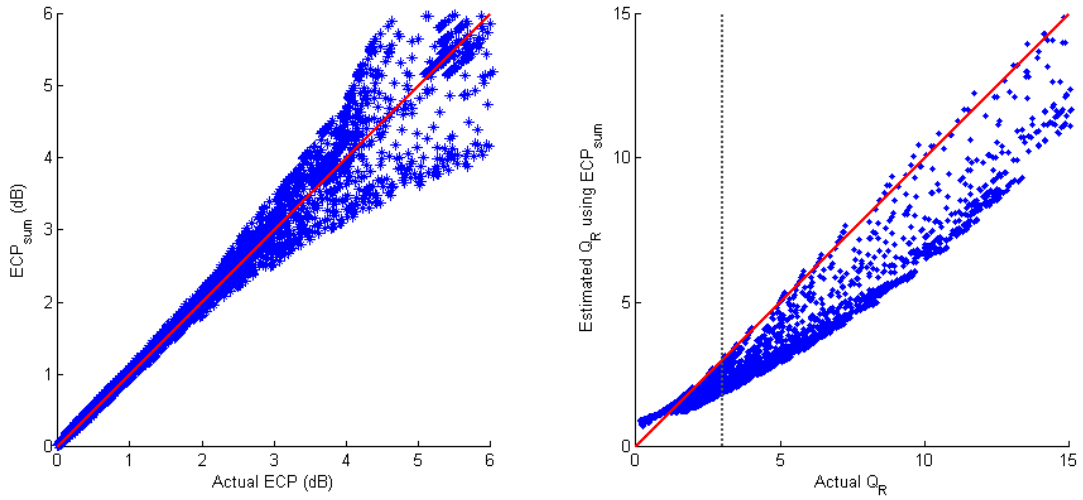

(a) (b)

Figure 3.13: (a) Actual ECP vs. ECP_{sum} , with β = 1, (b) Actual Q_R vs. Estimated Q_R using ECP_{sum}

The most simple of these combination methods is to assume that each degradation is independent of the others, and use scalar addition of individual ECP values (in dB) such that:

$$ECP_{sum}(dB) = ECP_{ASE}(dB) + ECP_{PMD}(dB) + ECP_{RCD}(dB) \qquad (3.25)$$

This corresponds to multiplication of the ECP values in linear units. Figure 3.13a shows a plot of the actual ECP calculated directly from the received mark and space data in the presence of the three impairments against the estimated total ECP, denoted ECP_{sum}. It can be seen that there is excellent agreement between the actual and estimated overall ECP values where the actual ECP < 3 dB, with a general loss of accuracy at higher values. Figure 3.13b shows the effect of using ECP_{sum} as $ECP_{T,R}$ in (3.20). Compared with Figure 3.8, the fit between the actual Q_R and estimated Q_R is very similar, with the estimated Q_R almost always being an underestimate of the actual Q_R, particularly in the critical region for FEC operation where actual $Q_R \approx 3$.

The results show that it is possible to provide an estimate (albeit a rough underestimate) of the Q-factor, and hence the BER, from multiple optical impairments by making use of the ECP signal degradation metric. The next step is to tune the estimate to give better agreement between the estimated Q_R and actual Q_R.

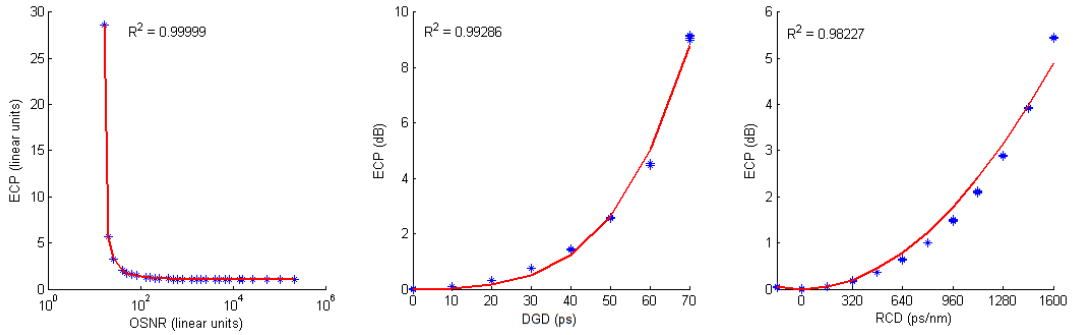

Figure 3.14: Estimated ECP from individual impairments, with $\beta = 3$.

3.7.1.2.1 EFFECT OF β ON Q_R USING ESTIMATED ECP

As shown previously, increasing the parameter β has the effect of reducing the error between the estimated Q_R and actual Q_R when using the actual ECP value, so in an attempt to improve the fit between the two, the calculations and curve fits were repeated using a value of $\beta = 3$.

An important observation when performing these calculations was that many more of the values for the actual ECP that were positive when $\beta = 1$ became negative when $\beta = 3$, and the general values for ECP were quite large in comparison. For example, in the PMD plot in Figure 3.14 the ECP value at a PMD of 70 ps is approximately 9 dB when $\beta = 3$, compared to 2.5 dB when $\beta = 1$. Additionally, the ECP values were negative (and omitted for curve fitting purposes) for PMD values of 80 and 90 ps and many lower values of OSNR. This adversely affects the curve fitting process, with

Table 3.3: Linear impairment curve fit equations and constants for $\beta = 3$.

Impairment	Curve Fit Equation	Constants
ASE	$ECP_{ASE} = \left(A_1 \left(\frac{A_2}{OSNR} \right)^{A_3} \right)^{-1}$	$A_1 = 3.06181$ $A_2 = 3.01193$ $A_3 = 0.69743$
PMD	$ECP_{PMD}(dB) = B_1 (DGD)^4 + B_2 (DGD)^2$	$B_1 = 0.000000313914$ $B_2 = 0.000259449$
RCD	$ECP_{RCD}(dB) = C_1 (RCD)^2$	$C_1 = 0.00000191944$

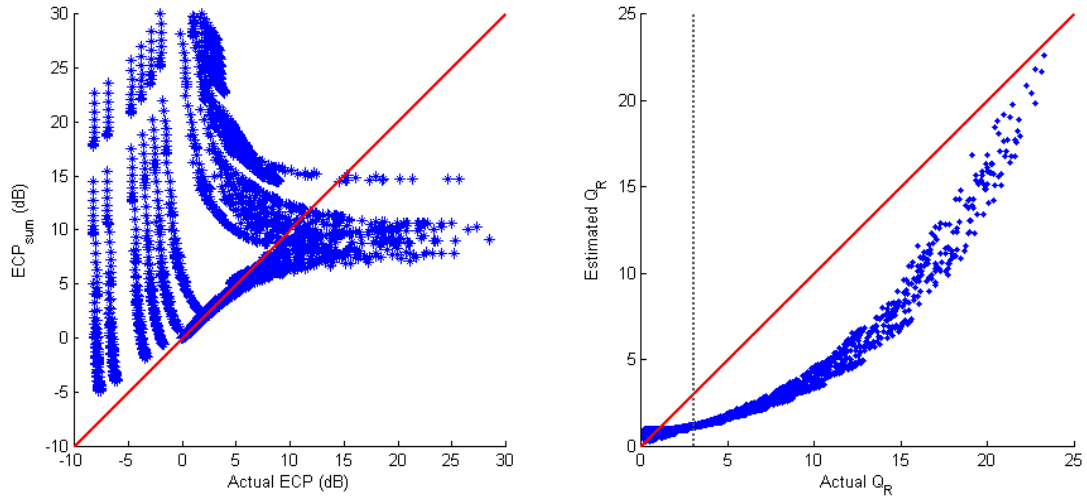

(a) (b)

Figure 3.15: (a) Actual ECP vs. ECP_{sum} , with $\beta = 3$, (b) Actual Q_R vs. Estimated Q_R using ECP_{sum}

more values of ECP needing to be extrapolated rather than interpolated from impairment values. The curve fit constants for $\beta = 3$ are shown in Table 3.3. Another problem is the non-Gaussian nature of RCD and PMD. Using $\beta = 3$ will severely overestimate the ECP, or underestimate the receiver eye height.

From these ECP curve fits, the ECP_{sum} approximation was calculated using (3.25) and shown in Figure 3.15a, and the corresponding estimated Q_R shown in Figure 3.15b. Evidently, the choice of $\beta = 3$ does not provide a good estimate of the actual Q_R.

To understand why this might be the case, recall that the definition of the ECP in (3.12) is the ratio of the transmitter eye height to the receiver eye height. With a larger value of β, there are many more instances for which the receiver eye height (calculated as $\Delta_R - \beta\Sigma_R$) may be close to zero, when $\Delta_R \approx \beta\Sigma_R$, causing $ECP_{T,R}$ to be large, or even negative, when $\beta\Sigma_R > \Delta_R$. These factors degrade the quality of the ECP curve fits that break down with negative and asymptotically large ECP values.

It was also observed that using $\beta = 3$ increases the magnitude of the actual ECP values calculated, in some cases by 2 orders of magnitude, over the same ECP values calculated where $\beta = 1$. This increase is likely to result in the ECP_{sum} from (3.25) being an overestimate of the actual ECP, which in turn would result in a large

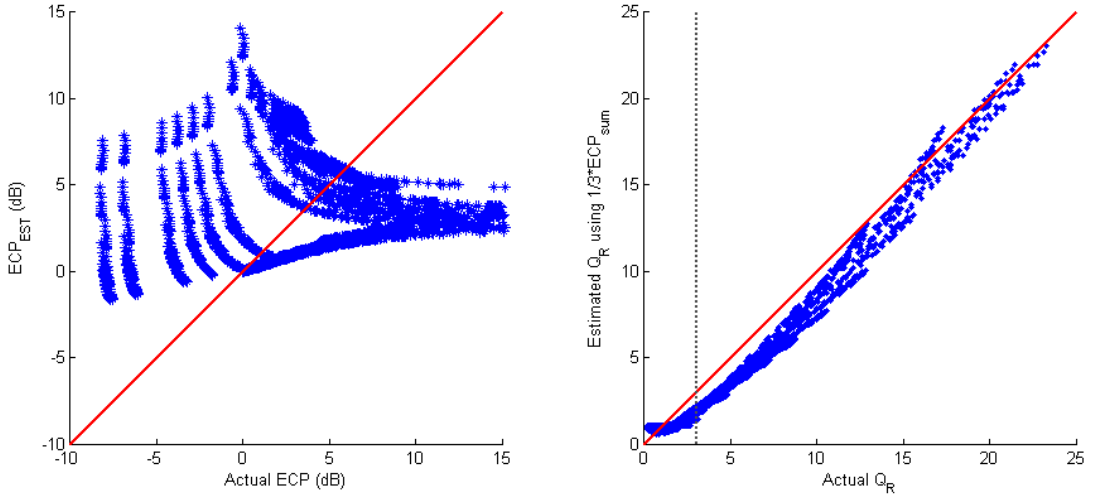

(a) (b)

*Figure 3.16: (a) Actual ECP vs. 1/3*ECP_{sum} , with β = 3,*
*(b) Actual Q_R vs. Estimated Q_R using 1/3*ECP_{sum}*

underestimate of the actual Q_R by the estimated Q_R, which is consistent with the data observed in Figure 3.15b.

To test this hypothesis, (3.25) was intuitively modified such that:

$$\begin{aligned} ECP_{sum}(dB) &= \frac{1}{\beta}\left(ECP_{ASE}(dB) + ECP_{PMD}(dB) + ECP_{RCD}(dB)\right) \\ &= \frac{1}{3}\left(ECP_{ASE}(dB) + ECP_{PMD}(dB) + ECP_{RCD}(dB)\right) \end{aligned} \tag{3.26}$$

Figure 3.16b shows a plot of the actual Q_R and the estimated Q_R using the ECP_{sum} value obtained from (3.26), and shows a much better fit. This is interesting because Figure 3.16a shows that many of the (1/3) × ECP_{sum} values do not in fact match the actual ECP values.

These results imply that it is not necessary to find a good estimate for the actual ECP in order to obtain a good estimate of the actual Q_R, but rather that it is more important to tune the estimated ECP that in turn gives a good estimate for Q_R.

3.7.1.2.2 FITTING ECP TO OBTAIN A BETTER ESTIMATE OF Q_R

The flow chart in Figure 3.17 is intended as a brief review of the insights gained in the previous sections. For clarity, the yellow shaded boxes indicate those quantities that can be gathered, or calculated, a-priori to setting up a network connection, while the blue boxes indicate simulation data or quantities that can only be calculated from received statistics after a connection has been established. The labels on the arrows indicate which equations or techniques should be used to compute the next quantities.

Recall the following from previous sections:

- The actual ECP values, when transformed to actual Q_R values, do not necessarily give a good fit. The error between the estimated Q_R and actual Q_R values depends on which impairment is dominant, shown in Figure 3.11.
- The estimated ECP values have clear, well defined relationships with impairment values, shown in Figure 3.12.
- The sum of ECP values (in dB), gives a decent approximation of the actual ECP values, particularly for $\beta = 1$, shown in Figure 3.13.

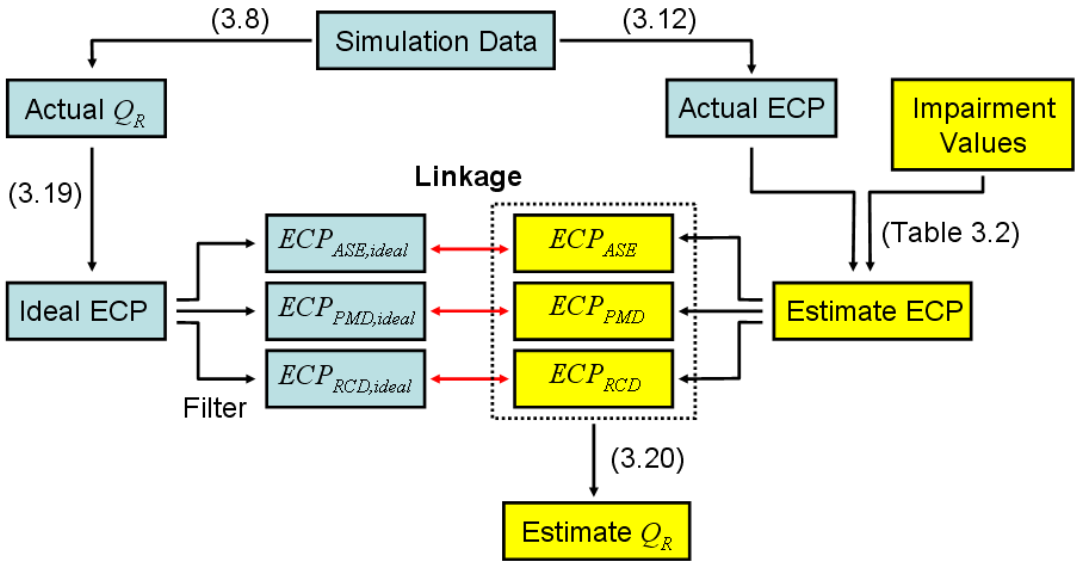

Figure 3.17: Overview of steps to estimate ECP.

- Scaling the ECP values (in dB) can provide a better fit for the estimated Q_R, as shown in Figure 3.16b, even if the estimated ECP does not match the actual ECP.

The presented evidence suggests that a more productive method of estimating the actual Q_R might be to obtain a linkage between the estimated ECP value (found using the methods described above in this chapter), and the *ideal* ECP. The "ideal ECP" is defined as the ECP value that gives the correct value for the actual Q_R. It is found using (3.19), which is the reverse transformation of (3.20) used to estimate Q_R from the estimated ECP. In reality, the value of Q_R is not generally known a-priori unless pre-calibration of the system is performed, but in simulations this is not the case.

To test this hypothesis, for each individual impairment, a plot was made between the estimated ECP values (in linear units), obtained using the equations in Table 3.2 and

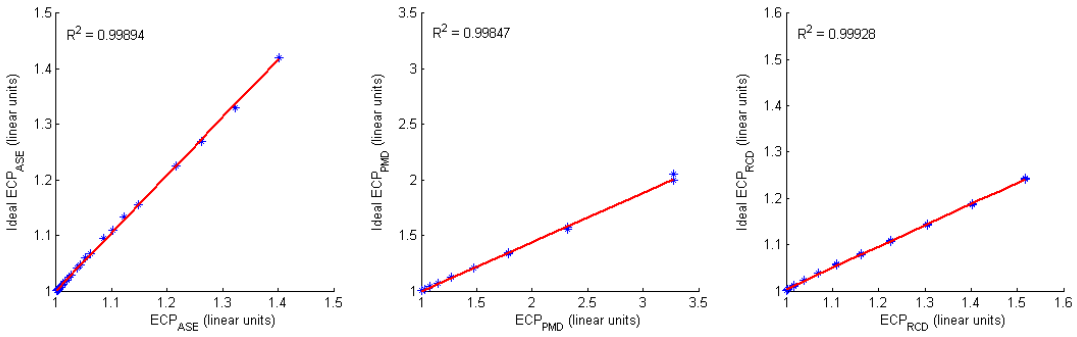

Figure 3.18: Relationship between ideal ECP and estimated ECP, with β = 1

Table 3.4: Curve fits between estimated ECP and ideal ECP for individual impairments, β = 1

Impairment	Curve Fit Equation	Constants
ASE	$ECP_{ASE,ideal} = A_1 ECP_{ASE} + A_2$	$A_1 = 1.04187$ $A_2 = -0.0413175$
PMD	$ECP_{PMD,ideal} = B_1 ECP_{PMD} + B_2$	$B_1 = 0.440190$ $B_2 = 0.559658$
RCD	$ECP_{RCD,ideal} = C_1 ECP_{RCD} + C_2$	$C_1 = 0.459325$ $C_2 = 0.544457$

using β = 1 because this gives better results for the estimated ECP values, and the ideal ECP values obtained using the actual Q_R and (3.19). The results are shown in Figure 3.18 for each of the individual impairments. Here, the red line represents a linear curve fit, with the fitted parameters being reported in Table 3.4, with high correlation coefficients where $R^2 > 0.998$ for all impairments.

Thus, it appears possible to transform the initial estimated ECP values for each of the impairments (obtained using curve fits from actual impairment values), into new ECP values:

$$ECP_{ASE,fitted} = 1.04187 ECP_{ASE} - 0.0413175 \tag{3.27}$$

$$ECP_{PMD,fitted} = 0.440190 ECP_{PMD} + 0.559658 \tag{3.28}$$

$$ECP_{ASE,fitted} = 0.459325 ECP_{ASE} + 0.544457 \tag{3.29}$$

Combining these using multiplication in the linear units, equivalent to addition in dB, gives:

$$ECP_{fit} = ECP_{ASE,fitted} \times ECP_{PMD,fitted} \times ECP_{RCD,fitted}$$
$$or \tag{3.30}$$
$$ECP_{fit}(dB) = ECP_{ASE,fitted}(dB) + ECP_{PMD,fitted}(dB) + ECP_{RCD,fitted}(dB)$$

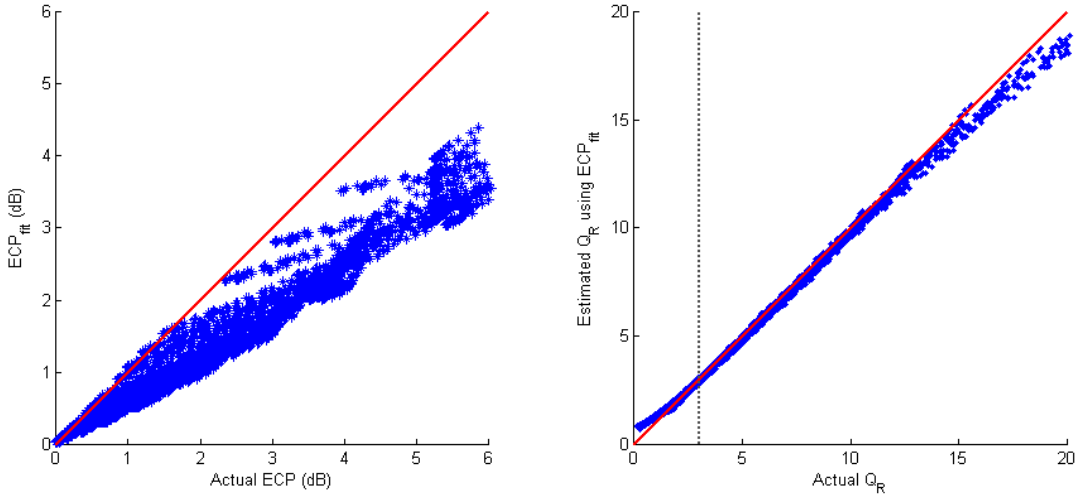

(a) (b)

Figure 3.19: (a) Actual ECP vs. ECP_{fit} , with β = 1, (b) Actual Q_R vs. Estimated Q_R using ECP_{fit}

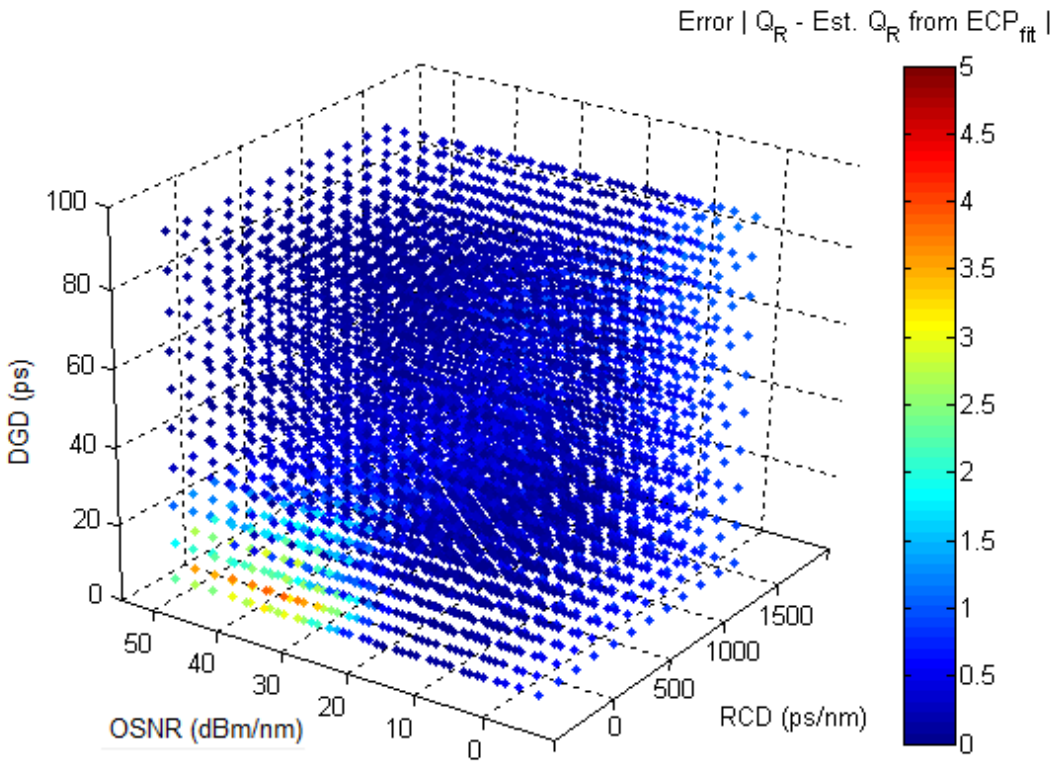

Figure 3.20: Error between actual Q_R and estimated Q_R using ECP_{fit}

Figure 3.19a shows a plot of the actual ECP with ECP_{fit} where clearly, ECP_{fit} provides an underestimate of the actual ECP. Figure 3.19b shows a plot of the actual Q_R against the estimated Q_R using ECP_{fit} obtained from (3.30), showing excellent agreement. Figure 3.20 displays the error between the actual Q_R and estimated Q_R and shows that there is a small amount of error in the region where the OSNR is high, and there is a small amount of RCD present.

Table 3.5: Error statistics between actual Q_R and estimated $Q_{R,fit}$, $\beta = 1$

Actual Q_R range	**Mean (Q_R – Est. $Q_{R,fit}$)**	**Variance (Q_R – Est. $Q_{R,fit}$)**
$Q_R > 8$	0.4516	0.2338
$Q_R \leq 8$	**0.0389**	**0.0185**

Statistical analysis of the error for all the data points is summarised in Table 3.5 for different regions of actual Q_R. For routing purposes, the region where $Q_R < 8$ is considered to be the most important and this is where the estimate is most accurate.

The fact that there exists a linear transformation between the ideal ECP and the actual ECP, shown in Figure 3.18, suggests that it should be possible to perform a fit between the individual impairment values and the ideal ECP values, rather than between the impairment values and the actual ECP values, which was done to produce Figure 3.12. This process intrinsically accounts for the linear transformation between the ideal and actual ECP values, eliminating the need to compute the actual ECP values from the data.

This new, more efficient method for computing the estimated Q_R is summarised in Figure 3.21, with boxes shaded in blue indicating quantities that are calculated in an "offline" phase and yellow shaded boxes indicating quantities calculated in real-time, or "online", a-priori to a connection establishment.

The "data" can be gathered from simulations as has been done in this thesis, or from calibrated sweeps of individual impairments whilst recording the mark and space mean and variance levels. From these sweeps, the Q_R and ideal ECP are computed using (3.8) and (3.19) for each impairment. This data is then fitted using the

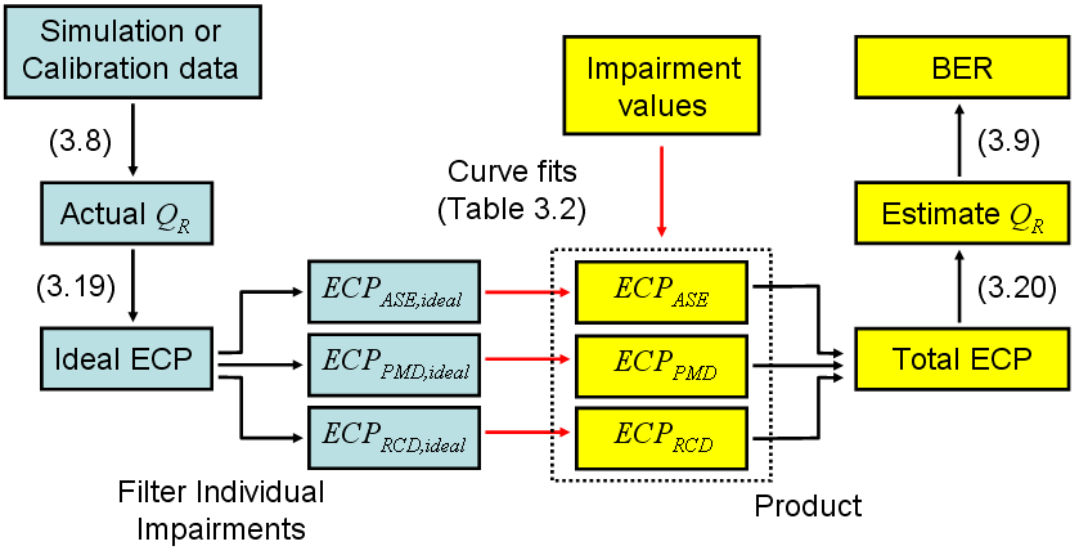

Figure 3.21: Process to estimate Q_R using the ECP.

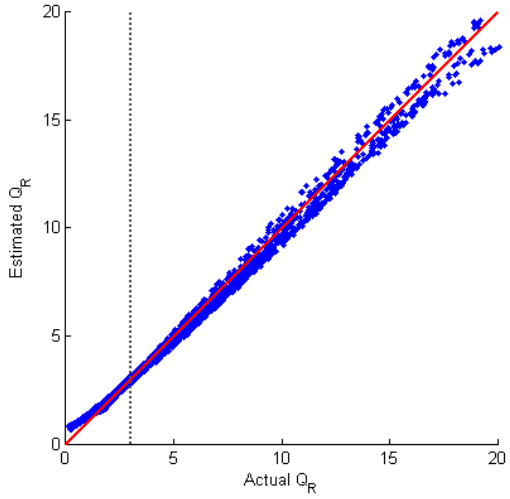

Figure 3.22: Actual Q_R vs. estimated Q_R using ideal ECP

relationships described in Table 3.2 to obtain the constants required to compute the estimated ECP values, from the measured and monitored individual impairment values. These ECP values are combined via multiplication in the linear domain or addition in dB to give the overall estimated ECP which is then used to calculate the estimated received Q_R using (3.20) and hence BER using (3.9).

Using this process, very similar results were obtained to those in Figure 3.19, shown in Figure 3.22. The fact that the very simple relationship given by (3.25), where the total ECP is the product of individual impairment ECPs, yields such good agreement between the estimated and actual Q_R reinforces that the effects of the three linear impairments - ASE, PMD and RCD – on signal quality are, for the purpose of estimating the total signal degradation, indeed independent of each other.

Table 3.6: Error statistics between actual Q_R and estimated $Q_{R,fit}$, using ideal ECP

Actual Q_R range	**Mean (Q_R – Est. $Q_{R,fit}$)**	**Variance (Q_R – Est. $Q_{R,fit}$)**
$Q_R > 8$	0.3486	0.2867
$Q_R \leq 8$	**-0.0343**	**0.0575**

3.7.1.2.3 40 GBIT/SEC AND 100 GBIT/SEC SYSTEMS

To this point, all results have been obtained using system bit rates of 10 Gbit/sec. Practical future systems are expected to operate at 40 Gbit/sec and 100 Gbit/sec, so simulations were run to ascertain whether the developed Q-factor estimation method was applicable to higher bit rate systems. These systems had a much lower tolerance to PMD and RCD, an expected result [101], because the pulse spreading caused by these effects occupy a much larger proportion of the width of a single bit resulting in inter-symbol interference. The system parameters are listed in Table 3.7.

Table 3.7: Simulation parameters for 40 Gbit/sec and 100Gbit/sec systems

Bit Rate	**40 Gbit/sec**		**100 Gbit/sec**	
Parameter	**Range**	**Increments**	**Range**	**Increments**
Launch power	-9 dBm to 0 dBm	3 dBm	-9 dBm to 0 dBm	3 dBm
Loss-Gain	0 to 45 dB	5 dB	0 to 45 dB	5 dB
DGD	0 to 27 ps	3 ps	0 to 18 ps	2 ps
RCD	-30 to 80 ps/nm	10 ps/nm	0 to 10 ps/nm	1 ps/nm

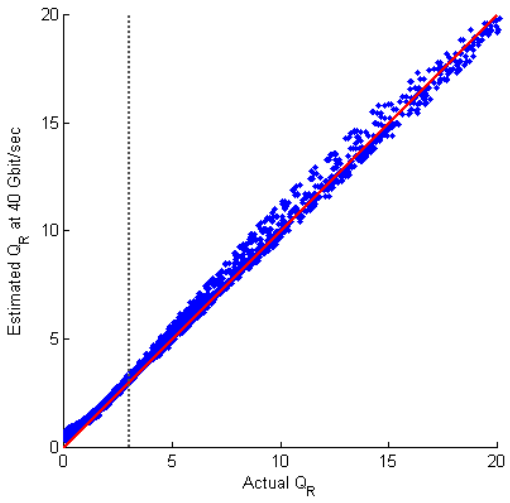

Figure 3.23: Actual Q_R vs. estimated Q_R at system rate 40 Gbit/sec

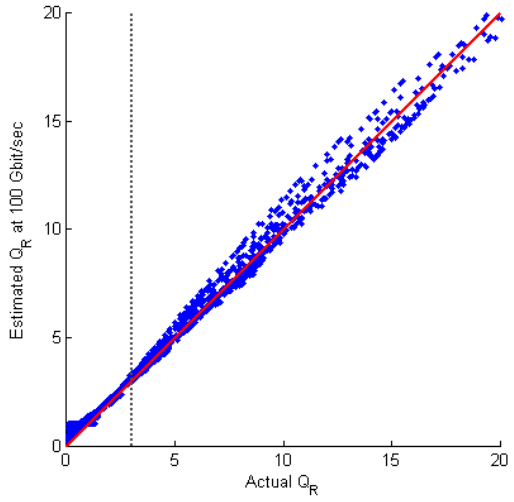

Figure 3.24: Actual Q_R vs. estimated Q_R at system rate 100 Gbit/sec

The process in Figure 3.21 was used to calculate the estimated Q_R, and statistics of the error between the estimated Q_R and actual Q_R were computed as in previous sections.

A comparison between the actual Q_R and estimated Q_R for a system bit rate of 40 Gbit/sec is shown in Figure 3.23 and the corresponding statistics for the error between the two is shown in Table 3.8.

In this case, the curve fit between the ideal ECP and the DGD was found to best fit a 6^{th} order polynomial, while the best fit between the ideal ECP and the RCD was found to be a 4^{th} order polynomial.

Note that in this case, most of the data points lie above the "ideal" red line and the mean error (Actual Q_R – Estimated Q_R) is negative, indicating that the estimated Q_R can provide an overestimate of the actual Q_R. In cases like these, it may be beneficial to apply a slight correction factor (e.g. $Q_{R,corrected} = Q_{R,fit} - k$, where k is a constant) to

Table 3.8: Error statistics between actual Q_R and estimated $Q_{R,fit}$, for 40 Gbit/sec, $\beta = 1$

Actual Q_R range	**Mean (Q_R – Est. $Q_{R,fit}$)**	**Variance (Q_R – Est. $Q_{R,fit}$)**
$Q_R > 8$	-0.0814	0.2621
$Q_R \leq 8$	**-0.1282**	**0.0278**

the estimated Q_R to ensure that it provides a worst case (underestimate) approximation to the actual Q_R.

Figure 3.24 shows the results, and Table 3.9 the error statistics, of the Q-factor estimation process for linear impairments in a system with bit rate of 100 Gbit/sec. The data points are more concentrated toward lower Q_R values, and there is more spread at higher values. The 100 Gbit/sec system is extremely sensitive to inter-symbol interference caused by PMD and RCD, with the best curve fits for these parameters found to be 6th order and 4th order polynomials respectively as in the 40 Gbit/sec case.

In theory, the higher order polynomials that relate the ECP to the DGD and RCD for the 40 Gbit/sec and 100 Gbit/sec simulations may also hold for 10 Gbit/sec, with some scaling factor for the polynomial co-efficients related to the bit rate. This could be further investigated in future work.

The results for both the 40 Gbit/sec and 100 Gbit/sec simulations demonstrate that the method developed to estimate the Q-factor from multiple linear optical impairments with NRZ coding, is applicable to higher bit-rate systems.

The next section aims to extend the developed Q-factor estimation method to include the effect of intra-channel and inter-channel crosstalk from optical switching elements.

Table 3.9: Error statistics between actual Q_R and estimated $Q_{R,fit}$, for 100 Gbit/sec, $\beta = 1$

Actual Q_R range	**Mean (Q_R – Est. $Q_{R,fit}$)**	**Variance (Q_R – Est. $Q_{R,fit}$)**
$Q_R > 8$	0.0069	0.4075
$Q_R \leq 8$	**-0.0030**	**0.0420**

3.7.2 CROSSTALK

To this point, only the three main linear impairments – ASE, PMD and RCD – have been considered in the estimation of the Q-factor from multiple optical impairments. This section extends the methodology established in section 3.7.1 to include the effects of inter-channel and intra-channel crosstalk introduced in network switching elements such as ROADMs.

To model these additional noise effects, the simulation setup in Figure 3.7 was extended to include:

- an intra-channel crosstalk noise source with associated attenuator,
- an array of additional transmitters acting as inter-channel crosstalk noise sources,
- an ideal WDM multiplexer, and
- a de-multiplexer using a trapezoidal bandpass transfer function to extract the reference channel, with variable stop band attenuation.

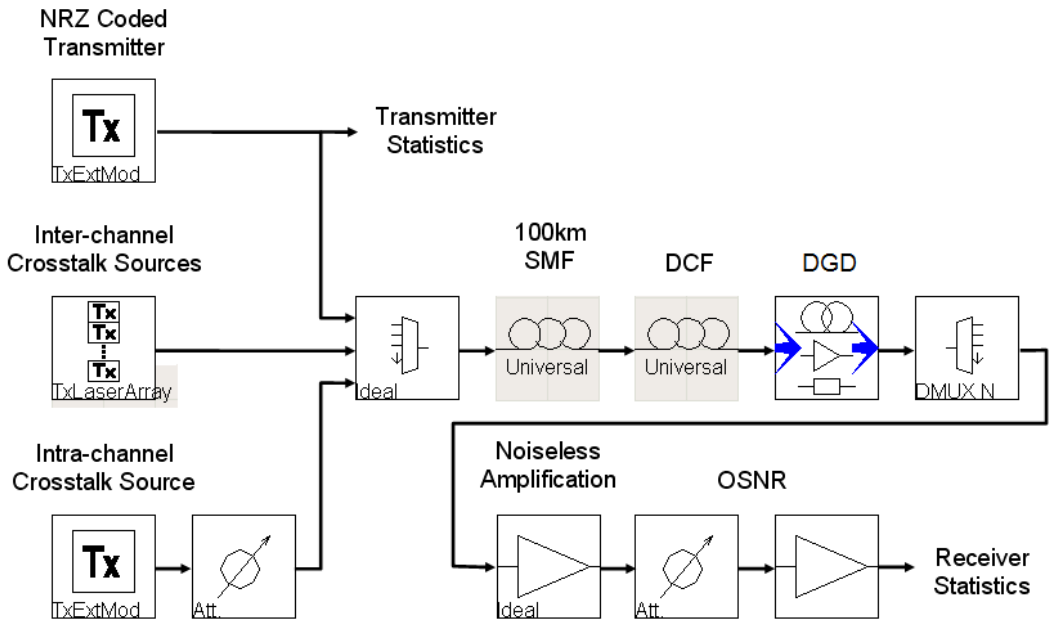

Figure 3.25: Simulation setup for crosstalk and non-linear impairment analysis

Combined with the additional transmitters, the de-multiplexer enables the modelling of inter-channel crosstalk at various levels by varying the stop band attenuation level. Intra-channel crosstalk is introduced at various levels by the intra-channel source and attenuator. The transmitted bit patterns for crosstalk sources were unrelated to the reference source.

In these simulations, the additional transmitters were equally spaced 100 GHz above and below the reference transmitter that operated at 193.1 THz with line width 20 MHz, and all channels transmitted at the same optical power levels. The intra-channel crosstalk source operated at 193.1 THz, the same frequency as the reference transmitter, but with a power level reduced from the reference transmitter power level by the variable attenuator.

Note that while the launch powers extended into the non-linear range, non-linear effects were switched off in the fibres for the crosstalk simulations. Table 3.10 summarises the parameters of the simulation and the range of levels that were used.

Table 3.10: Intra-channel and inter-channel crosstalk, and non-linear effects simulation parameters

Bit Rate	**10 Gbit/sec**	
Parameter	**Range**	**Increments**
Launch power	0 dBm to 9 dBm	3 dBm
Loss-Gain	0 to 40 dB	10 dB
DGD	0 to 100 ps	10 ps
RCD	-320 to 1600 ps/nm	320 ps/nm
Intra-channel crosstalk	None, and 15 dB to 35 dB below launch power	5 dB
Inter-channel crosstalk	None, and 15 dB to 35 dB below launch power	5 dB
Additional transmitters	0 to 8	2

3.7.2.1 INTRA-CHANNEL CROSSTALK

To examine the effect of intra-channel crosstalk, the results were extracted so that there was zero ASE, PMD and RCD, with no additional transmitters and hence no inter-channel crosstalk. This left the intra-channel crosstalk as the only impairment. The intra-channel crosstalk was measured as a ratio between the crosstalk power and the signal power in linear units (InXT), and plotted against the corresponding ideal ECP value, with the results shown in Figure 3.26. Mathematically:

$$InXT = \frac{P_{XT,\lambda}}{P_{sig}} \tag{3.31}$$

Where P_{sig} is the signal power, $P_{XT,in}$ is the intra-channel crosstalk power, both in linear units.

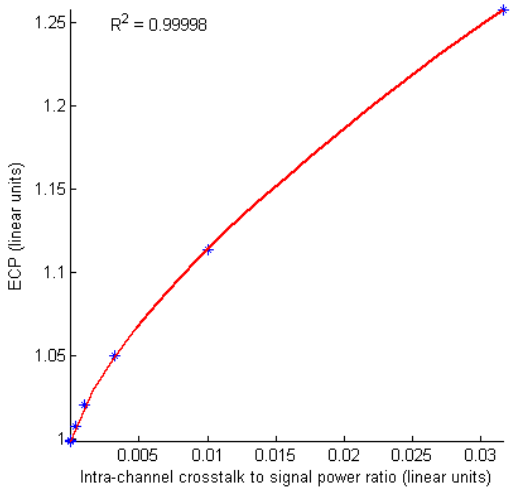

Figure 3.26: Intra-channel crosstalk level vs. ideal ECP

Table 3.11: Intra-channel crosstalk curve fit to ECP

Impairment	Curve Fit Equation	Constants
InXT (linear units)	$ECP_{InXT} = D_1 + D_2 \left(InXT\right)^{D_3}$	$D_1 = 0.997157$ $D_2 = 2.92091$ $D_3 = 0.699507$

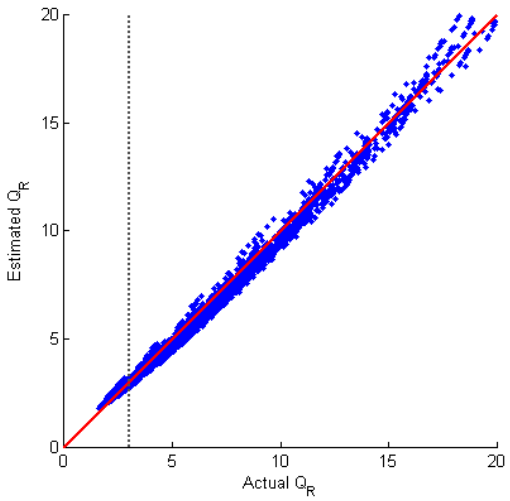

Figure 3.27: Actual Q_R vs. estimated Q_R including intra-channel crosstalk

In Figure 3.26, a curve fit of the InXT parameter and the ideal ECP (shown in red) was empirically determined to follow the power relationship shown in Table 3.11, and the corresponding correlation coefficient was $R^2 = 0.99998$.

Reintroducing the other impairments, an estimate of the total ECP, from all impairments, was determined by combining the estimated ECP value obtained using the InXT curve fit, with the estimated ECP values from the relationships for ASE, PMD and RCD previously established and displayed in Table 3.2, using:

$$ECP_{TOTAL} = ECP_{ASE} \times ECP_{PMD} \times ECP_{RCD} \times ECP_{InXT} \tag{3.32}$$

The estimated Q_R using the total estimated ECP was then calculated using (3.20) and the result was plotted against the actual Q_R computed from the simulation, depicted in Figure 3.27.

Table 3.12: Error statistics between actual Q_R and estimated Q_R, including intra-channel crosstalk

Actual Q_R range	**Mean (Q_R – Est. Q_R)**	**Variance (Q_R – Est. Q_R)**
$Q_R > 8$	0.1616	0.2000
$Q_R \leq 8$	**0.1366**	**0.0544**

The results show good agreement between the Actual Q_R and Estimated Q_R, with the error statistics in relevant Q-factor regions listed in Table 3.12. The error is mostly greater than zero in the most relevant region $Q_R \leq 8$, indicating that the estimated Q_R tends to be a conservative underestimate of the actual Q_R.

3.7.2.2 INTER-CHANNEL CROSSTALK

In a similar manner to the intra-channel crosstalk case, to ascertain the effect of inter-channel crosstalk on the ECP and Q-factor, the results were filtered so that there was zero ASE, PMD and RCD, and the intra-channel crosstalk source was switched off. This left the inter-channel crosstalk level (OutXT), measured as ratio of the total crosstalk power to the signal power, as the remaining variable contributing to the ECP. Mathematically:

$$OutXT = \frac{\sum_{\lambda} P_{XT,\lambda}}{P_{sig}} \tag{3.33}$$

where λ are the wavelengths of the inter-channel crosstalk signals, and $P_{XT,\lambda}$ and P_{sig} are in linear units.

A plot of the ideal ECP against OutXT is shown in Figure 3.28, with the actual points being depicted in blue, and the red line depicting a linear curve fit using the equation and parameters in Table 3.13.

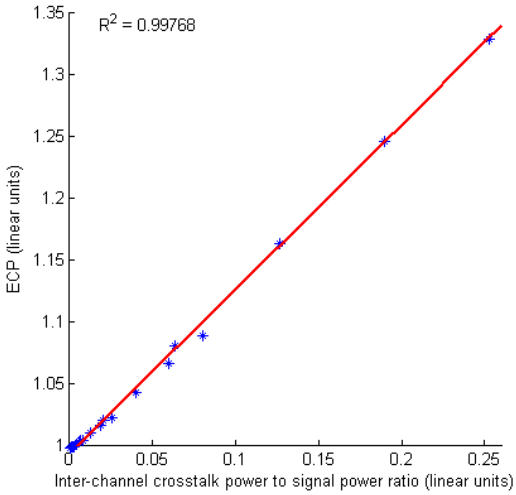

Figure 3.28: ECP as a function of OutXT

Table 3.13: Curve fit equation for estimated ECP from OutXT

Impairment	Curve Fit Equations	Constants
OutXT	$ECP_{OutXT} = E_1(OutXT) + E_2$	$E_1 = 1.33114$ $E_2 = 0.993692$

The estimated ECP from OutXT, ECP_{OutXT}, was then combined with the ECP contributions from ASE, DGD and RCD, calculated using the previously established relationships in Table 3.2, using scalar multiplication to provide a total ECP value. From this, the estimated Q_R was calculated and plotted against the actual Q_R, which is shown in Figure 3.29.

It is apparent that while the estimated Q_R generally fits the actual Q_R, there is a relatively large amount of uncertainty. Additionally, many of the points lie above the ideal red line, indicating that the estimated Q_R overestimates the actual Q_R, particularly near the dotted grey line and suggests that there is a source of ECP that may not have been accounted for. This is undesirable, as paths chosen using the estimated Q_R may actually have Q_R values below the required threshold, resulting in potentially costly false positives with regard to algorithms that are supposed to allocate sustainable quality connections.

The results were re-examined in an attempt to ascertain the reason behind the

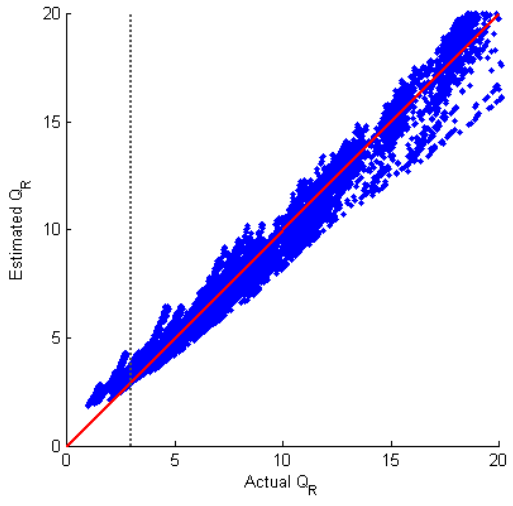

Figure 3.29: Actual Q_R vs. estimated Q_R including inter-channel crosstalk

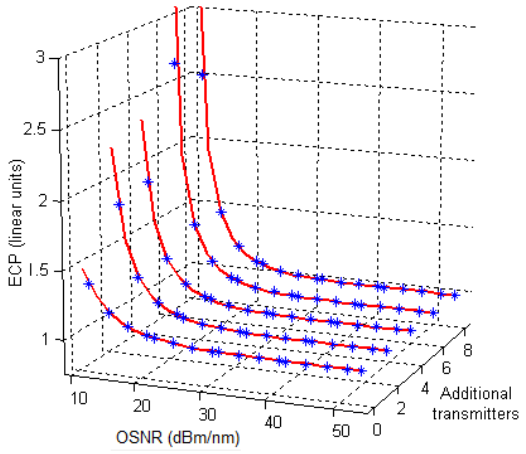

Figure 3.30: ECP as a function of OSNR and NumTx

variability of the Q-factor estimation. It was found from closer inspection that the OSNR to ECP relationship was also dependent on the number of additional transmitters (NumTx) which is directly related to OutXT.

This is apparent in the plot shown in Figure 3.30, where these values are plotted as the blue points. To account for this dependence, separate curve fits were found for the OSNR to ECP, shown as the red lines in Figure 3.30, whilst varying NumTx, in the absence of inter-channel crosstalk, PMD and RCD. Each of these curves closely followed the OSNR to ECP equation from Table 3.2, but with different fitting constants that were dependent on NumTx.

Using these equations to estimate the ECP from the OSNR and NumTx ($ECP_{ASE,NumTx}$), the total ECP was found using:

$$ECP_{TOTAL} = ECP_{ASE,NumTx} \times ECP_{PMD} \times ECP_{RCD} \times ECP_{OutXT} \tag{3.34}$$

The estimated Q_R was then found and plotted against the actual Q_R, with the results displayed in Figure 3.31.

Comparing Figure 3.31 to Figure 3.29 shows that accounting for the variance of the OSNR to ECP relationship due to NumTx vastly improves the quality of the estimated Q_R. In fact, in the critical region along the dotted grey line where the actual Q_R is around 3, the estimate provides almost a perfect fit. Table 3.14 shows the

associated error statistics when inter-channel crosstalk is included in the Q-factor estimation model.

It appears that there is an extra noise source in addition to the inter-channel crosstalk and ASE noise. It is speculated that this is the "ASE-crosstalk beat noise" from the mixing of the ASE passed through the WDM de-multiplexer filter corresponding to the desired signal, and the undesired inter-channel crosstalk optical fields.

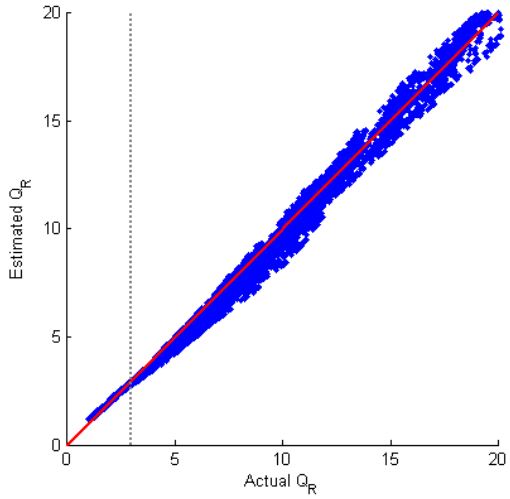

Figure 3.31: Actual Q_R vs. estimated Q_R including inter-channel crosstalk, with OSNR correction

Table 3.14: Error statistics between actual Q_R and estimated Q_R, including inter-channel crosstalk using NumTx dependent OSNR correction

Actual Q_R range	**Mean (Q_R – Est. Q_R)**	**Variance (Q_R – Est. Q_R)**
$Q_R > 8$	0.0794	0.7796
$Q_R \leq 8$	**0.2022**	**0.0742**

The ASE field can be written as a sum of modes over the frequencies ω_j:

$$E_{ASE} = \sum_j A_j e^{i\omega_j t} \tag{3.35}$$

where the index j covers all frequencies across the gain bandwidth of the optical amplifiers in the system and A_j is the ASE field strength in mode j with $P_{ASE,j} = A_j^2$ = ASE power in mode j that reaches the receiver detector.

The optical fields of the inter-channel crosstalk signals can be written as:

$$E_K = B_K e^{i\omega_K t} \tag{3.36}$$

where the index K corresponds to frequencies in the crosstalk channels, and B_K = optical field strength for WDM channel K and $P_K = B_K^2$ = crosstalk channel power.

When these signals are incident upon a detector with responsivity parameter R, the beat noise produces a current $i_{ASE\text{-}XT}$ given by:

$$\begin{aligned} i_{ASE-XT} &= R\left(E_{ASE}\sum_K E_K^* + E_{ASE}^*\sum_K E_K\right) \\ &= R\left(\sum_j A_j e^{i\omega_j t}\sum_j B_k e^{-i\omega_K t} + \sum_j A_j e^{-i\omega_j t}\sum_j B_K e^{i\omega_K t}\right) \\ &= R\left(\sum_j\sum_K A_j B_k e^{i(\omega_j-\omega_K)t} + \sum_j\sum_K A_j B_K e^{-i(\omega_j-\omega_K)t}\right) \\ &= 2R\sum_j\sum_K A_j B_k \cos\left(\left(\omega_j-\omega_K\right)t\right) \end{aligned} \tag{3.37}$$

The electrical filter at the receiver removes the terms where $|\omega_j - \omega_K| > B_e$, where B_e is the electrical filter bandwidth. If A_j is assumed to be constant over the optical filter gain bandwidth, then $i_{ASE\text{-}XT}$ can be written as:

$$i_{ASE-XT} \approx 2R\sqrt{P_{ASE}}\sum_{|\omega_j-\omega_K|<B_e}\sqrt{P_K}\cos\left(\left(\omega_j-\omega_K\right)t\right) \tag{3.38}$$

The limitation on the frequency range given by the summation means that the contributions from each WDM channel are independent and involve beating between the channel power and the ASE within the frequency region around that channel.

Consider Figure 3.32 that shows a typical frequency spectrum including a desired signal, WDM crosstalk signals and the ASE spectrum. Here, P_{ASE} is actually the ASE "out-of-band" power that remains after filtering by the de-multiplexer filter, as

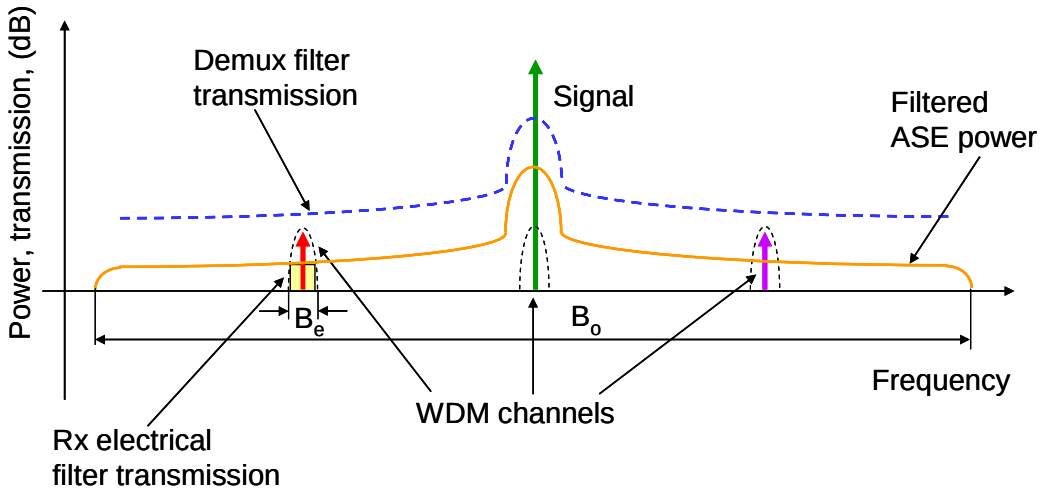

Figure 3.32: Actual Q_R vs. estimated Q_R including inter-channel crosstalk, with OSNR correction

opposed to the "in-band" ASE within the signal channel. B_e is the receiver electrical filter bandwidth and B_o is the gain bandwidth of the optical amplifier.

Treating the current $i_{ASE\text{-}XT}$ as a zero mean Gaussian random process, the ASE-crosstalk beat noise variance, $\sigma_{ASE\text{-}XT}^2$, can be written as:

$$\sigma_{ASE-XT}^{\ 2} = 4R^2 \frac{B_e}{B_o} P_{ASE} \sum_K P_K \tag{3.39}$$

The ASE-crosstalk beat noise standard deviation, $\sigma_{ASE\text{-}XT}$, manifests as noise in the signal by contributing to the ECP. To quantify its effect on the system, the ASE-crosstalk beat noise power was added to the in-band ASE noise power, resulting in a modified OSNR value, $OSNR_{ASE,XT}$, that was dependent on the total amount of inter-channel crosstalk power.

A curve fit was found between the ideal ECP and $OSNR_{ASE,XT}$, at low levels of inter-channel crosstalk to reduce the direct contribution to the ECP from OutXT. This fit was consistent with the ECP to OSNR curve fit in Table 3.2, but resulted in different fitting parameters.

Using the estimated ECP from $OSNR_{ASE,XT}$, termed $ECP_{ASE,XT}$, the total estimated ECP was then calculated using:

$$ECP_{TOTAL} = ECP_{ASE,XT} \times ECP_{PMD} \times ECP_{RCD} \times ECP_{OutXT} \tag{3.40}$$

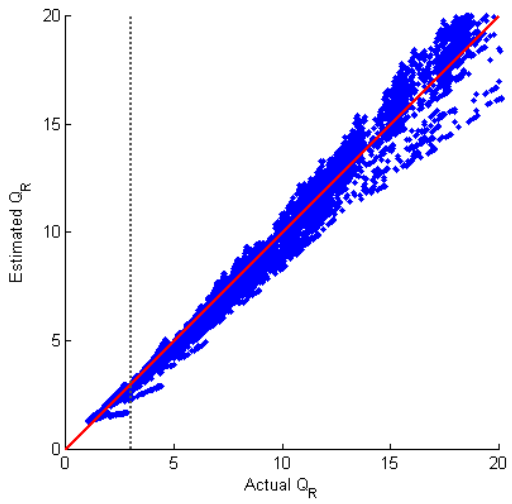

Figure 3.33: Actual Q_R vs. estimated Q_R including inter-channel crosstalk, using $OSNR_{ASE,XT}$

Using ECP_{TOTAL} to compute the estimated Q_R, and plotting against the actual Q_R resulted in Figure 3.33, with error statistics shown in Table 3.15. There is clearly better agreement than in the case where the ASE-crosstalk beat noise is not considered in Figure 3.29.

The results presented indicate that both intra-channel and inter-channel crosstalk can be integrated into the Q-factor estimation model developed for linear impairments in section 3.7.1. It should be noted that in reality, it is unlikely that crosstalk levels for all interfering channels would be identical or easily measured and the simulation results may differ from experimental results. The next section moves on to extend the model further to include non-linear impairments such as FWM, SPM and XPM.

Table 3.15: Error statistics between actual Q_R and estimated Q_R, using $OSNR_{ASE,XT}$

Actual Q_R range	**Mean (Q_R – Est. Q_R)**	**Variance (Q_R – Est. Q_R)**
$Q_R > 8$	0.0430	0.8013
$Q_R \leq 8$	**0.2142**	**0.0971**

3.7.3 NON-LINEAR IMPAIRMENTS

The deployment of all-optical WDM networks poses additional problems for the estimation of Q-factor on a per-channel basis, due to the increased length of network paths and fewer signal regeneration points. This introduces two problems - firstly it becomes necessary to deploy more EDFAs, but these introduce large amounts of ASE noise. To minimise the number of EDFAs one solution is to increase optical launch powers, often up to 3 dBm per channel. As seen in section 2.6.2, large optical power intensities in a small fibre core can lead to non-linear effects that degrade signal quality. The second problem with increasing path lengths is that these non-linear effects can accumulate to significant levels over these longer path lengths [99].

This section considers the effects of the Four Wave Mixing (FWM), Self Phase Modulation (SPM) and Cross Phase Modulation (XPM) on the ECP and Q-factor using the same analysis techniques as in previous sections. Raman scattering and Stimulated Brillouin Scattering (SBS) are not considered as these effects tend to occur at much higher powers, or can easily be mitigated using special techniques, such as dithering and intelligent channel spacing [45], but could be investigated in future work. In fact, the effect of FWM can similarly be mitigated by uneven channel spacing and the presence of chromatic dispersion (that causes signals to “walk away” from each other [45]), but is considered here as many networks may contain low dispersion and evenly spaced channels.

The same simulation setup from Figure 3.25 and set of parameters in Table 3.10 were used, except in these simulations the FWM and SPM/XPM processes were selectively activated to examine the separate and combined effects of the non-linear impairments on the ECP and Q-factor. In these simulations the intra-channel and inter-channel crosstalk were switched off because including these parameters as well as the non-linear effects for multiple channels resulted in unacceptably long simulation times.

3.7.3.1 FOUR WAVE MIXING

The results in this section were obtained from simulations that were conducted with a number of additional transmitters in the system where the FWM process was activated, but the SPM/XPM was not, and inter-channel crosstalk was eliminated using ideal filtering.

It should be reiterated that in these simulations, the high powered signals were propagated down single mode fibre (SMF) with dispersion coefficient of 16 ps/nm·km and dispersion slope of 0.08 ps/nm^2·km, with the variable DCF providing dispersion compensation. There were between 2 to 8 additional channels evenly spaced at 100 GHz above and below the reference channel and signal powers per channel were varied together between 0 and 9 dBm. The bit patterns for additional channels were unrelated to the reference channel.

The techniques previously established in Figure 3.21 were used to determine the ECP contributions of the ASE, DGD and RCD, and the resulting total ECP calculated by taking the product of the three, from which the estimated Q_R was produced. The purpose of this was to observe the overall effect of FWM on the system, with the results shown in Figure 3.34. Compared to the case where there is no FWM in Figure 3.19b, there is an increased spread in the estimated Q_R.

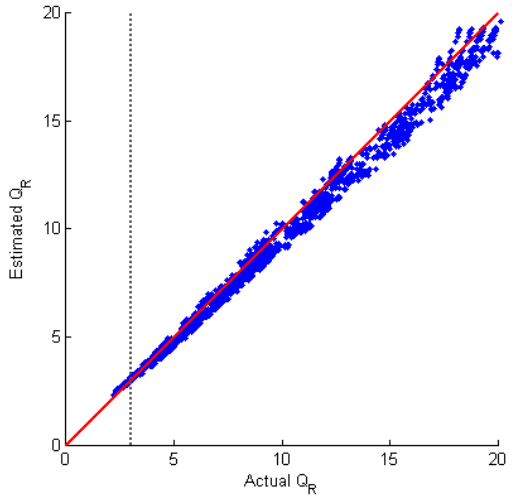

Figure 3.34: Actual Q_R vs. estimated Q_R including FWM in SMF

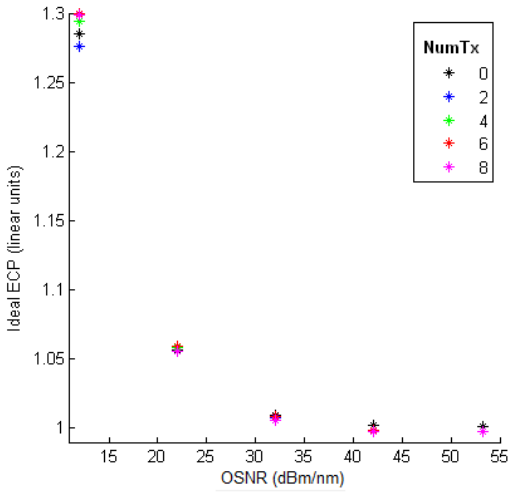

Figure 3.35: ECP contribution from OSNR, varying the number of transmitters

FWM is often treated as an additional random noise variance added to the received mark and space levels (e.g [67]-[69]) that is combined with the ASE noise variance. This is due to the FWM products falling within the filter pass-band and as the number of additional channels (*NumTx*) increases, so do the number of these products. This results in a different OSNR to ECP relationship, dependent on *NumTx*. Further examinations of the OSNR to ideal ECP relationships, shown in Figure 3.35, support this assumption.

To obtain a figure for the ECP contribution due to FWM, ECP_{FWM}, the following derived quantity was used:

$$ECP_{FWM}(OSNR, NumTx) = \frac{ECP_{ideal,OSNR,NumTx}}{ECP_{ideal,OSNR,0}} \tag{3.41}$$

where $ECP_{ideal,OSNR,NumTx}$ is the ideal ECP value for a specific OSNR and number of additional transmitters (NumTx) and the DGD and RCD are zero. Further investigation, not covered here, would be required to relate this heuristically derived quantity to a measureable metric.

Figure 3.36 shows a plot of ECP_{FWM} as a function of the OSNR and the number of additional transmitters. The blue points represent the actual values of ECP_{FWM} while the red lines depict 7th order polynomial curve fits to those points, all with R^2 values greater than 0.99.

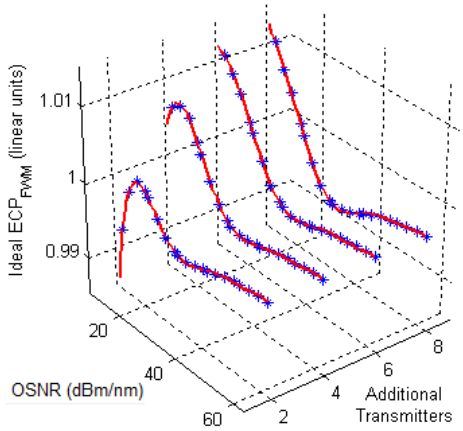

Figure 3.36: ECP contribution from FWM, varying number of additional transmitters and OSNR

It should be noted that these curve fits will vary depending upon the additional channel power profiles and spacings. In these particular simulations, where all channels had equal powers, the relationships were found to be independent of the channel transmit powers.

The estimated total ECP was found using:

$$ECP_{TOTAL} = ECP_{PMD} \times ECP_{RCD} \times ECP_{ASE} \times ECP_{FWM}(OSNR, NumTx) \quad (3.42)$$

and the resultant plot of estimated Q_R vs. actual Q_R is shown in Figure 3.37.

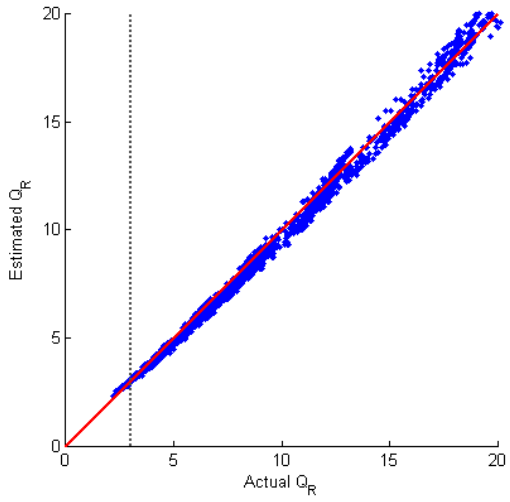

Figure 3.37: Actual Q_R vs. estimated Q_R including FWM with ideal OSNR curve fit

Table 3.16: Error statistics between actual Q_R and estimated Q_R

	Actual Q_R range	**Mean (Q_R – Est. Q_R)**	**Var (Q_R – Est. Q_R)**
Excluding ECP_{FWM}	$Q_R > 8$	0.6035	0.1844
	$Q_R \leq 8$	**0.2639**	**0.0423**
Including ECP_{FWM}	$Q_R > 8$	0.1343	0.1394
	$Q_R \leq 8$	**0.1736**	**0.0289**

Figure 3.37 and Table 3.16 show better agreement between the estimated and actual values of Q_R than in the case where the FWM ECP contribution was not included.

Finally, in a similar manner to section 3.7.1.2.2 for the linear impairments, an attempt was made to determine if there was a simple relationship between the measured ECP and the ideal ECP contributions from FWM. It was found that these relationships were non-linear of at least a 4th order polynomial, shown in Figure 3.38.

It should be remembered that this set of results assumes that all the channel launch powers are the same, and that the additional channels are equally spaced above and below the reference channel by 100 GHz. It is expected that these results would be different if these parameters and configurations were varied, but it is surmised, without further investigation, that the developed methods would still provide a useful tool for Q-factor estimation in the presence of FWM.

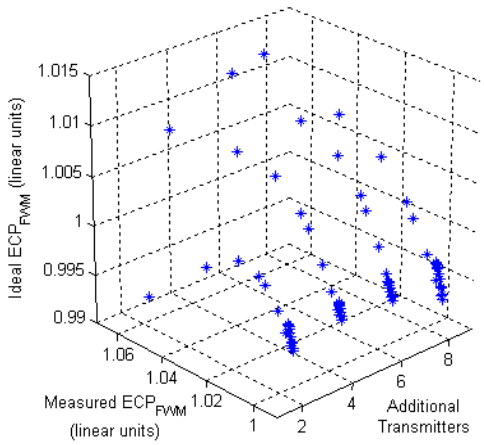

Figure 3.38: Relationship between Measured ECP_{FWM} and Ideal ECP_{FWM}

3.7.3.2 SELF PHASE MODULATION

Simulations were run with the SPM parameter switched on, no additional transmitters, and no crosstalk. An attempt was made to use the previously established relationships from Table 3.2 and method from Figure 3.21 to compute the estimated Q_R, which was then plotted against the actual Q_R to produce Figure 3.39. Clearly, the methods used to estimate Q_R for linear impairments need adjustment when SPM is present.

As discussed in section 2.6.2.3, SPM occurs when the optical intensity of a propagating signal in an optical fibre increases to a level that it induces variations in the local refractive index of the fibre. This change in refractive index interacts with the fibre dispersion, so that the relationship between the RCD and ECP is modified. It was found that the RCD to ideal ECP function does not fit a 2nd order polynomial as a function of both the RCD and the launch power (TxPower) of the optical signal as shown by the blue points in Figure 3.40. The red lines indicate curve fits of the RCD to ECP when the launch power is held constant, and the green lines indicate curve fits of the TxPower to ECP when the RCD is held constant. The correlation coefficient between the ideal ECP and the curve fitted ECP in Figure 3.40 was $R^2 = 0.99921$.

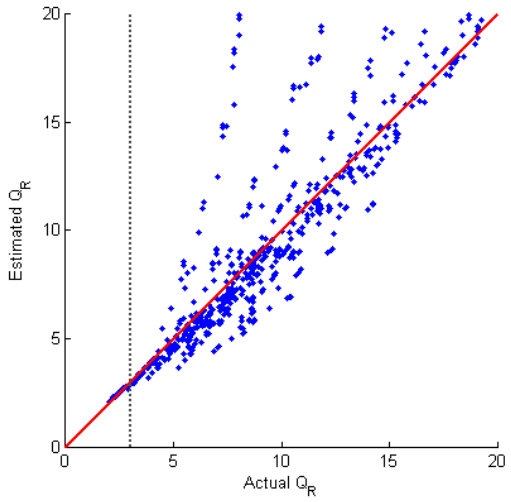

Figure 3.39: Actual Q_R vs. estimated Q_R without SPM correction

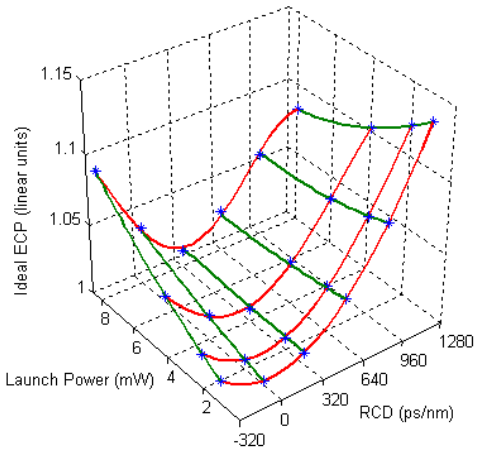

Figure 3.40: Launch power and RCD vs. ideal $ECP_{TxPower,RCD}$

It was found that the TxPower to ideal ECP relationship (green lines in Figure 3.40) could be modelled by a different 2nd order polynomial for each level of RCD, and that the coefficients of the individual 2nd order polynomials, when plotted against the RCD, could all in turn be fitted by 4th order polynomials. It was also found that it did not matter in which order the curves were fitted. If the RCD was fitted to the ideal ECP first, with a constant TxPower, the RCD to ideal ECP relationship (red lines in Figure 3.40) was still a 4th order polynomial, and the corresponding coefficients fitted to the TxPower were still a 2nd order polynomial. This process is summarised in Table 3.17, where the TxPower is measured in mW, and the RCD in ps/nm.

Table 3.17: Curve fit equations for Ideal ECP from SPM, found to be a function of TxPower and RCD

Impairment	**Curve Fit Equations**
SPM, TxPower fitted first	$ECP_{TxPower,RCD} = A_{1,RCD}\left(TxPower\right)^2 + A_{2,RCD}\left(TxPower\right) + A_{3,RCD}$
	$A_{j,RCD} = a_{j,1}\left(RCD\right)^4 + a_{j,2}\left(RCD\right)^3 + a_{j,3}\left(RCD\right)^2 + a_{j,4}\left(RCD\right) + a_{j,5}$
SPM, RCD fitted first	$ECP_{TxPower,RCD} = B_{1,TxPower}\left(RCD\right)^4 + B_{2,TxPower}\left(RCD\right)^3 + B_{3,TxPower}\left(RCD\right)^2 + B_{4,TxPower}\left(RCD\right) + B_{5,TxPower}$
	$B_{k,TxPower} = b_{k,1}\left(TxPower\right)^2 + b_{k,2}\left(TxPower\right) + b_{k,3}$

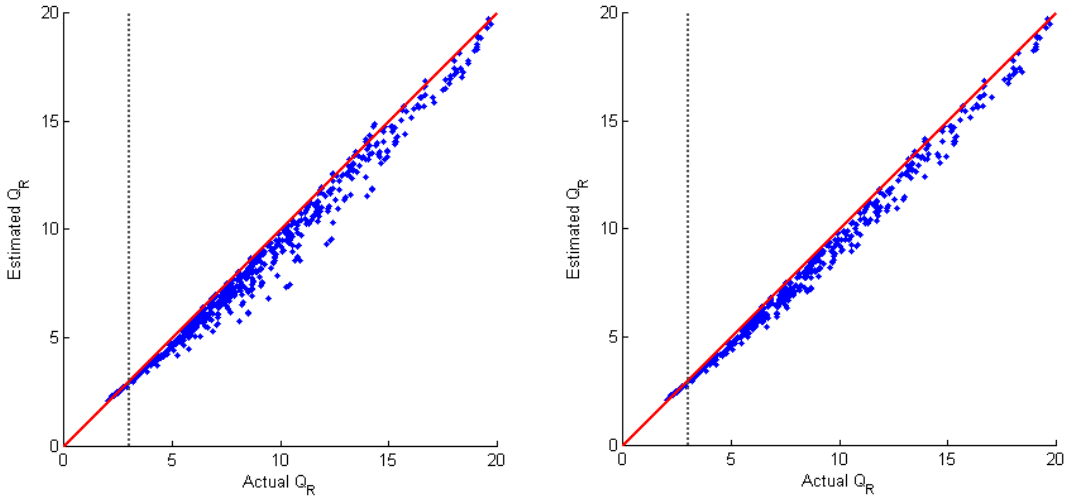

(a) (b)

Figure 3.41: Actual Q_R vs. estimated Q_R including SPM
(a) all launch powers, (b) launch power ≤ 6 dBm

Using this approximation for $ECP_{TxPower,RCD}$, with the previously established relationships for the ideal ECP due to OSNR and DGD, the total ECP was calculated using linear multiplication of the individual ECP contributions, which was then used to calculate the estimated Q_R using (3.20). The estimated Q_R was then plotted against the actual Q_R from the simulation, and is shown in Figure 3.41a, showing reasonable agreement. Further investigation revealed that the points with the most error (which are all underestimates of the actual Q_R) occur at the highest launch power of 9 dBm/channel, or approximately 8 mW (an unlikely value for real networks), and Figure 3.41b shows the same plot with these points removed, leaving points with launch powers of 6 dBm (≈ 4 mW) or below, displaying better agreement. The analysis of the error for the case of launch powers being ≤ 6 dBm is shown in Table 3.18.

Table 3.18: Error statistics between actual Q_R and estimated Q_R, including SPM

Actual Q_R range	**Mean (Q_R – Est. Q_R)**	**Variance (Q_R – Est. Q_R)**
$Q_R > 10$	0.6555	0.1875
$Q_R \leq 10$	**0.3979**	**0.097**

It was found that when the launch power was 9 dBm, the OSNR curve fit began to overestimate the ECP contribution from the ASE, resulting in the estimated Q_R being a larger underestimate of the actual Q_R at some points. This implies that there is an interdependence between the ECP contribution from OSNR and SPM. These results may be in accord with the fact that pulse compression [100] resulting from SPM can increase the signal power, thus reducing the ECP contribution from the OSNR.

3.7.3.2.1 EFFECT OF DISPERSION MAP ON ECP DUE TO SPM

It is known that non-linear effects have the most significant effect at the beginning of a fibre span as the optical intensity at this point is the greatest [46]. For this reason, different link configurations that result in the same RCD at the end of a link may give different ideal ECP values due to SPM.

To investigate this effect, two different dispersion maps, shown in Figure 3.42, were simulated, and the ideal ECP values calculated as before. For the alternate dispersion map, an amplifier with output power of the same level as the launch power was placed after the first span of dispersion compensating fibre (DCF).

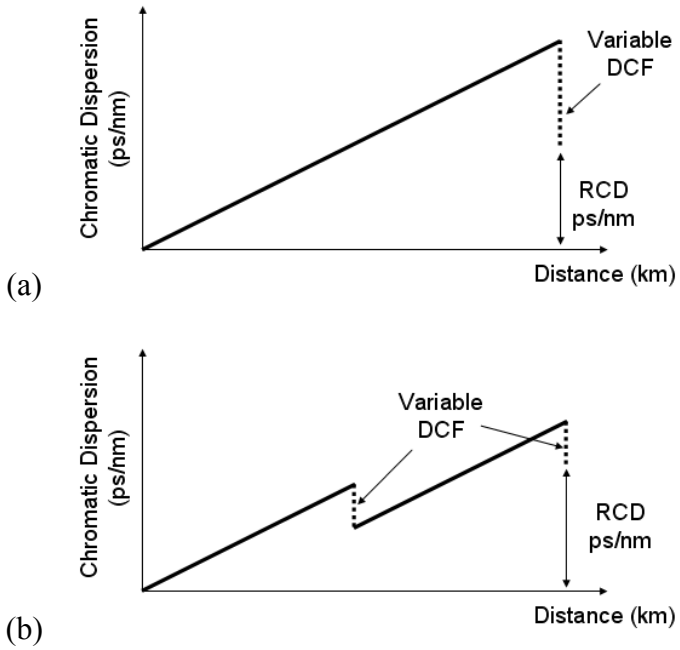

Figure 3.42: (a) Original dispersion map, (b) Alternate dispersion map

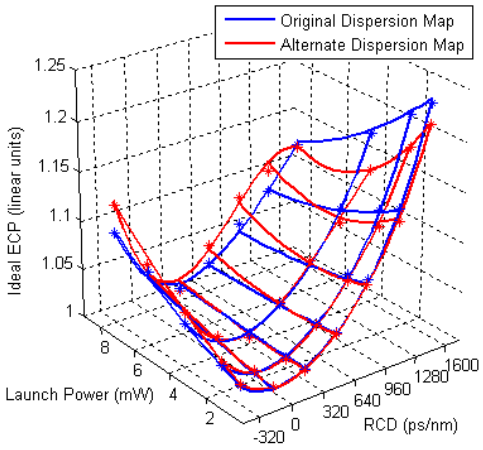

Figure 3.43: Effect of alternate dispersion map on ideal $ECP_{TxPower,RCD}$

Figure 3.43 shows a plot of the ideal ECP value as a function of the TxPower and the RCD for the two dispersion maps. The points represent ideal ECP values, and the lines represent the interpolated estimate of the ideal ECP found using the techniques and relationships established in section 3.7.3.2.

Clearly, different dispersion maps that give the same RCD at the end of a link may not give the same value for ideal ECP in the presence of SPM. In situations where SPM is a significant issue, details of the dispersion map may need to be known in advance and accounted for. It may be possible to calculate and accumulate the ECP due to SPM of each amplified span, but this was not investigated in this work.

3.7.3.3 CROSS PHASE MODULATION

The origin of cross phase modulation is the same as SPM – the Kerr effect, where high optical intensity of an optical signal within in an optical fibre alters its local refractive index. As discussed previously, when the signal itself causes the Kerr effect, the phenomenon is called SPM, however, when other signals are the source of the effect causing phase modulation of the reference signal, the effect is called cross phase modulation (XPM).

To study the effect of XPM on the ECP, the SPM simulation was extended to include additional channels. These channels had the same launch power as the reference channel and individually each would experience SPM, and also cause XPM in the

reference channel. With this in mind, it was reasonable to assume that the effect of XPM might be similar in nature to SPM, but display a dependence on the number of additional transmitters in the system (NumTx). To test this hypothesis, a plot of the ideal ECP due to the RCD and transmitter launch power (TxPower) was made for each value of NumTx, and is shown in Figure 3.44.

In Figure 3.44, that the black lines indicate the cases where there were no additional transmitters in the system and thus the ideal ECP surface is representative of SPM only, acting upon the reference channel. Further examination of the different coloured ideal ECP surfaces reveal that the ideal ECP does indeed depend on not only the RCD and the TxPower, but also the number of additional transmitters. In

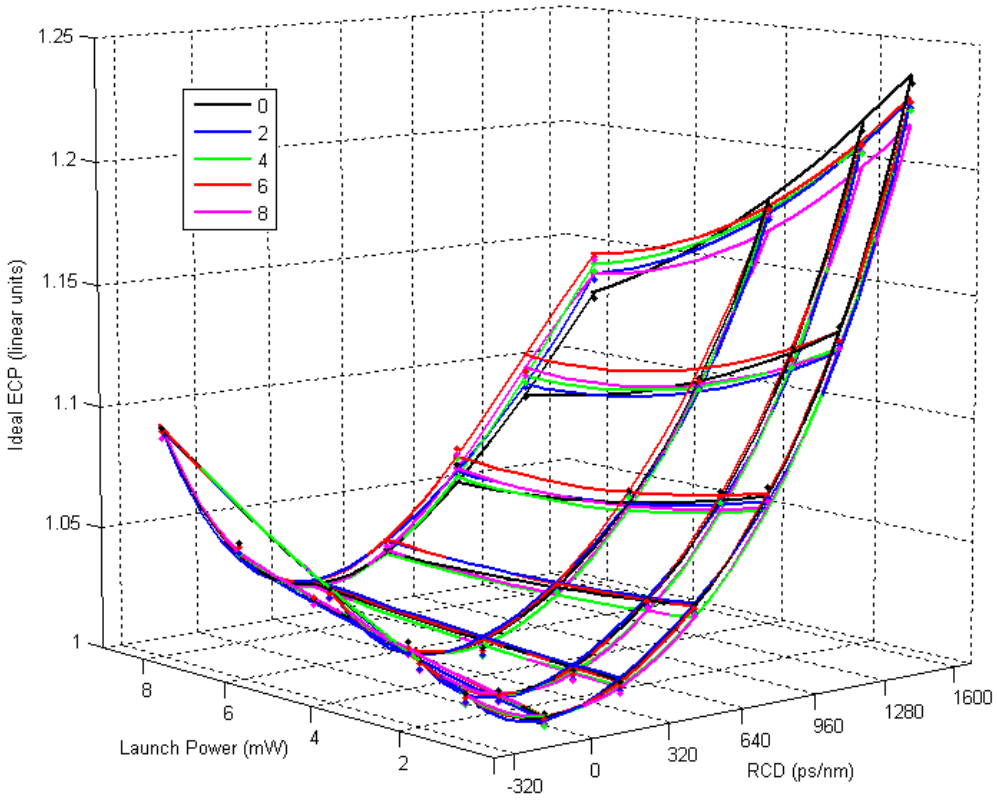

Figure 3.44: ECP from RCD and TxPower, while varying NumTx

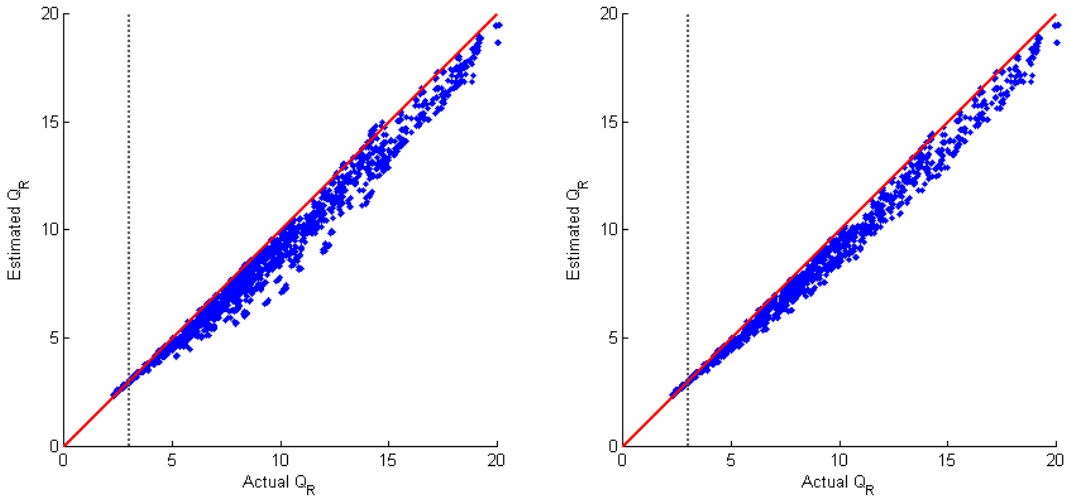

(a) (b)

Figure 3.45: Actual Q_R vs. estimated Q_R including XPM
(a) all launch powers, (b) launch power ≤ 6 dBm

fact, using the same methodology and equations for SPM (recall Table 3.17), it was found to be possible to construct similar curve fitting surfaces for each value of NumTx with different constants. These surfaces represent a signal affected by SPM with variations caused by XPM from additional channels spaced at 100GHz. For a system with many channels, these variations are often modelled as noise, because the data in different channels are independent random processes [100].

Using a different approximation for the ECP due to XPM, dependent on the value of NumTx, the estimated Q_R was calculated and plotted against the actual Q_R in Figure 3.45. Figure 3.45a shows the case where all launch powers were considered, while Figure 3.45b shows the case where the points with 9 dBm launch power were removed. The results are very similar to those for the case of only SPM, which is consistent with theory. Table 3.19 shows the error statistics of the points in Figure

Table 3.19: Error statistics between actual Q_R and estimated Q_R, including XPM

Actual Q_R range	**Mean (Q_R – Est. Q_R)**	**Variance (Q_R – Est. Q_R)**
$Q_R > 10$	0.9316	0.2702
$Q_R \leq 10$	**0.4416**	**0.1395**

3.45b, where the launch powers were ≤ 6 dBm.

When the launch power was 9 dBm the OSNR curve fit equation given in Table 3.2 overestimated the ECP contribution from ASE. This is not surprising, as it appears that the overall effect of SPM/XPM is dominated by the effect of SPM, with minor variations due to the XPM caused by additional transmitters, so the results that apply for SPM should also apply here.

Importantly, the estimated Q_R approaches the actual Q_R when approaching the critical FEC region of actual $Q_R \approx 3$. Despite the error at higher Q-factor values (that matter less when using the estimated Q_R in path selection applications), the results support the methodology developed in this chapter to estimate the Q_R from multiple optical impairments including crosstalk and non-linear effects.

For all the non-linear impairments, it is speculated that it might be possible to find a relationship between the ECP and another common measure of non-linearities – the "non-linear phase shift". This, however, has not been covered in this thesis, in favour of the investigations presented in later sections.

3.7.4 DPSK MODULATION FORMAT

The previous sections have shown that the methods presented to compute the Q-factor from multiple optical impairments including ASE, PMD, RCD, crosstalk, FWM and SPM/XPM can provide a good estimate of the actual Q-factor when using NRZ modulation at bit rates of up to 100 Gbit/sec. Although NRZ modulation is the most widely used format in 10 Gbit/sec systems due to its simplicity [102], advanced modulation formats [103], such as differential phase shift keying (DPSK) [104] are expected to be adopted in higher speed and longer distance optical communication systems. This section examines whether the presented multi-impairment Q-factor estimation technique is applicable to DPSK.

In NRZ modulation, binary information is encoded in the power level of an optical signal, with a mark being represented as a high power level and a space as a low power level. In DPSK, binary information is encoded as a change in the phase of the optical carrier between subsequent bits, with a mark represented by a 0 phase change to the phase of the current signal, and a space represented by a π phase change. A timing diagram for a typical DPSK signal is shown in Figure 3.46.

DPSK has a number of advantages over NRZ modulation, the most significant being a 3 dB lower OSNR requirement for a given BER [104] enabling greater transmission distance. It has also been shown to be more resistant to non-linear effects [105], but is more susceptible to chromatic dispersion [106].

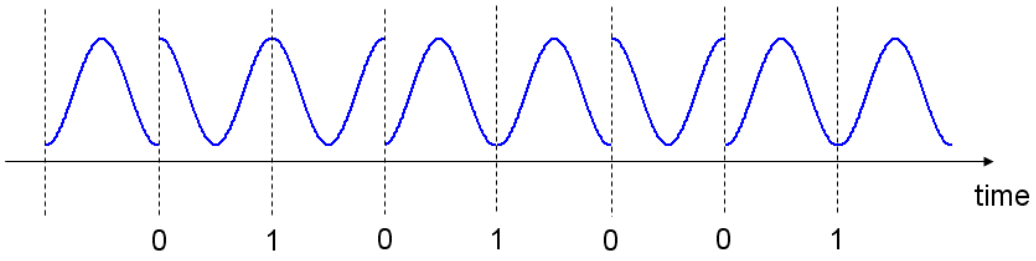

Figure 3.46: DPSK timing diagram

It should be noted that the BER calculated from the Q-factor as defined in (3.5) for NRZ modulation provides an overestimate of the true BER by about 3 dB [107] when used in DPSK, and that for linear operating powers a correction factor is required [108]. While this is inconvenient, there is still value in using the techniques developed in this thesis to estimate the Q-factor from multiple optical impairments.

To examine the combination of the effects of multiple impairments on DPSK signals using the ECP, the simulation setup from Figure 3.7 was used. An NRZ-DPSK transmitter and DPSK receiver consisting of a Mach-Zehnder Interferometer with two PIN photodiodes replaced the NRZ transmitter and receiver photodiodes. For demonstrative purposes, the simulations were conducted at a range of linear launch powers from -9 to 0 dBm with the simulation parameters shown in Table 3.20.

Table 3.20: Linear impairment simulation parameters for DPSK simulations

Parameter	Range of values	Increments
Launch power	-9 dBm to 0 dBm	3 dBm
Loss-Gain	0 to 40 dB	5 dB
DGD	0 to 70 ps	10 ps
RCD	-320 to 1600 ps/nm	160 ps/nm

The Q-factor was calculated using (3.5), and a corresponding ideal ECP was derived using (3.19). This was then plotted against the individual impairment values, for each of the impairments, in the absence of the other two impairments. It was found that the relationships used to find the ideal ECP for the OSNR and the DGD were very similar to those used in NRZ modulation, with the OSNR fitting the function from Table 3.2:

$$\text{Ideal } ECP_{ASE} = \left(A_1 \left(\frac{A_2}{OSNR} \right)^{A_3} \right)^{-1} \tag{3.43}$$

and the DGD fitting a 4th order polynomial:

$$\text{Ideal } ECP_{PMD}(dB) = B_1\left(DGD\right)^4 + B_2\left(DGD\right)^2 \tag{3.44}$$

where ECP_{ASE} and the OSNR are expressed in linear units, ECP_{PMD} is expressed in dB and DGD is expressed in ps.

Interestingly, where previously the ideal ECP due to RCD could be expressed as a function of a quadratic equation, using DPSK this relationship was best fitted by a 6th order polynomial with only even terms:

$$\text{Ideal } ECP_{RCD}(dB) = C_1\left(RCD\right)^6 + C_2\left(RCD\right)^4 + C_3\left(RCD\right)^2 \tag{3.45}$$

where ECP_{RCD} is expressed in dB and the RCD is expressed in ps/nm, a plot of which is shown in Figure 3.47. Here, the constants were $C_1 = 1.83 \times 10^{-19}$, $C_2 = -5.76 \times 10^{-13}$ and $C_3 = 6.88 \times 10^{-7}$. The correlation coefficient R^2 was greater than 0.99 for each of the ECP to impairment relationships.

The total ECP was then found by multiplying the ECP values from the individual impairments, when expressed in linear units, or addition when expressed in dB:

$$ECP_{TOTAL} = ECP_{ASE} \times ECP_{PMD} \times ECP_{RCD} \tag{3.46}$$

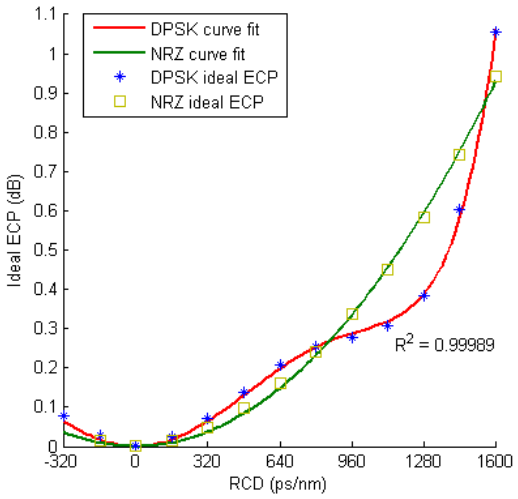

Figure 3.47: Estimated ideal ECP from RCD in DPSK and NRZ.

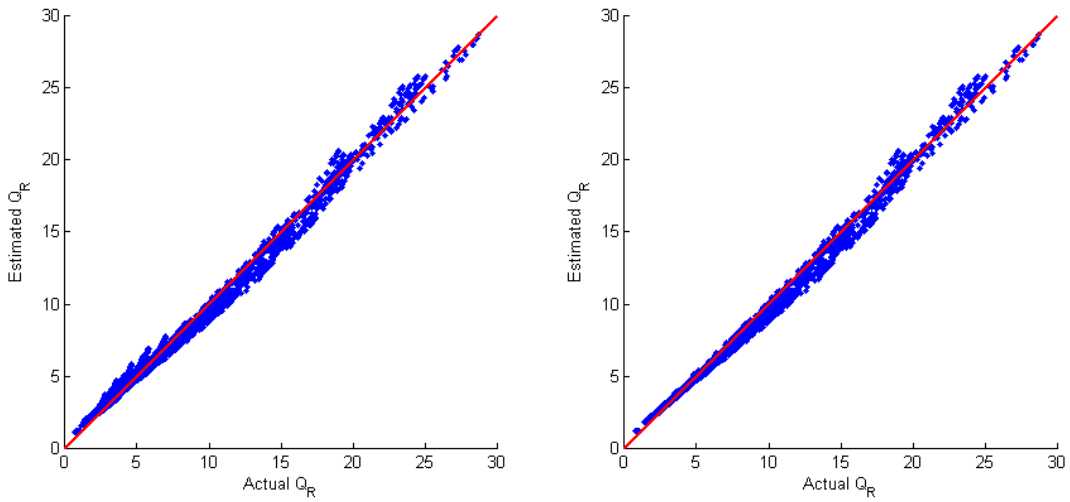

(a) (b)

Figure 3.48: Actual Q_R vs. estimated Q_R using DPSK

Finally, the estimated Q_R was found from ECP_{TOTAL} using (3.20), and the results were plotted against the actual Q_R, shown in Figure 3.48. The plot in Figure 3.48a shows good agreement between the estimated Q_R and actual Q_R, but there is some slight underestimate of the actual Q_R in the region where the Q-factor is between 1 and 7. Further investigation of these points revealed that these were occurring when the RCD values exceeded 960 ps/nm. Filtering of those points yield Figure 3.48b, in which there is better agreement. Table 3.21 gives the error statistics obtained from all points excluding those with RCD > 960 ps/nm.

The results show that the ECP signal degradation metric can be used with DPSK modulation to estimate the Q-factor at the receiver in the presence of linear impairments such as ASE, PMD and RCD. Non-linear impairments were not investigated, due to time constraints, but could be investigated in future work.

Table 3.21: Error statistics between actual Q_R and estimated Q_R using DPSK modulation

Actual Q_R range	**Mean (Q_R – Est. Q_R)**	**Variance (Q_R – Est. Q_R)**
$Q_R > 10$	0.3677	0.4113
$Q_R \leq 10$	**0.1737**	**0.1068**

3.8 SUMMARY, DISCUSSION AND CONCLUSIONS

3.8.1 SUMMARY

In this chapter, a method and framework were presented and validated using computer simulations, that enable the computation of an estimate of the Q-factor and bit error rate (BER) of an optical signal that had been affected by multiple optical impairments, using non return-to-zero (NRZ) and differential phase shift keying (DPSK) modulation. For NRZ modulation these include linear impairments such as amplified spontaneous emission (ASE), polarisation mode dispersion (PMD) and residual chromatic dispersion (RCD), as well as intra-channel and inter channel crosstalk and non-linear impairments such as four-wave mixing (FWM), self phase modulation (SPM) and cross phase modulation (XPM). For DPSK modulation the work in this thesis only covered linear impairments.

One approach was to calculate the eye closure penalty (ECP) directly from the received mark and space statistics in the presence of individual, and combinations of, the linear optical impairments – ASE, PMD and RCD. The ECP was then curve fitted to individual impairments. The total ECP was calculated as the product of the individual ECPs under the assumption that the ECP contribution from each of the individual impairments was independent of the other impairments. This assumption was shown to be very reasonable. The ECP calculation included a parameter β and its effect was studied, with the conclusion that the best value for β is 1.

A relationship was derived between the Q-factor at the receiver and ECP, and used to estimate the Q-factor at the receiver. This approach gave and approximate value for the Q factor.

Working backwards from the actual receiver Q-factor gave an associated "ideal" ECP value which revealed that the ECP calculated directly from the receiver statistics was an overestimation of the ideal ECP. Further investigation showed that for each of the individual impairments, there was a linear transformation between the two. Furthermore, it was found that it was possible to skip this transformation altogether and instead fit the ideal ECP to the individual impairments.

This revelation meant that in real world terms, to implement the presented Q-factor estimation method, it is only necessary to measure the Q-factor from individual impairments in the optical communication system for the bit rate and modulation format (NRZ, the most widely used modulation format and DPSK, its most likely successor) of interest. This is then used to determine the curve fitting constants that relate the ECP to the individual impairments, a process summarised and reiterated in Figure 3.49, where the blue shaded boxes indicate quantities that need to be found in a calibration phase, and the yellow shaded boxes indicating quantities calculated a-priori to connection provisioning.

Testing the framework on 40 Gbit/sec and 100 Gbit/sec NRZ modulated systems showed that it was still applicable to determining the Q-factor at these rates. It was found that at these higher bit rates the ECP to DGD relationship was more accurately modelled by a 6th order polynomial and the RCD was now best modelled by a 4th order polynomial.

This method was then extended to include the effects of intra-channel and inter-channel crosstalk, where it was found that with knowledge of the crosstalk power level and number of interfering transmitters, it was possible to calculate an associated ECP. In the case of intra-channel crosstalk, this ECP was a simple function of the

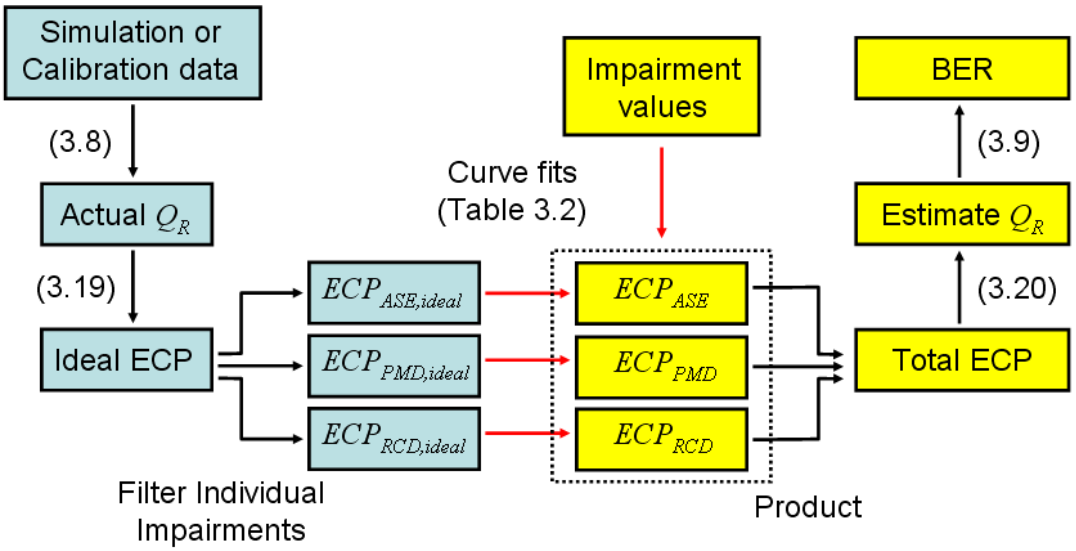

Figure 3.49: Process to estimate Q_R using the ECP.

crosstalk power, but in the case of inter-channel crosstalk, the ECP contribution was more complex, being not only a function of the crosstalk power and number of transmitters, but also dependent on an ASE-Crosstalk beat noise term.

Next, the four wave mixing, self phase modulation and cross phase modulation non-linear impairments were considered, by increasing the launch powers up to 9 dBm, well into the non-linear operating region. It was found that ECP contribution from the additional noise caused by the FWM process was dependent on the OSNR and number of transmitters. This was expected, as the extra signals generated by the FWM phenomenon are analogous to inter-channel crosstalk.

The self phase modulation effect on the ECP manifested as a dependence on both the RCD and the launch power, and a two-dimensional curve fit for both parameters were found. Even though this was found to be possible, the overall estimated Q-factor computed was found to provide a significant overestimate when the launch power was greater than 6 dBm per channel, but showed good agreement otherwise. The reason for this is unclear, but it is suspected that the SPM effect causing pulse compression and actually improving signal power might be exacerbated at higher launch powers, but was unaccounted for in the OSNR to ECP calculation. The results for cross phase modulation were very similar to those of SPM, but was shown to add a dependence on the number of transmitters.

Finally, the multi-impairment Q-factor estimation method was tested on the DPSK modulation format. While the applicability of the conventionally defined Q-factor is debateable in phase shift keyed modulation, there is evidence in the literature to suggest that it is still useful [108]. With slight post calculation modification, in the linear operating regime (and given that DPSK has been shown to be more robust than NRZ modulation against non-linear effects) it would appear that the presented Q-factor estimation method is still useful. Applying the developed method directly to the data obtained from DPSK simulations showed that the estimated Q-factor showed good agreement with the actual Q-factor, after accounting for a change in the ECP to RCD curve fit (that was now found to follow a 6^{th} order polynomial), with the best accuracy obtained when the RCD was less than 1000 ps/nm.

3.8.2 DISCUSSION

The results and analysis presented in this chapter show that it is possible to calculate the Q-factor at the receiver in an optical link, using the ECP due to multiple optical impairments. The most obvious application of this result is in the automated provisioning of connections in all-optical networks where it was shown in section 2.5 that routing using multiple constraints was generally infeasible. Therefore calculating a single signal quality metric is extremely useful. While there are a number of references in the literature, covered in section 2.7, that have provided estimates of the Q-factor (and hence BER) from multiple impairments, the author is unaware of any that can include the range of degradations and modulation formats discussed in this work with a quantitative evaluation of accuracy. In this work, it has become clear that there are two factors that affect the accuracy of the Q-factor estimation from multiple impairments using the method proposed in this work.

The first factor is the accuracy of the curve fits between the individual impairments and the ideal ECP that allow real-time calculation of the estimated Q-factor. For different bit rates and modulation formats, and in some cases, the number of transmitters and launch powers, each of the optical impairments will have a slightly different relationship to the ECP. This means that the curve fitting constants will need to be determined accordingly, either through simulation of the system, or through calibration data from the real system. Inaccuracies in these relationships can lead to error in the estimation of the overall Q-factor when combining the ECP values from multiple impairments. In the event that a relationship can not be found between the ideal ECP and an optical impairment, it should be sufficient to interpolate values from the calibration data.

The second factor affecting the accuracy of the Q-factor estimation is the fact that the effects of some impairments are not independent of each other. This was shown in results presented for SPM and XPM, where it was found that the combination of the individual impairment ECP values via multiplication (valid when the impairments are independent) did not provide accurate results under certain conditions. This problem can be mitigated by calculating the ECP from a joint set of multiple parameters (e.g. RCD and launch power), as shown in the SPM/XPM case.

From a networking perspective, it should be noted that this method for combining multiple impairments into a single metric does not result in a metric that satisfies the optimal substructure property discussed in section 2.5.4. This is because the overall metric includes the effect of RCD, which in optical networks can be a negative or positive value. Note that this is the case for any combined signal quality metric that would include the effect of RCD and means that conventional shortest path algorithms (e.g. Dijkstra's and Bellman-Ford) can not claim to converge to a globally optimal solution using metrics of this kind. This does not mean that the metrics are not useful, as evidenced by the large number of routing algorithms that utilise such metrics (previously discussed in section 2.7). However, it means that there may be a number of routes that might have adequate signal quality which are not found by those routing algorithms. This issue is not a topic of this thesis.

Future work could be done to include the effects of more optical impairments into the ECP combination framework, as well as validation of the presented technique using experimental data. Further investigation could also be done to refining the ECP relationships for non-linear effects and to ascertain the dependencies between the system parameters. It would be interesting to determine if using the ECP to combine the effect of multiple impairments is useful for other modulation formats besides NRZ and DPSK.

3.8.3 CONCLUSIONS

From the data collected and the results presented in this chapter, a number of important conclusions can be made and are listed below.

- It is possible to combine the signal degradation effect from of multiple optical impairments on an optical signal, using the presented framework that utilises the ECP metric.
- It is not a necessary to calculate the ECP from receiver statistics, as this overestimates the ideal ECP. Instead it is better to calculate the ideal ECP value from the measured receiver Q-factor to gauge the effect of optical impairments on signal quality (a measurement procedure which can be applied in a real network was described above).
- The ECP can be related to not only linear impairments such as ASE, PMD and RCD, but also to crosstalk and non-linear impairments such as FWM, SPM and XPM.
- The Q-factor of an optical signal can be accurately predicted in NRZ and DPSK modulated systems from the combined ECP, at bit rates of up to 100 Gbit/sec. This shows that the developed method will be applicable in future ultra-high capacity optical networks.
- The estimated Q-factor is very often a worst case underestimate of the actual Q-factor, which is often a desirable property for network provisioning.

To this point, the values for optical impairments have been considered only as static values while in reality, some of these values may be dynamic. In the next chapter, the techniques developed in this chapter will be applied to the case where some of these impairments are time-varying.

4

Outage Probability

4.1 INTRODUCTION

The work presented in chapter 3 provides a solid framework and methodology that enables a network operator to estimate the Q-factor and BER for optical connections with multiple optical impairments. To this point, the values for these impairments have been static values. In reality they may vary with time, so that a connection that was provisioned subject to one set of impairment values might be unsustainable at a later time as the impairment values change, possibly resulting in a "connection outage".

This chapter begins by explaining the relevance of the outage probabability as an enabling mechanism in modern day telecommunications. It then examines the previous published research on outage probability subject to single impairments. This work is distinct from the concept of engineering network "protection", but the outage probability of a network path can certainly be used to aid in the design of protection paths. It is then shown that the method used to estimate signal quality constructed in chapter 3 can be extended to enable the estimation of the outage probability for a connection affected by multiple time-varying optical impairments.

4.2 OUTAGE PROBABILITY

In an increasingly competitive telecommunications marketplace, service level agreements (SLA) are a competitive differentiator that can attract customers willing to pay for certainty of service. It is important that network operators are able to make realistic guarantees, to be able to deliver on their promises. In telecommunications, the amount of down time that a provisioned service or connection is reasonably expected to experience is a key metric. This down time must be evaluated and is related to the "outage probability". For example, a network operator may specify that a service or connection will experience "99.99% uptime", equating to 52.6 minutes of downtime per year, or an outage probability of 0.01%. Serious network outages can be caused by events such as physical cable cuts or environmental disasters. In the context of optical networks and this work, an outage is considered to have occurred if the bit error rate (BER) of a connection exceeds 10^{-9} or 10^{-12}. As seen in chapter 3, the BER is determined by the level of optical impairments, such as ASE, PMD and RCD, impacting on the optical signal.

In optical networking, most of the literature pertaining to outage probability relates to PMD [109]-[112]. The actual value of the differential group delay (DGD) caused by PMD is a time varying quantity best modelled by a Maxwellian distribution [113]. In this context, the outage probability is usually defined in terms of the probability that the DGD exceeds a certain threshold level [46], resulting in an unacceptably high BER. The work in [109] directly relates the probability density function of first and second order PMD to the BER, and calculates the outage probability by taking the cumulative probability of the BER exceeding 10^{-12}.

The authors of [114] consider the effect of time dependent seasonal variations in temperature on the chromatic dispersion in optical fibre across different regions of the USA. The temperature and corresponding dispersion variations are modelled by a sinusoidal function that cause levels of residual chromatic dispersion (RCD) to exceed a specified level of dispersion compensation. These excursions can cause an unacceptably high power penalty. In this context, the outage probability is defined as

the probability that the dispersion penalty exceeds 1 dB, and was found to be approximately 5.5×10^{-5}.

The effect of polarisation dependent loss (PDL) on signal OSNR was considered in [115], who showed that PDL could cause fluctuations in the OSNR as signal power varied with polarisation state changes. Here, the outage probability was defined as the probability that the BER exceeded 10^{-5}, with the author citing this threshold as the maximum BER that forward error correction (FEC) mechanisms could typically correct. In [116], power penalties arising from ASE transients and nonlinearities are shown to exist in EDFAs operating in WDM networks when channels are added or removed from optical links. These penalties, existing for microseconds to milliseconds, could significantly disrupt system performance resulting in network outages to multiple channels, and are exacerbated in higher bit rate systems with higher launch powers. This work did not specifically calculate an outage probability associated with these events.

Ultimately, a network operator would like to be able to know the outage probability of new and existing connections as the state of the network changes, but to do so requires accurate data on traffic demands and optical impairments. Fortunately, the deployment of real-time optical performance monitors that can monitor single [117], or multiple impairments are becoming more common [96]. These monitors can record large amounts of operational data, including histograms of impairment values over time.

4.3 DYNAMIC OPTICAL IMPAIRMENTS

The framework developed in chapter 3 allowed the combination of the effects of multiple optical impairments including ASE, PMD, RCD, crosstalk, FWM and SPM/XPM, on the Q-factor and BER of an optical connection. This was achieved by using an intermediate quantity, the ECP, which had clear relationships with those impairments and also with the Q-factor.

Previously, the values of the optical impairments were considered to be static, but in reality some of these values are dynamic. The instantaneous DGD value caused by PMD is often modelled by a Maxwellian random variable [46]. It has been shown that the RCD can have sinusoidal seasonal variations associated with temperature [114], and that PDL [110] in network components and optical fibre. ASE power may spike during channel addition and deletion [116] causing OSNR variations. A common method to model time varying quantities such as these is to treat them as random variables (RV).

As previously mentioned, optical performance monitors are expected to be able to record data on optical impairment levels within an optical network and in particular to build up histograms of impairment values over time windows that could be of the order of months. These histograms can easily be normalised to create discrete probability density functions, also called probability mass functions (PMFs),

4.3.1 PMD PROBABILITY MASS FUNCTION

The instantaneous DGD due to the PMD impairment has been shown to follow a Maxwellian [46] distribution with respect to the instantaneous DGD, Δτ:

$$p(\Delta\tau) = \frac{\sqrt{2}}{\alpha^3\sqrt{\pi}}\Delta\tau^2 \exp\left(\frac{-\Delta\tau^2}{2\alpha^2}\right) \tag{4.1}$$

the shape of which is characterised by the mean DGD, DGD_{ave} or $\overline{\Delta\tau}$:

$$\overline{\Delta\tau} = 2\alpha\sqrt{\frac{\pi}{2}} \tag{4.2}$$

Substituting (4.2) into (4.1) gives:

$$p(\Delta\tau) = \frac{32}{\pi^2}\frac{\Delta\tau^2}{\overline{\Delta\tau}^3}\exp\left(\frac{-4}{\pi}\frac{\Delta\tau^2}{\overline{\Delta\tau}^2}\right) \tag{4.3}$$

Figure 4.1 shows an example of a PMF for the instantaneous DGD where the mean DGD is 20 ps.

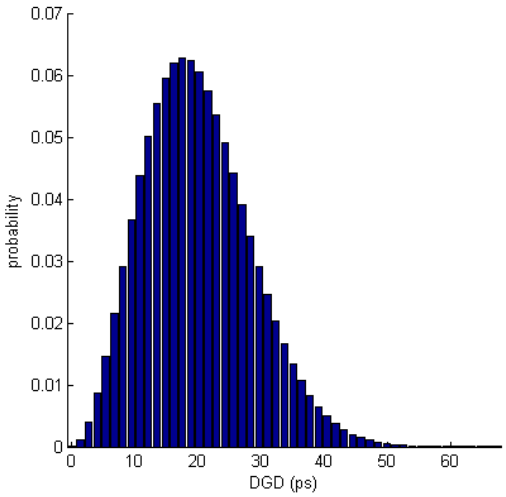

Figure 4.1: PMF of DGD from PMD, DGD_{ave} = 20 ps

4.3.2 RCD PROBABILITY MASS FUNCTION

The chromatic dispersion of a span of fibre is dependent on the temperature of the fibre. The authors of [118] found that optical fibres are typically buried at depths of about a metre, so daily temperature variations are negligible, but seasonal soil temperature variations are significant. The work in [114] showed that the soil temperature in regions across the terrestrial United States could be modelled by a sinusoidal function over the period of a year, with a peak to peak change in temperature, ΔT, of up to 20°C about the mean temperature.

For single mode fibre, the zero dispersion wavelength λ_0 and the dispersion slope S_0 are related to the temperature T by [114]:

$$\frac{d\lambda_0}{dT} = 0.02452 \; nm/°C \tag{4.4}$$

$$\frac{dS_0}{dT} = -1.55825 \times 10^{-6} \; ps/nm^2/km/°C \tag{4.5}$$

So for ΔT = 20°C, the corresponding range of $\Delta\lambda_0$ around a mean value of λ_0 = 1322 nm would be [1321.7548, 1322.2452] nm, and ΔS_0 around a mean value of S_0 = 0.092 ps/(nm^{2}km) would be [0.092015583, 0.091984418] ps/(nm^{2}km).

A connection with a channel wavelength of 1550 nm would therefore experience chromatic dispersion in the range of [16.802, 16.768] ps/(nm·km). Assuming longer path lengths, for example 500km due to all-optical networking, and the use of static dispersion compensation, the RCD would be found to vary with a sinusoidal function around the mean RCD value, RCD_{ave} by approximately ± ΔRCD = 8.4 ps/nm. Note that longer path lengths would increase this value, and also that higher bit rate signals are much more adversely affected by even small variations in RCD.

The time varying RCD can thus be approximately modelled by a sinusoidal function:

$$RCD(t) = RCD_{ave} + \Delta RCD \cdot \sin(t) \tag{4.6}$$

The corresponding probability density function can be found using [119]:

$$p(RCD) = \begin{cases} \left(\pi\sqrt{2\sigma^2 - \left(RCD - RCD_{ave}\right)^2}\right)^{-1}, & \left|RCD - RCD_{ave}\right| < \Delta RCD \\ 0, & \left|RCD - RCD_{ave}\right| \geq \Delta RCD \end{cases} \quad (4.7)$$

Where the standard deviation of a sinusoidal function is

$$\sigma = \frac{\Delta RCD}{\sqrt{2}} \quad (4.8)$$

Figure 4.2 shows a PMF of the RCD where RCD_{ave} = 100 ps/nm and ΔRCD = 8 ps/nm. Note that the most likely RCD values are the values that are $RCD_{ave} \pm \Delta RCD$, while the least likely RCD value is RCD_{ave}. This is because the gradient of the time varying RCD function given by (4.6) approaches zero near the peak values, and thus the instantaneous RCD values spend more time near those values, resulting in a higher probability in the PMF. Consequently, at RCD_{ave} the magnitude of the gradient is at a maximum, and thus the RCD spends the least amount of time at that value.

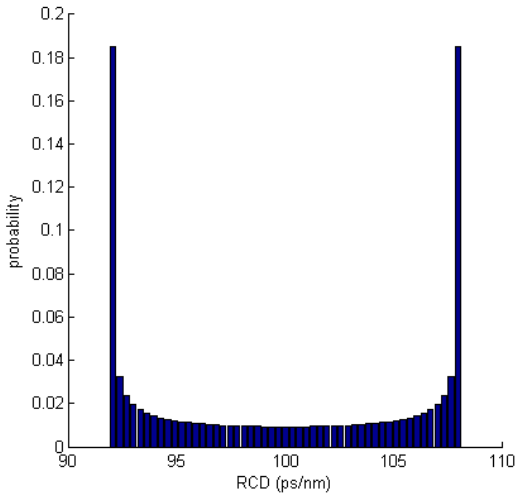

Figure 4.2: PMF of RCD, with RCD_{ave}= 100 ps/nm and ΔRCD = 8 ps/nm

4.3.3 OSNR PROBABILITY MASS FUNCTION

The main source of time dependent OSNR variations in the literature refers to polarisation dependent loss (PDL) of signal power in components and optical fibre [115]and ASE transients in EDFAs [116], [120].

PDL is caused by optical components and fibre that cause different amounts of signal attenuation for signal components aligned with the two orthogonal polarisation axes, ultimately resulting in an OSNR penalty. The PDL is dependent on random alignment between the state of polarisation of the optical signal and the axes of the PDL in the elements along the path and is a time dependent following a Maxwellian distribution [121]. The OSNR penalty is shown to be roughly proportional to the PDL power penalty at the receiver [115].

As seen in [116] and [120], ASE variation within EDFAs can depend on the number of channels being dropped or added at any particular time. For a 16 channel system, the OSNR can temporarily drop for hundreds of microseconds by up to 2 dB when 15 channels are dropped or added in close temporal proximity. This effect increases with the number of channels in the system. Aside from catastrophic network events such as cable cuts and mass calling events, it is unlikely that this effect will be seen too often in normal network operation.

In light of these facts, Figure 4.3 shows a possible PMF of OSNR for a particular connection. In this case, the steady state value of OSNR, $OSNR_{SS}$ is 25.5 dBm/nm, and the PDL penalty, PDL_{pen} is characterised by a Maxwellian distribution with a mean value PDL_{ave} of 0.5 dB. It is assumed, for simplicity, that the OSNR penalty is equal to the PDL power penalty. The distribution of the OSNR is then characterised by $OSNR = OSNR_{SS} - PDL_{pen}$ and $OSNR_{ave} = 25$ dBm/nm.

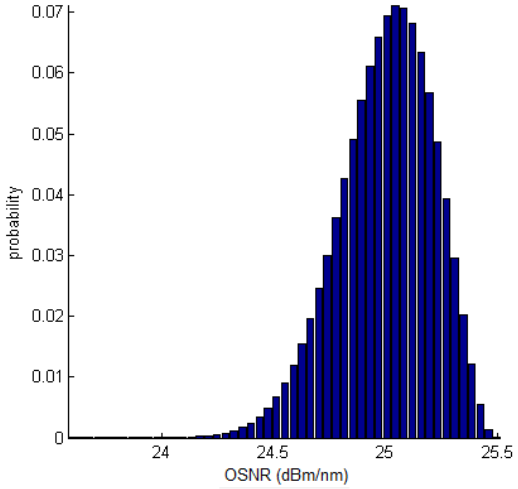

Figure 4.3: PMF of OSNR, with $OSNR_{ave}$ = 25 dBm/nm

4.4 OUTAGE PROBABILITY FROM MULTIPLE IMPAIRMENTS

Using the framework developed in Chapter 3, it is possible to transform these impairments to ECP values. These transformations depend on bit-rate and modulation format. For simplicity, NRZ modulation with bit-rates of 10 Gbit/sec, 40 Gbit/sec and 100 Gbit/sec are considered, in the presence of ASE, PMD and RCD. As seen in section 3.7.3 and 3.7.2, non-linear impairments and crosstalk can be taken into accounted by using ECP relationships for OSNR and RCD that are dependent on the transmit power and number of interfering channels in the path.

4.4.1 TRANSFORMATION OF IMPAIRMENT PMFS TO ECP PMFS

Given the individual impairment PMFs, such as those in Figure 4.1, Figure 4.2 and Figure 4.3, it is possible to compute the corresponding PMF of the ECP contribution for each of the impairments. This is done using the method described in [122], given by the following extract (with random variables denoted in **bold**):

> Assume that the random variable (RV) **x** is of discrete type taking the values x_k with probability p_k. In this case, the RV **y** = g(**x**) is also of discrete type taking the values $y_k = g(x_k)$.
>
> If $y_k = g(x)$ for only one $x = x_k$, then
>
> $$\mathrm{P}\{\mathbf{y} = y_k\} = \mathrm{P}\{\mathbf{x} = x_k\} = p_k$$
>
> If, however, $y_k = g(x)$ for $x = x_k$ and $x = x_m$, then
>
> $$\mathrm{P}\{\mathbf{y} = y_k\} = \mathrm{P}\{\mathbf{x} = x_k\} + \mathrm{P}\{\mathbf{x} = x_m\} = p_k + p_m$$

This means that given the PMF of an optical impairment, DGD for example, the PMF for the ECP due to DGD, ECP_{DGD} would be found by transforming each DGD value in the PMF to an ECP_{DGD} value using the relationship in Table 3.2 (a 4th order polynomial) and leaving the corresponding probabilities unchanged. Figure 4.4 shows the transformation of the DGD PMF from Figure 4.1 using the transformation function:

$$ECP_{DGD}(dB) = A_1(DGD)^4 + A_2(DGD)^2 \tag{4.9}$$

Where $A_1 = 3.21412 \times 10^{-8}$ and $A_2 = 1.08922 \times 10^{-4}$, and DGD is in ps.

Similarly, the PMFs for the ECP due to OSNR and the ECP due to RCD can be computed using:

$$ECP_{OSNR}(dB) = 10\log_{10}\left[\left(1 - B_1(B_2 / OSNR)^{B_3}\right)^{-1}\right] \tag{4.10}$$

$$ECP_{RCD}(dB) = C_1(RCD)^2 \tag{4.11}$$

Where $B_1 = 2.70027$, $B_2 = 0.497971$, $B_3 = 0.695772$, $C_1 = 3.63704 \times 10^{-7}$, $OSNR$ is in linear units and RCD is in ps/nm. Note that these constants and relationships apply only for a 10 Gbit/sec NRZ system with linear launch powers. For 40 Gbit/sec and 100 Gbit/sec systems, the ECP_{DGD} and ECP_{RCD} relationships vary slightly, fitting 6th

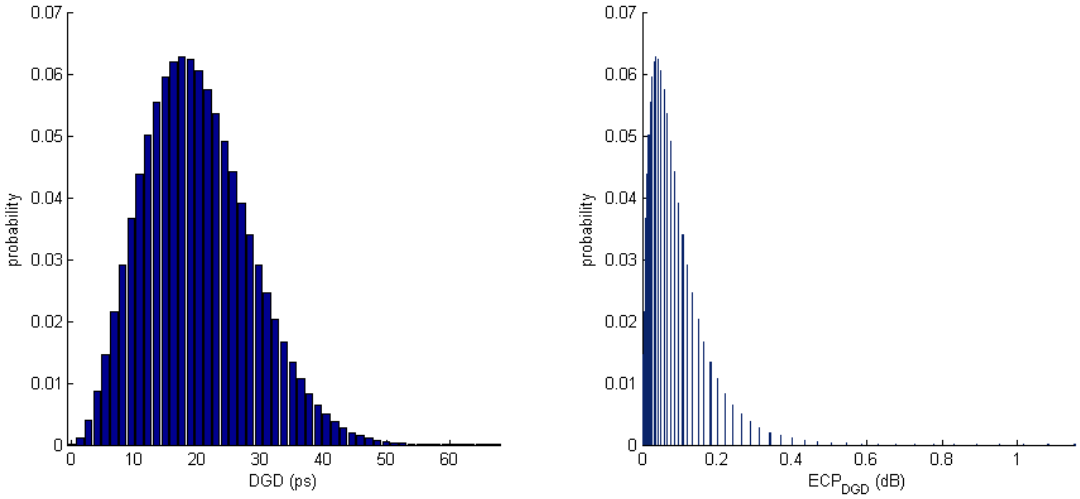

(a) (b)

Figure 4.4: Transformation of (a) DGD PMF to (b) ECP_{DGD} PMF.

and 4th order polynomials respectively.

When increasing launch powers above the linear operating region (> 3 dBm), the effect of SPM/XPM can be found as a function of the ECP for RCD dependent on launch power, as shown in sections 3.7.3.2 and 3.7.3.3, while the effect of FWM manifests as a function of the ECP for OSNR, dependent on the number of additional transmitters as shown in section 3.7.3.1. Similar techniques can be used to account for crosstalk.

4.4.2 COMBINING ECP PMFS

After computing the ECP PMFs, the next step in the process is to combine these PMFs into a single PMF of the total ECP caused by the optical impairments. For static values of ECP, this was done by multiplying the individual ECP values together or equivalent to adding the ECP values expressed in dB as shown in section 3.7.1, equation (3.30). Recall basic probability theory:

> Consider the discrete random variable **x**, defined by $P\{\mathbf{x} = x_k\} = p_k$ and the discrete random variable **y**, defined by $P\{\mathbf{y} = y_m\} = q_m$. The probability of any particular pair of values $\mathbf{x} = x_k$, $\mathbf{y} = y_m$ occurring is calculated as $P\{\mathbf{x} = x_k, \mathbf{y} = y_m\} = p_k \times q_m$.

Using these results, it follows that given the two discrete random variables $\mathbf{ECP_A}$ defined by $P\{\mathbf{ECP_A} = ECP_{A,k}\} = p_k$ and $\mathbf{ECP_B}$ defined by $P\{\mathbf{ECP_B} = ECP_{B,m}\} = q_m$, the random variable for the total ECP from the two, $\mathbf{ECP_{TOTAL}}$, would be defined by:

$$P\{\mathbf{ECP_{TOTAL}} = ECP_{TOTAL,k,m} = ECP_{A,k} \times ECP_{B,m}\} = p_k \times q_m \tag{4.12}$$

when the ECP values are expressed in linear units and:

$$P\{\mathbf{ECP_{TOTAL}} = ECP_{TOTAL,k,m} = ECP_{A,k} + ECP_{B,m}\} = p_k \times q_m \tag{4.13}$$

when the ECP values are expressed in dB.

Importantly, this technique applies even if the ECP effect from two impairments are dependent on each other, using any mapping f such that $ECP_{TOTAL} = f(ECP_{A,k}, ECP_{B,m})$, so long as the two random variables $\mathbf{ECP_A}$ and $\mathbf{ECP_B}$ are statistically independent, which in the context of this work means that the temporal occurrences of impairments A and B are not statistically correlated.

To reiterate, it is important to recognise the distinction between the two concepts of:

- Statistical independence between the temporal probability mass functions of the ECP impairment values, and,
- Dependence between the values of ECP_A and ECP_B in calculating the value of ECP_{TOTAL}.

The first concept affects the values of P{$\mathbf{ECP_{TOTAL}}$}, while the second concept affects the individual values of $ECP_{TOTAL,k}$.

Using these techniques, an example is shown in Figure 4.5 where ECP PMFs transformed from the impairment PMFs in Figure 4.1, Figure 4.2 and Figure 4.3 associated with DGD, RCD and OSNR are combined into a single PMF for ECP_{TOTAL}.

Observe that the ECP_{TOTAL} PMF has many more "bins" than the individual ECP

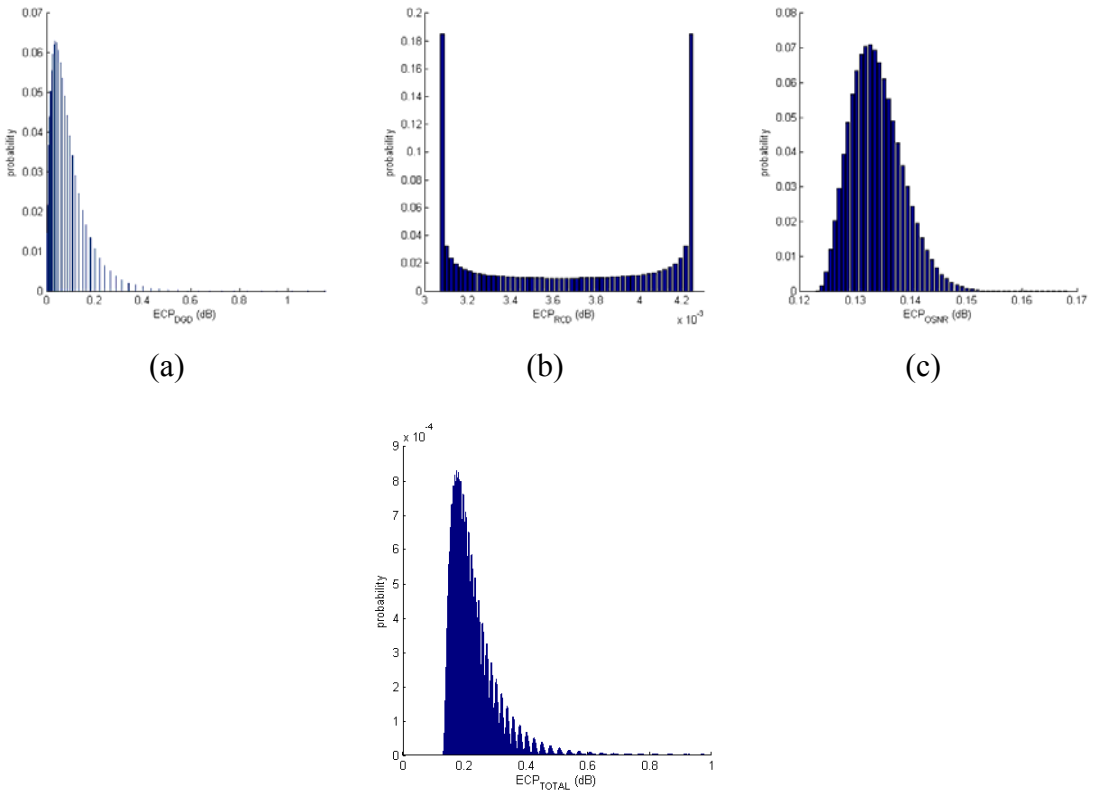

(a) (b) (c)

(d)

Figure 4.5: (a) ECP_{DGD}, (b) ECP_{RCD} and (c) ECP_{OSNR} used to compute (d) ECP_{TOTAL}

PMFs. This is because the number of possible values for ECP that result from combining the individual ECP PMFs is a product of the number of bins for each of the individual ECP PMFs. Computationally, this can become an issue if each of the impairment PMFs have a large number of bins. An analysis of the computation complexity of the ECP PMF combination process will be shown later.

4.4.3 COMPUTING OUTAGE PROBABILITY

The final steps to compute the overall outage probability from the optical impairments use the same method to transform the ECP_{TOTAL} PMF to the Q-factor PMF and then to the BER PMF as in section 4.4.1. The relationships used to transform the ECP_{TOTAL} PMF to the Q-factor PMF is given by:

$$Q_R = \frac{\beta G_{T,R} Q_T ECP_{TOTAL}}{\beta + Q_T (G_{T,R} ECP_{TOTAL} - 1)} \tag{4.14}$$

where $\beta = 1$, and $G_{T,R} = 1$ and:

$$BER = \frac{1}{2}\left[1 - \text{erf}\left(\frac{Q_R}{\sqrt{2}}\right)\right] \tag{4.15}$$

Figure 4.6 shows the Q-factor and BER PMFs obtained using this procedure from the

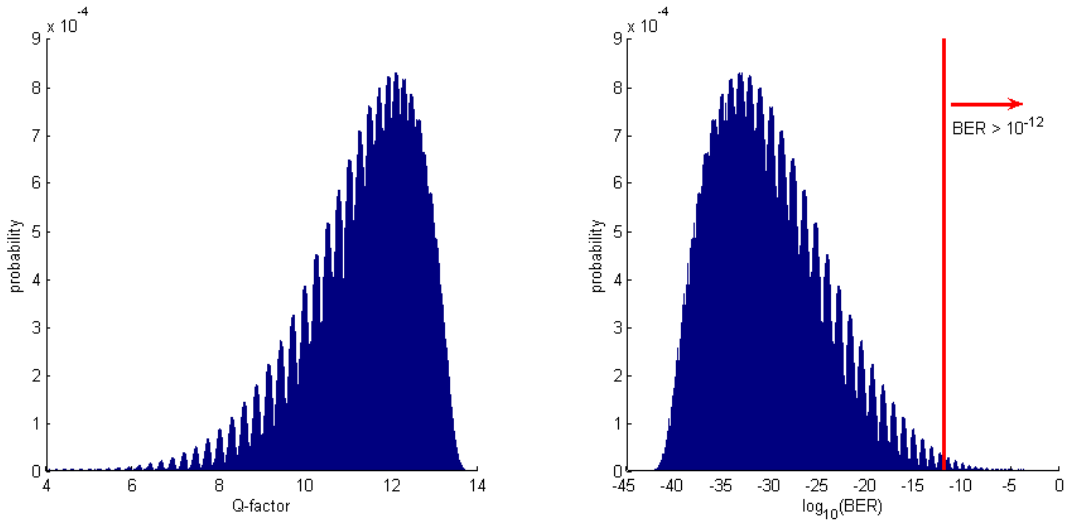

(a) (b)

Figure 4.6: (a) Q-factor PMF, (b) BER PMF

ECP_{TOTAL} PMF from Figure 4.5d. The observed "ripples" in the PMF are a result of the discrete natures of the input PMFs. The final value for the outage probability can then be found by taking the sum of all the probability values for which the BER values are greater than the specified threshold. In Figure 4.6, the red line corresponds to the BER threshold value $\Omega = 10^{-12}$, so the outage probability would be the sum of all the probability values to the right of the line, or mathematically:

$$P_{outage} = \sum_{k} P(\mathbf{BER} = BER_k) \text{ , where } BER_k > \Omega \qquad (4.16)$$

Figure 4.7 provides a flow chart of the steps required in computing the outage probability from multiple optical impairments.

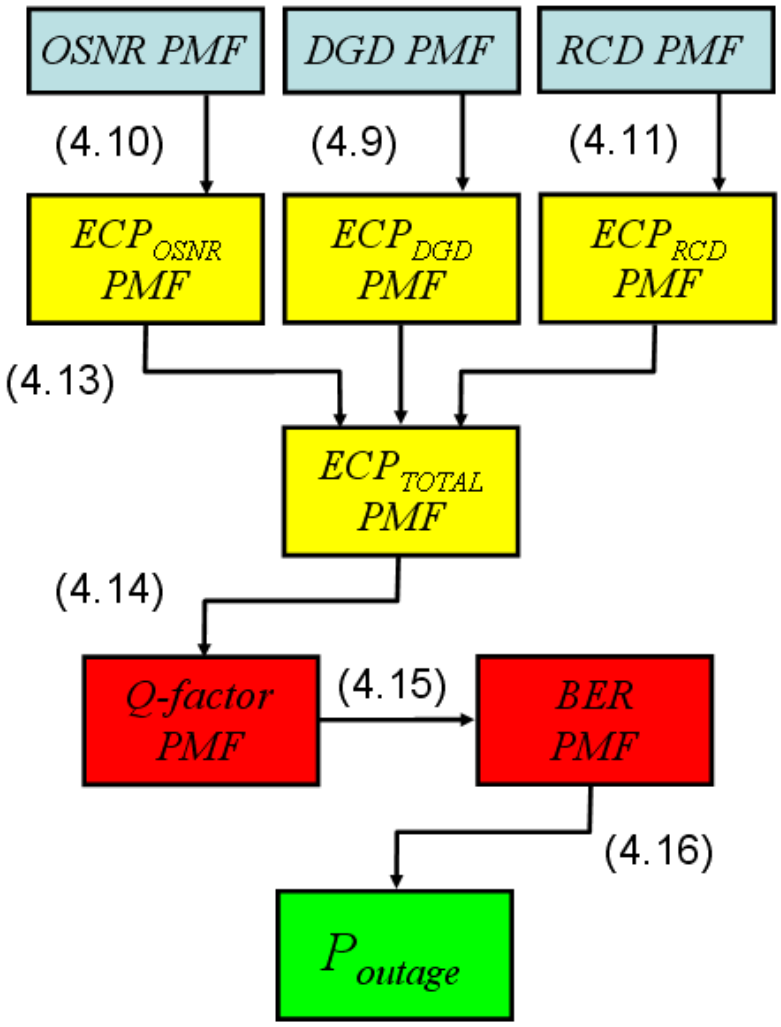

Figure 4.7: Outage probability computation flow chart using OSNR, DGD and RCD as an example

4.4.4 COMPUTATIONAL COMPLEXITY AND ESTIMATION ACCURACY

As has previously been mentioned, the computation complexity of the above outage probability estimation method is dependent upon the number of calculations required at the ECP combining stage.

If each of the M individual ECP PMFs is characterised by N histogram bins, then the algorithmic complexity of computing the total ECP PMF will be $O(N^M)$, bounded by a polynomial function in N, and exponential in M. Given that the number of impairments, M, is relatively constant, it is expedient to keep N as small as possible, both in terms of data storage, and the outage probability computation time. The trade off is that decreasing N also decreases the accuracy of the outage probability estimation, because the PMF resolution is coarser.

As an example, the algorithm to compute the outage probability was executed using Matlab on an Intel 1.8GHz Dual Core CPU, whilst varying the number of bins, M, and recording the average computation time over 20 tests as well as the computed outage probability P_{outage}, the results of which are shown in Figure 4.8. It can be seen in Figure 4.8a that for $N \geq 50$, the outage probability appears to settle to an equilibrium value, while the blue points in Figure 4.8b fit a 4th order polynomial, represented by the red line, confirming our computational complexity analysis.

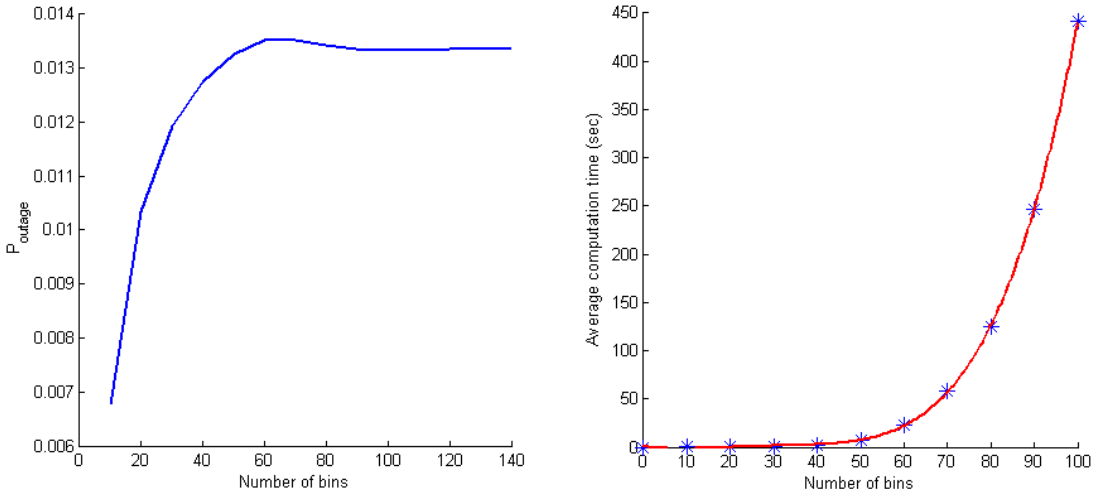

(a) (b)

Figure 4.8: (a) Outage probability vs. N, (b) Computation time vs. N

4.5 OUTAGE PROBABILITY SIMULATIONS

To examine the efficacy of the model developed in section 4.3, the method outlined in section 4.4 was used to compute the outage probability using the parameters listed in Table 4.1. Note that the parameters controlling the distribution of the PDL affecting OSNR and the seasonal variation in RCD are constants independent of the bit rate of the system. Using the results of 4.4.4 the number of bins, N, was chosen to be 50, as a trade off between the computation time required (≈ 6 seconds per run) and the accuracy of the outage probability estimation.

Table 4.1: Outage probability simulation parameters

Bit Rate	Parameter	Range	Increments
All	N	50	-
	PDL_{ave}	0.5 dB	-
	ΔRCD	8 ps/nm	-
10 Gbit/sec	$OSNR_{ave}$	10 to 50 dBm/nm	2 dBm/nm
	DGD_{ave}	0 to 40 ps	2 ps
	RCD_{ave}	0 to 1000 ps/nm	50 ps/nm
40 Gbit/sec	$OSNR_{ave}$	12 to 48 dBm/nm	4 dBm/nm
	DGD_{ave}	0 to 20 ps	2 ps
	RCD_{ave}	0 to 100 ps/nm	10 ps/nm
100 Gbit/sec	$OSNR_{ave}$	16 to 48 dBm/nm	4 dBm/nm
	DGD_{ave}	0 to 10 ps	1 ps
	RCD_{ave}	0 to 10 ps/nm	1 ps/nm

4.5.1 10 GBIT/SEC NRZ RESULTS

Figure 4.9 shows a 4 dimensional plot with the x, y and z axes representing the average OSNR, DGD, and RCD values, and the point colour representing the computed outage probability with an outage defined to occur where BER > 10^{-12}.

This plot shows that there is a "knee" region in which there is a sharp rise in the outage probability as a function of the average OSNR. When $OSNR_{ave}$ is greater than approximately 30 dBm/nm, and DGD_{ave} is low, the system is relatively insensitive to the effect of RCD. As the value of $OSNR_{ave}$ drops below 30 dBm/nm, the effect of RCD becomes particularly significant, with a rapid transition from P_{outage} = 0 to P_{outage} = 1 within a very small range of RCD_{ave}.

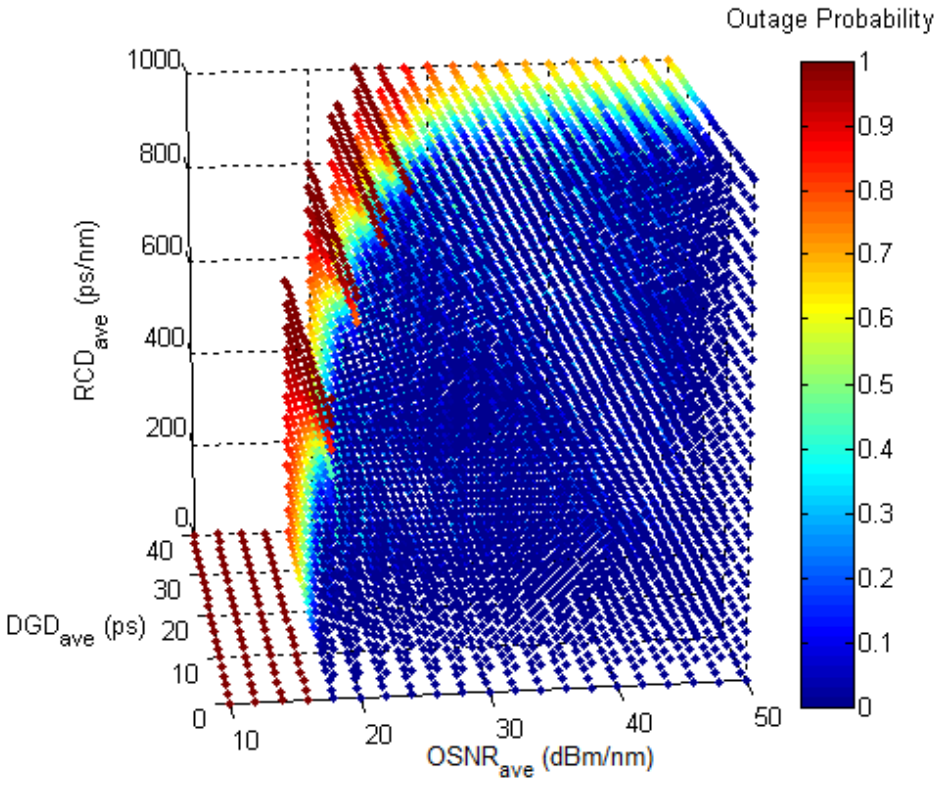

Figure 4.9: P_{outage} vs. $OSNR_{ave}$, DGD_{ave} and RCD_{ave}

The effect of DGD_{ave} is less pronounced, as can be seen in Figure 4.10, where the colour representing outage probability along the DGD_{ave} axis changes much more gradually.

The most useful aspect of Figure 4.9 and Figure 4.10 is that they quantify the interaction between the three impairments, showing that the outage probability due to PMD is relatively independent of OSNR and RCD, but that the outage probability due to RCD depends largely on the OSNR. For a bit rate of 10 Gbit/sec, it appears that ASE is the dominant impairment that determines the outage probability of the system, which is consistent with other findings [65], [123].

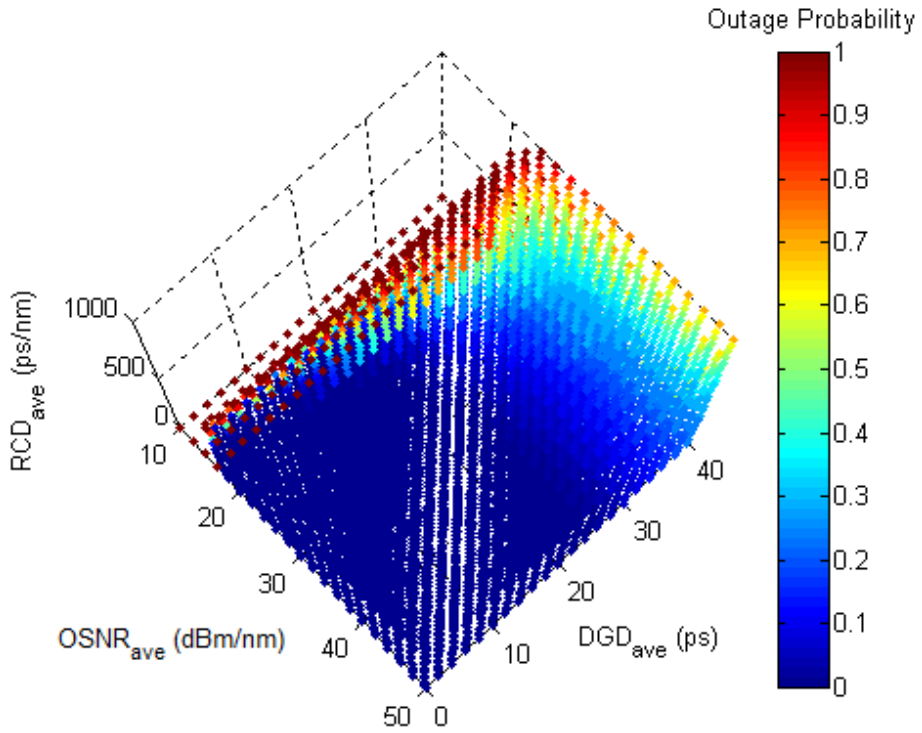

Figure 4.10: P_{outage} vs. $OSNR_{ave}$, DGD_{ave} and RCD_{ave}

4.5.2 40 GBIT/SEC AND 100 GBIT/SEC NRZ RESULTS

The outage probability simulations were re-run using the impairment to ECP relationships corresponding to 40 Gbit/sec and 100 Gbit/sec systems from section 3.7.1.2.3 and section 4.4.1, with the results shown in Figure 4.11 and Figure 4.12. These relationships represent the increased effect that waveform distortion effects such as PMD and RCD have on the ECP and hence the BER of higher bit rate signals.

As can be seen in both plots, the outage probability rapidly approaches 1 for values of PMD_{ave} and RCD_{ave} that are much lower than in the 10 Gbit/sec case. In fact, the tolerance of the 40 Gbit/sec system to RCD is at most about 60 ps/nm when there is no ASE or PMD. The system is even less tolerant to PMD, with the outage probability rapidly approaching 1 with a DGD_{ave} of 5 ps.

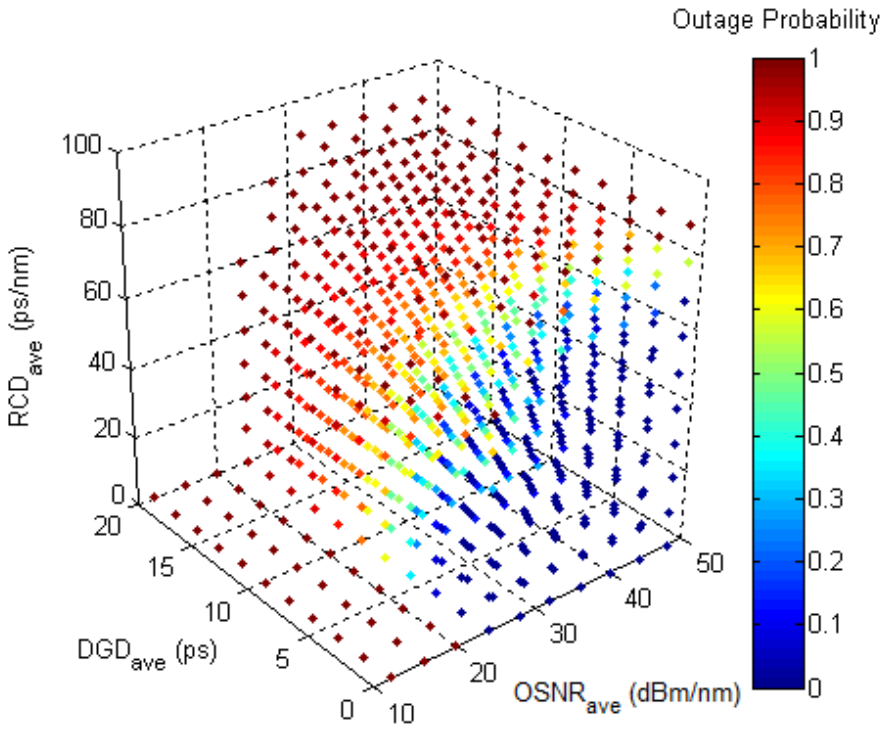

Figure 4.11: P_{outage} vs. $OSNR_{ave}$, DGD_{ave} and RCD_{ave}

These findings are highlighted even more in the 100 Gbit/sec system, with the outage probability growing quickly from a DGD_{ave} of 2 ps and RCD_{ave} of 2 ps/nm. The outage probability relationship with $OSNR_{ave}$ remains relatively constant. ASE no longer dominates the outage probability as it did with the 10 Gbit/sec case. In fact, PMD appears to be the limiting factor for 100 Gbit/sec bit rates. The results presented for higher bit rate systems are consistent with what is known about PMD and RCD. Both cause inter-symbol interference that is much more detrimental when the bit rate is increased as the bit period is correspondingly reduced.

Recall that over a year, seasonal variations in soil temperature can cause the RCD to vary by as much as 8 ps/nm in 500 km of single mode fibre. While this is an insignificant amount for 10 Gbit/sec systems, it becomes significant at 40 Gbit/sec and critical in 100 Gbit/sec systems, highlighting the need for dynamic dispersion compensation [114] if NRZ modulation were to be used.

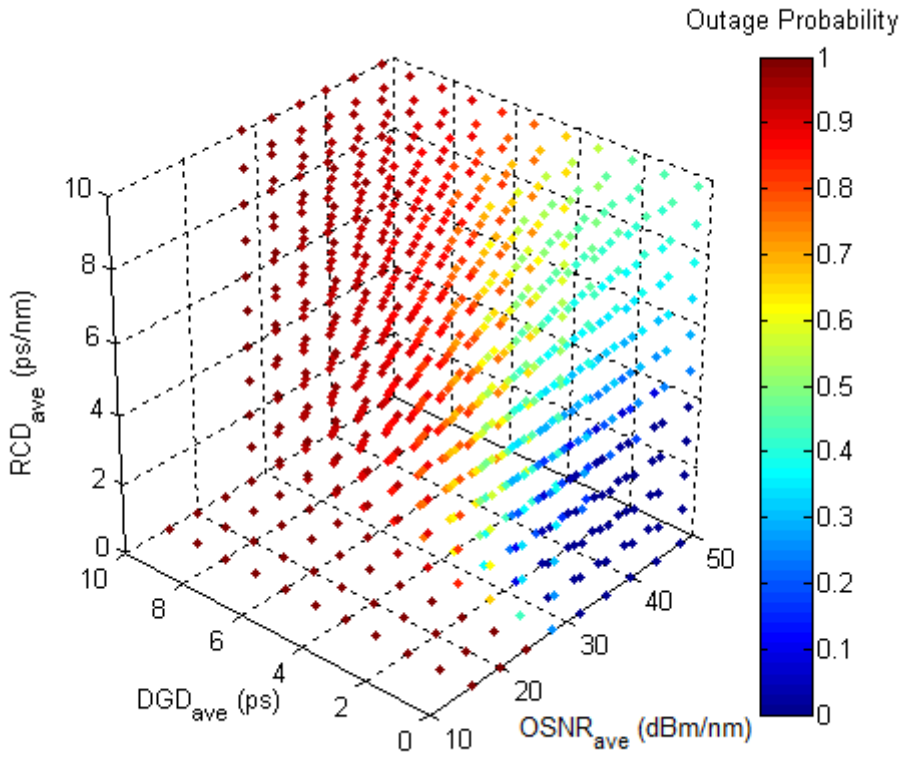

Figure 4.12: P_{outage} vs. $OSNR_{ave}$, DGD_{ave} and RCD_{ave}

4.6 SUMMARY, DISCUSSION AND CONCLUSIONS

4.6.1 SUMMARY

In this chapter, a method for calculating the outage probability of an optical connection due to multiple optical impairments was presented. Outage probability is commonly defined as the probability that the bit error rate (BER) of a connection exceeds a threshold (e.g. 10^{-12}) and is of interest to telecommunications network operators, which are increasingly offering service level agreements to customers as a competitive differentiator. Previously, this was only considered for single impairments such as polarisation mode dispersion (PMD) or residual chromatic dispersion (RCD).

In addition to the well known temporal characteristics of PMD (characterised by a Maxwellian distribution of the differential group delay (DGD)), the literature shows that seasonal soil temperature variations can alter the temperature of buried optical fibre, causing the RCD to change. There is also prior work that relates polarisation dependent loss (PDL) to time variations in the OSNR and EDFA transients to short term variations in ASE power.

Optical performance monitors are expected to be able to provide a wealth of information regarding multiple optical impairments, including histograms of instantaneous impairment values. These histograms are directly analogous to probability mass functions (PMF) and can be treated as discrete random variables. Applying probability theory to these random variables, it was shown that it is possible to use the framework developed in chapter 4 to compute a PMF of the total ECP due to multiple optical impairments. From the PMF of the ECP, the PMF of the Q-factor and BER was calculated, ultimately yielding a total outage probability. This process is re-summarised in Figure 4.13.

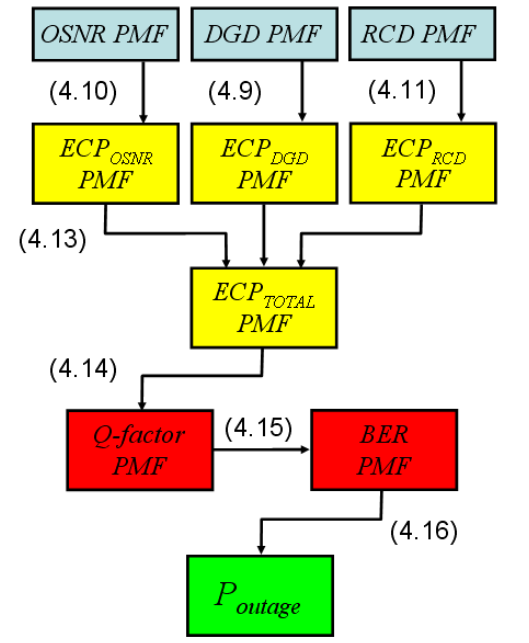

Figure 4.13: Outage probability computation flow chart

As a demonstration, the method was applied to three linear impairments in the form of PMFs of the OSNR, DGD, RCD of an optical connection for various mean values of those impairments. It was shown that for a bit rate of 10 Gbit/sec, the effects of PMD and RCD on the outage probability are dominated by the effect of OSNR, while at bit rates of 40 Gbit/sec and 100 Gbit/sec, both PMD and RCD were major contributors to the outage probability. In fact, variations in the average DGD by 2 or 3 ps and RCD of just 3 or 4 ps/nm could cause the outage probability to vary from 0 to 1. The results show that for higher bit rate systems, small variations in impairment values need to be considered and accounted for.

An analysis was performed on the computation complexity of the method and showed that the simplest implementation was polynomial in the number of histogram bins for each of the impairments, and exponential in the number of impairments. It was also shown that there was a necessary trade off between the accuracy of the outage probability calculation and the computation time, both of which are directly related to the number of histogram bins.

4.6.2 DISCUSSION

Optical performance monitoring is a key component of next generation optical networks [117], [96], [69] able to provide a wealth of data that can enable better, and automated, management of the network. By collecting data on impairment values over extended periods of time, this work has outlined a method that network operators can calculate the outage probability of a network path from the histograms of optical impairments. This simple calculation, however, relies on a number of factors and assumptions that must be addressed.

The most critical factor is the requirement of statistical independence between the temporal variations of the optical impairments to enable a simple calculation of the combined ECP PMF. To date, there is no evidence to suggest that there is any significant relationship between the time evolution of DGD, RCD and OSNR. However, if this is not the case multi-dimensional joint PMFs of the relevant impairments can be measured by the optical monitors to account for any such time correlation.

Not to be confused with the statistical independence requirement mentioned above, it is not necessary that the effect on the ECP or Q-factor of two impairments be independent of each other. An example of this in the literature is that the effect of PMD on outage probability is dependent on the amount of polarisation dependent loss (PDL) also in the system [115]. In the example presented, this effect was ignored, but it can be accounted for in the calculation of the ECP value by using the same techniques as in section 3.7.2 for inter-channel crosstalk and 3.7.3 for non-linear effects, where the ECP value was found from a combination of two or more impairments.

Finally, it should be remembered that the transformation between the impairments, ECP, Q-factor and BER are bit rate and modulation format dependent relationships. In the examples presented in this chapter, the modulation format was assumed to be NRZ modulation, and the calculation of the BER assumed that the receiver statistics conformed to Gaussian statistics. It has been shown in section 3.7.4 that for DPSK, these relationships are different, and it would be expected for this to also be the case

for other modulation formats. It should be stated that as long as relationships exist between the impairments, ECP, an appropriate Q-factor and the BER, the techniques presented in this thesis could probably be modified and applied to obtain values for the BER and outage probability.

Future experimental work could involve validation of this model using real statistics from optical performance monitors that could monitor impairment level histograms and the histograms of Q-factor or BER. In the algorithmic domain, more efficient methods of computing the combined ECP PMF distribution could reduce computation time, enabling better accuracy and possibly real time calculation of path outage probability for use in routing. Dependence between the effects on the ECP, and temporal occurrences, of optical impairments could be studied to help refine the models developed in this thesis.

4.6.3 CONCLUSIONS

From the data collected and the results presented in this chapter, a number of important conclusions can be made and are listed below.

- The method of using the ECP to estimate the Q-factor and BER from multiple optical impairments developed in chapter 3 can be used to calculate the outage probability of a connection, using simple probability theory.
- There is a trade off between the accuracy of the outage probability calculation and the computation time using the presented method.
- Temporal variations in optical impairment values, as small as 2 or 3 ps of DGD, or 2 to 3 ps/nm RCD, can cause significant outage probability, highlighting the need for dynamic PMD and RCD compensation in high bit rate systems.

In the next chapter, it will be shown how the outage probability computed in this chapter can be used to obtain useful statistics on the probability of connection request blockage due to both physical impairments and user traffic requests, which will be termed the “failure probability”.

5 Failure Probability

5.1 INTRODUCTION

In the provisioning of resources in a network, a network operator needs to maintain a balance between providing enough resources to satisfy customer requirements and the cost of operating a sustainable network. A key metric for switched WDM networks is the probability that a request for network resources (such as wavelengths) from a customer is denied due to a lack of resources (often due to wavelength continuity issues), commonly called the "blocking probability".

As seen in section 2.4, the deployment of intelligent all-optical networks presents new challenges in network dimensioning as signal quality issues become more significant due to longer network paths that have higher levels of optical impairments. It would be extremely useful for network providers to have a composite metric for a path that accounts for both the probability of wavelength blocking and the probability of outage associated with physical impairments on that path.

This chapter shows that the outage probability metric from chapter 4 and BER from chapter 3, calculated from multiple optical impairments, can be used to find a combined wavelength blocking and physical layer outage probability, termed "failure probability". The failure probability would be an important metric for network designers to gauge the overall sustainability of an allocated path. This can be calculated analytically for a small number of links, but often requires simulation for realistically sized networks. This work demonstrates how the method for estimating the Q-factor and outage probability from multiple impairments can be used by network designers and queuing theorists to better provision switched WDM networks.

5.2 TELETRAFFIC ENGINEERING

Teletraffic engineering is the "application of probability theory to the solution of problems concerning planning, performance evaluation, operation, and maintenance of telecommunication systems" [124] but has applicability in many areas such as road traffic, customer service, manufacturing and storage management to name a few. The tools of teletraffic engineering are stochastic processes, queuing theory and numerical simulation.

5.2.1 STOCHASTIC PROCESSES

A "stochastic process", or random process, is a collection of random variables that may or may not be identically distributed and/or independent of each other. In telecommunications, a stochastic process is often used to model customer behaviour parameters such as the inter-arrival and holding time of calls to a telephone network, or analogously in the context of this chapter, connections in switched WDM networks. These definitions are illustrated in Figure 5.1 that shows the state of a WDM wavelength.

The most versatile and commonly used distribution to model inter-arrival and holding times is the exponential distribution, also called the negative exponential distribution, which can be characterised by a single parameter, α, corresponding to the mean of the distribution.

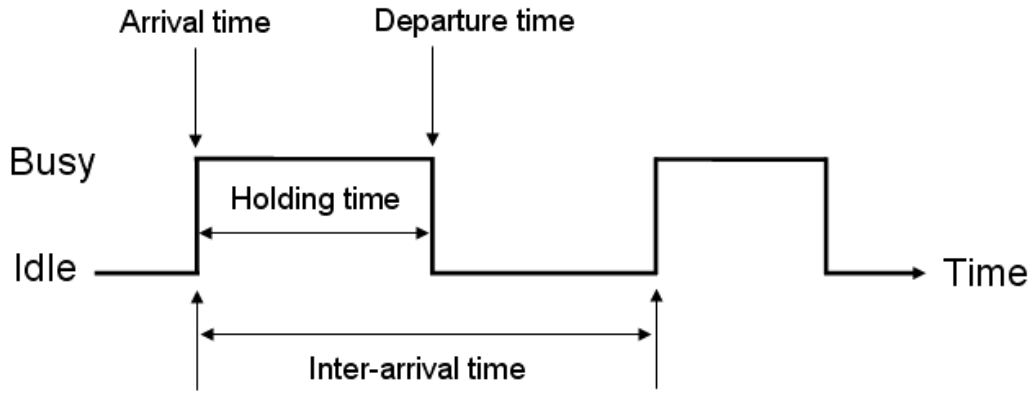

Figure 5.1: Inter-arrival and holding time definitions

The probability density function, $f(t)$ and cumulative probability density function $F(t)$ for the exponential distribution are [125]:

$$f(t) = \alpha \, \mathrm{e}^{-\alpha t} \tag{5.1}$$

$$F(t) = 1 - e^{-\alpha t} \tag{5.2}$$

where t in this case is in units of time. The mean m and standard deviation σ are:

$$m = \frac{1}{\alpha} \tag{5.3}$$

$$\sigma = \frac{1}{\alpha^2} \tag{5.4}$$

The most fundamental property of the exponential distribution is that it is "memoryless". When modelling connection holding times, this means that the residual time, r, to wait before the connection departure is independent of the amount of time that has already passed, s, since the connection arrival. Mathematically, this is written as:

$$f(r + s \mid s) = f(r) \tag{5.5}$$

The exponential distribution is the only continuous probability distribution and the geometric distribution the only discrete probability distribution that exhibit the memoryless property. Importantly, the sum of two exponential random variables of rate α and μ is another exponential random variable with rate $(\alpha + \mu)$.

When the exponential distribution is used to model the inter-arrival time (of mean $1/\alpha$ units of time) between incoming connections, the number of arrivals within an arbitrary, fixed time interval are equivalently modelled by a "Poisson arrival process" with rate α connections per unit time [125]. Thus, the Poisson arrival process describes connection arrivals that have exponentially distributed inter-arrival times. In practice, the exponential distribution is an extremely good model of random customer behaviour.

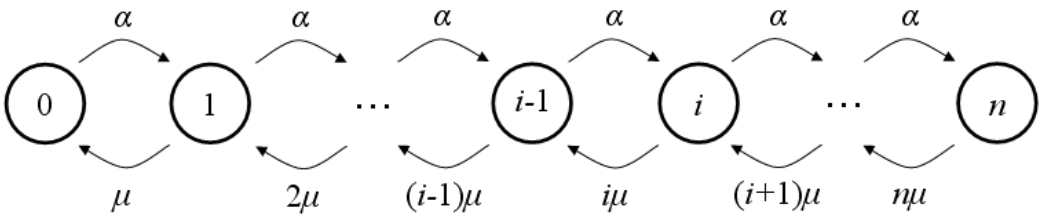

Figure 5.2: Example state transition diagram

5.2.2 STATE TRANSITION DIAGRAMS AND BLOCKING PROBABILITY

A telecommunications network is a combination of deterministic (hardware and software algorithms) and stochastic (user) systems. A powerful technique to model such a system is the state transition diagram. Consider a single optical fibre that carries n wavelengths. Assume that incoming connections arrive according to a Poisson process at a rate of α connections per unit time, and that the connection holding time is exponentially distributed with mean $1/\mu$ units of time. For simplicity, assume that only one connection can be assigned to each wavelength, a connection can be assigned to any available wavelength and that all wavelengths are treated equally. It is possible, then, to define the state of the system in terms of the number of busy channels, i, and to construct the state diagram shown in Figure 5.2.

Here, the system transitions from state i to $(i + 1)$ at a rate of α connections per unit time, and from i to $(i - 1)$ at a rate of $i\mu$ connections per unit time. Importantly, the system is memoryless – the transition rate from one state to another depends only on the present state and not on any past state (called the "Markov property" [126]) and this type of state diagram is often called a "Markov chain".

When the system is in statistical equilibrium, the probability that an observation of the system sees that the system is in state i, $p(i)$, is equal to the long-term proportion of time that the system spends in state i. The blocking probability is the equilibrium probability that an incoming connection observes the system to be in state n, or $p(n)$, where all wavelengths in the system are in use and the incoming connection must be blocked.

5.2.3 OBTAINING EQUILIBRIUM PROBABILITIES

5.2.3.1 ANALYTIC TECHNIQUES

To analytically compute the equilibrium probability $p(i)$ that the modelled system is in state i, the equations governing the transitions between states need to be solved. When the system is in statistical equilibrium, the net rate of transitions (i.e. in and out) for each state must be zero and the "probability flow" rates into and out of state i must be equal, for all i. This means that for the system described in Figure 5.2, the following equations can be written for each state:

$$\alpha p(0) = \mu p(1), \qquad i = 0 \tag{5.6}$$

$$\alpha p(i) + i\mu p(i) = \alpha p(i-1) + (i+1)\mu p(i+1), \qquad i > 0 \tag{5.7}$$

With the additional constraint that the sum of all the probabilities $p(i)$ must be 1:

$$\sum_{i=0}^{n} p(i) = 1 \tag{5.8}$$

Solving these equations simultaneously will thus yield the equilibrium probability of the system occupying any particular state at a random instant, from which the blocking probability may be found ($p(n)$). This can be solved in a variety of ways, for example by rewriting all of the equations in terms of $p(0)$ and using (5.8), or by expressing the set of simultaneous equations given by (5.6) and (5.7) in matrix form:

$$\begin{bmatrix} -\alpha & \mu & 0 & 0 & 0 \\ \alpha & -\mu-\alpha & 2\mu & 0 & 0 \\ 0 & \alpha & -2\mu-\alpha & \ddots & 0 \\ 0 & 0 & \ddots & \ddots & n\mu \\ 0 & 0 & 0 & \alpha & -n\mu \end{bmatrix} \begin{bmatrix} p(0) \\ p(1) \\ p(2) \\ \vdots \\ p(n) \end{bmatrix} = \begin{bmatrix} 0 \\ 0 \\ 0 \\ \vdots \\ 0 \end{bmatrix} \tag{5.9}$$

Solving this system directly using a matrix inversion or Gauss-Seidel iteration would yield an infinite number of solutions, because one of the equations will always be linearly dependent on the others [127], so the additional constraint (5.8) must be substituted for one of the rows, giving:

$$\begin{bmatrix} -\alpha & \mu & 0 & 0 & 0 \\ \alpha & -\mu-\alpha & 2\mu & 0 & 0 \\ 0 & \alpha & -2\mu-\alpha & \ddots & 0 \\ 0 & 0 & \ddots & \ddots & n\mu \\ 1 & 1 & 1 & \cdots & 1 \end{bmatrix} \begin{bmatrix} p(0) \\ p(1) \\ p(2) \\ \vdots \\ p(n) \end{bmatrix} = \begin{bmatrix} 0 \\ 0 \\ 0 \\ \vdots \\ 1 \end{bmatrix} \tag{5.10}$$

the solution of which gives the correct values for $p(i)$.

Solving this system analytically yields the well known Erlang's B distribution [124], which is also referred to as the "Truncated Poisson" distribution:

$$p(i) = \frac{\frac{1}{i!} \cdot \left(\frac{\alpha}{\mu}\right)^i}{\sum_{j=0}^{n} \frac{1}{j!} \cdot \left(\frac{\alpha}{\mu}\right)^j} \tag{5.11}$$

The limiting factor for efficient computation of $p(i)$ in all of these analytic techniques is the number of states, i. Recall that this example system only models a single link with capacity n wavelengths, and thus the number of system states is n. Now consider modelling a system with k links, each with capacity n wavelengths, for simplicity. This system is fully specified by n^k distinct states corresponding to all the possible combinations of the number of wavelengths occupied on each of the k links. Thus, the number of states grows exponentially in the number of links and polynomially in the capacity of each link.

5.2.3.2 MARKOV CHAIN MONTE CARLO SIMULATIONS

Clearly, the exact analytical approach to calculating connection blocking probability cannot be used for large telecommunications networks that have a vast amount of system states and arbitrarily complex routing between source-destination pairs. For such systems, a Markov chain Monte Carlo (MCMC) computer simulation is the technique of choice. Computer code can be written to directly implement the specifications of the Markov chain state transition diagram, allowing for very general system behaviour to be modelled. The system is then simulated for a large number of random events (Monte Carlo method), corresponding to connection arrivals and departures.

As connections enter and exit the system, the system state changes. If the system is in a state where all wavelengths are occupied, additional incoming connections are blocked and a blocking counter incremented. The connection blocking probability is then calculated as the ratio of the number of blocked connections to the total number of connection attempts. For a system with Poisson arrivals, which are all of the same class, this value is also equal to the "Time Congestion" - the long-term proportion of time spent by the system with all wavelengths occupied.

The MCMC simulation technique relies on the fact that the sum of independent Poisson arrival processes with various rate parameters, e.g. α_1, α_2, …, α_i, is a Poisson arrival process with rate ($\alpha_1 + \alpha_2 + \ldots + \alpha_i$) [128]. For the system specified in Figure 5.2, connection arrivals and departures are treated equally as "events". This means that the "event rate" is the sum of the arrival and departure rates for the system in state i, or ($\alpha + i\mu$). Thus if the system is in state i, the system transitions to state (i+1), corresponding to a connection arrival, with probability $\alpha/(\alpha+i\mu)$ and to state (i–1), corresponding to a connection departure, with probability $i\mu/(\alpha+i\mu)$. If the system is in state $i = n$ and a connection arrival occurs, the connection must be blocked.

Figure 5.3 shows C++ code that implements the state diagram in Figure 5.2. The *rand()* function on line 9 generates a uniformly distributed random on the interval [0, 1] which is then scaled by the event rate that depends on the system state i. If the result, R, is less than α, then a connection arrival has occurred, but if R is greater than α, a connection departure has occurred. Note that the probability that $R < \alpha$ is $\alpha/(\alpha+i\mu)$ and the probability that $R > \alpha$ is $i\mu/(\alpha+i\mu)$, which is consistent with the behaviour specified in the state transition diagram.

Note that it is simple to add code to record the number of times a particular state i, is traversed, resulting in a histogram of the system state, which when normalised, give the equilibrium probabilities of the system being in state i, $p(i)$. Here, the only unspecified parameter is `NUM_EVENTS`. The larger the value of `NUM_EVENTS`, the more accurate the calculated value of blocking probability, at the expense of computation time. As an example, for the system specified in Figure 5.2, using $\alpha = 4$ connections per unit time and $\mu = 1$ connection per unit time, both (5.10) and (5.11) result in $p(n) = 0.03042$. Using the simulation code in Figure 5.3, the blocking probability is

shown in Table 5.1 for different values of NUM_EVENTS. The results show that as the value of NUM_EVENTS is increased, the accuracy of the blocking probability calculated from the MCMC increases.

```
 1  double alpha; // connection arrival rate
 2  double mu; // connection departure rate
 3  double R; // random variable
 4  int attempts = 0; int blocked = 0; // counters
 5  int i = 0; // number of wavelengths in use, initialised to 0
 6  int n; // total number of available wavelengths
 7
 8  for (int events = 0; events < NUM_EVENTS; events++) {
 9      R = rand()*(alpha + i*mu); // generate a random number,
10                                 // dependent on system state i
11      if (R < alpha) { // connection arrival event
12          attempts++; // increment connection attempts
13          if (i < n) { // wavelengths are available
14              i++; // increment system state
15          } else { // no available wavelengths
16              blocked++; // increment blocked connections
17          }
18      } else { // connection departure event
19          i--; // decrement system state
20      }
21  }
22  printf("Blocking probability: %.4f\n", blocked/attempts);
```

Figure 5.3: MCMC simulation code of state transition diagram from Figure 5.2

Table 5.1: Convergence of simulation results as a function of NUM_EVENTS

NUM_EVENTS	blocked	attempts	Blocking probability
100	2	52	0.03846
1,000	18	513	0.03509
10,000	169	5086	0.03323
100,000	1413	50708	0.02787
1,000,000	15269	507637	0.03008
10,000,000	154497	5077250	0.03043

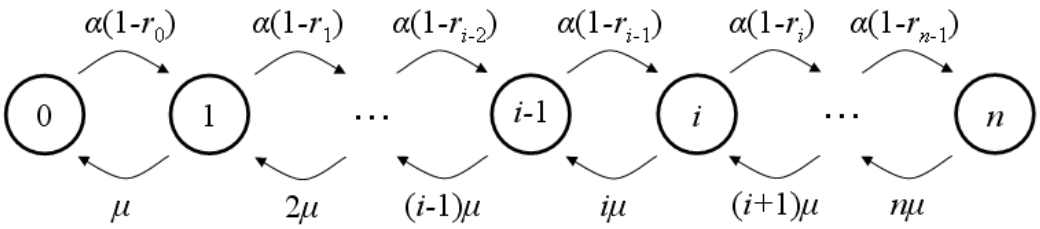

Figure 5.4: State transition diagram for loss system with restricted accessibility

The next section details a method to extend these analytical and simulation techniques to include the effect of physical layer impairments on the overall probability that an incoming connection fails to be granted resources in the single optical fibre link model developed in this section.

5.3 SINGLE LINK FAILURE PROBABILITY

Consider the system studied in the previous section, an optical fibre with capacity of n wavelengths with incoming connection requests at a rate α connections per unit time that have a mean holding time of $1/\mu$ units of time (depart the system at a rate μ connections per unit time). The signals carried on this fibre are subject to a number of optical impairments, such as ASE, PMD and RCD, that are liable to cause the BER of transmitted signals to exceed a specified threshold $\Omega = 10^{-12}$. It would be useful to calculate the combined probability that an incoming connection is not only granted access to the system, but that once admitted, the connection BER does not exceed Ω. This is possible by modifying the system in Figure 5.2.

The system in Figure 5.2 is called a "loss system with full accessibility" [124] because incoming connections have unrestricted access to available wavelengths. It is possible to model the desired behaviour described above using a "loss system with restricted accessibility", shown in Figure 5.4. Here, the rate at which connections are admitted into the system is scaled by a "passage factor", $(1–r_i)$ that is state dependent. The passage factor can restrict access to wavelengths, even if there are wavelengths available to be used.

The outage probability computed from multiple optical impairments using the method in chapter 4 can be directly substituted for r_i. This models the fact that while

there are available resources for an incoming connection, there is a percentage of time (represented by the outage probability) where that connection would not have adequate link signal quality to be sustainable with respect to the BER threshold. Note that since r_i is dependent on the state of the system, effects that depend on the number of wavelengths already in the system can be included, such as crosstalk, FWM and XPM.

The total probability that a connection fails to enter the system, termed the "failure probability", is hence a measure of the combined effect of the blocking probability due to user traffic demands and the outage probability due to physical layer impairments. Importantly, the two are also not independent of each other, as physical layer effects such as four-wave mixing and inter-channel crosstalk depend on the traffic load or number of occupied or active wavelengths.

5.3.1 TRUNK GROUPS

It should be noted that the analysis of this single-link system can equivalently represent a special case of multi-link systems where a number of pre-reserved wavelength continuous paths are terminated by the same end points, shown in Figure 5.5. Here, the red, green and blue solid lines represent a set of connections with coincident end points that are collectively called a "trunk group".

In Figure 5.5, each path in the trunk group can be modelled as a single resource. Assuming that the connections that are not a part of the trunk group, represented by the dotted purple and orange lines, are fixed (so that the physical layer effects of these connections on the trunk group are constant), it is possible to apply the failure probability analysis to this sub-system. In this case, r_i from Figure 5.4 would be the multi-link path outage probability values and α, μ the trunk group connection inter-arrival and departure rates.

This scenario could arise if a network provider were to set up dedicated high capacity end-to-end paths between two points in its network, for example if multiple customers were to request access to a number of wavelengths over co-incident all-optical paths.

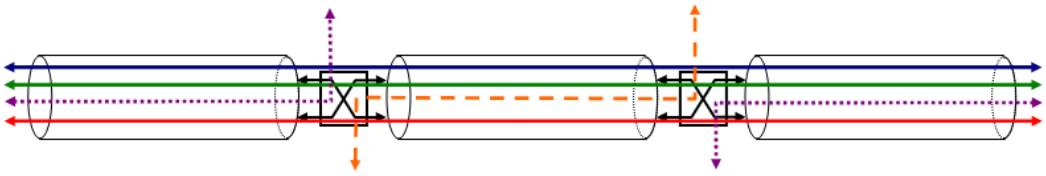

Figure 5.5: Example multi-link system that can be partially modelled by a single link system

5.3.2 ANALYTIC CALCULATION OF FAILURE PROBABILITY

The failure probability can be calculated using alterations to the methods used to calculate the blocking probability. For example, the matrix method with the adjusted state transition rates yields:

$$\begin{bmatrix} -\alpha(1-r_0) & \mu & 0 & 0 & 0 \\ \alpha(1-r_0) & -\mu-\alpha(1-r_1) & 2\mu & 0 & 0 \\ 0 & \alpha(1-r_1) & -2\mu-\alpha(1-r_2) & \ddots & 0 \\ 0 & 0 & \ddots & \ddots & n\mu \\ 1 & 1 & 1 & \cdots & 1 \end{bmatrix} \begin{bmatrix} p^*(0) \\ p^*(1) \\ p^*(2) \\ \vdots \\ p^*(n) \end{bmatrix} = \begin{bmatrix} 0 \\ 0 \\ 0 \\ \vdots \\ 1 \end{bmatrix} \quad (5.12)$$

for which the equilibrium values for $p^*(i)$ can be found. Here, $p^*(n)$ still represents the blocking probability, p_{block}, but an outage can occur also with probability r_i from any other state i, where $i <> n$, meaning that the total outage probability is:

$$p_{outage} = \sum_{i=0}^{n-1} p^*(i) r_i \quad (5.13)$$

The failure probability is hence:

$$\begin{aligned} p_{failure} &= p_{block} + p_{outage} \\ &= p^*(n) + \sum_{i=0}^{n-1} p^*(i) r_i \end{aligned} \quad (5.14)$$

5.3.3 MCMC SIMULATION OF FAILURE PROBABILITY

Figure 5.6 shows the C++ code to simulate the system defined by the state transition diagram in Figure 5.4 to compute the failure probability of the link described in section 5.3.

The key difference in this simulation with respect to the simulation of the full accessibility system in Figure 5.3 is seen on lines 15 and 16. Here, an additional

restriction is placed on the admission of connections into the system – if the random number assigned to S is less than the state dependent outage probability r_i, the connection experiences an outage and cannot be allocated. At the conclusion of the simulation, the failure probability is the sum of the outage and blocking counters divided by the total connection attempts.

To verify the correctness of the simulation code, the values of $\alpha = 4$, $\mu = 1$ and $r_i = 0.03$ (for all values of i) were used to calculate the failure probability, analytically using (5.12)-(5.14) and by the simulation for `NUM_EVENTS` = 10,000,000. Table 5.2 shows the blocking, outage and failure probabilities resulting from these two methods.

```
 1  double alpha; // connection arrival rate
 2  double mu; // connection departure rate
 3  double R, S; // random variables
 4  double[] r;
 5  int attempts = 0; int blocked = 0; int outaged = 0; // counters
 6  int i = 0; // number of wavelengths in use, initialised to 0
 7  int n; // total number of available wavelengths
 8
 9  for (int events = 0; events < NUM_EVENTS; events++) {
10      R = rand()*(alpha + i*mu); // generate a random number,
11                                 // dependent on system state i
12      if (R < alpha) { // connection arrival event
13          attempts++; // increment connection attempts
14          if (i < n) { // wavelengths are available
15              S = rand(); // generate random number in [0,1]
16              if (S < r[i]) { // connection outage
17                  outaged++; // increment outage counter
18              } else { // connection admitted
19                  i++; // increment system state
20              }
21          } else { // no available wavelengths
22              blocked++; // increment blocked connections
23          }
24      } else { // connection departure event
25          i--; // decrement system state
26      }
27  }
28  printf("Blocking probability: %.4f\n", blocked/attempts);
29  printf("Outage probability: %.4f\n", outaged/attempts);
30  printf("Failure prob: %.4f\n", (blocked+outaged)/attempts);
```

Figure 5.6: MCMC simulation code of state transition diagram from Figure 5.4

Note that the blocking probability has been reduced under the same load relative to the previous example in section 5.2.3.2, where outage probability was not considered (p_{block} = 0.03042). This is because some of the connections admitted by the system experience outages due to physical layer impairments. As these connections are removed from the system, the wavelengths that they occupied are allocated to new connections, resulting in a reduction of the blocking probability.

Table 5.2: Analytic vs. simulation results for computing outage, blocking and failure probability

Method	Blocking probability	Outage probability	Failure probability
Analysis	0.02679	0.02920	0.05599
Simulation	0.02681	0.02917	0.05598

5.4 FAILURE PROBABILITY IN ALL-OPTICAL NETWORKS

As shown in the previous sections, the construction and solution of state transition diagrams is an excellent technique to calculate, exactly, the blocking and failure probability in small systems, but this is not the case for large networks, due to the exponential growth in the state space with the number of links and possible paths.

In telephone networks, and traditional optical networks using optical regeneration, the blocking probability commonly refers to the probability that an incoming call or connection cannot gain access to a set of pre-determined fixed paths (sets of links). This has been comprehensively studied, with the most prominent work done in [129]. In all-optical networks without wavelength conversion technology, there is the additional constraint that all the links in a path must use the same particular wavelength. This is called the "wavelength continuity constraint" (WCC). If wavelength conversion is available at all nodes, the blocking probability analysis reduces to that of a telephone network. There have also been studies of the effect of sparsely placed wavelength converters in all-optical networks [130]. The blocking probability due to wavelength availability in all-optical networks without wavelength conversion is considered in [131]-[134] to name a few.

There have been very few attempts at the analytic formulation of the combined effect of traffic and physical layer impairments on the failure probability. The most notable work of this nature is [135], where the authors show how to combine path blocking probability due to the WCC, with a simple signal quality metric that accounts for inter-symbol interference and ASE noise (that are assumed to be static impairments) as receiver noise variances, and a model of crosstalk. Here a connection is considered to have inadequate signal quality should the number of crosstalk terms, related to the number of interfering wavelengths along a path, exceed a certain threshold. The technique is shown to have good agreement with simulation, at 2-3 orders of magnitude less computation time, for the average blocking probability of all paths, but no results are presented as to the accuracy of the analysis for *specific* paths. Additionally, this technique cannot account for inter-channel effects such as FWM or XPM.

Analytic techniques are good for network dimensioning of link capacities that require repeated calculation of blocking probabilities, however it should also be remembered these techniques pertain only to fixed path routing. Detailed analysis of the effects of physical layer impairments on the combined blocking and outage probability, along with dynamic routing and wavelength assignment algorithms, requires the use of simulation.

The strength of the signal quality estimation and outage probability computation methods developed in this thesis is that they can be generally applied to improve the accuracy of any analytic techniques that aim to account for physical layer impairments.

5.4.1 GENERALISED FAILURE PROBABILITY SIMULATION

To demonstrate the full range of applicability of the developed signal quality estimation method from chapter 3 and the outage probability calculation technique from chapter 4, the MCMC simulation from section 5.3.3 was generalised to enable the computation of the failure probability of connections between any two network nodes in arbitrary topologies. As discussed in the previous section, simulation can be

used to study dynamic impairment-aware routing wavelength assignment (IRWA) algorithms as well as in network dimensioning applications.

The network model is shown in Figure 5.7 where the network is specified as a set of nodes, $v_k \in V$, connected by links (v_i, v_j) that contain individual values for physical layer impairments, such ASE, PMD and RCD and physical distance. Each link also has a capacity of C_{ij} enumerated wavelengths $\lambda_0..\lambda_{Cij}$. A path through the network is specified as a set of links, with a wavelength associated with each link. If the wavelength continuity constraint needs to be satisfied, then each link in a path must use the same wavelength.

It is possible to calculate the total ASE, PMD (characterised by the mean DGD) and RCD for a network path between node 1 and node N, by concatenating the individual link values using the following relationships [46]:

$$P_{ASE,total} = \left(\sum_{j=1}^{N-1} P_{ASE,j} \prod_{k=j+1}^{N} G_k + P_{ASE,N} \right) \times 10^{-0.1 L_{res}} \tag{5.15}$$

$$DGD_{ave,total} = \sqrt{\sum_{j=1}^{N} \left(DGD_{ave,j} \right)^2} \tag{5.16}$$

$$RCD_{ave,total} = \sum_{j=1}^{N} RCD_{ave,j} \tag{5.17}$$

where G_k is the net gain/loss of the k-th link and L_{res} (dB) is the residual loss before the receiving node N.

As seen in section 3.7.2.2, the effect of inter-channel crosstalk noise on the signal quality can be characterised by the ratio of the total crosstalk noise power to the

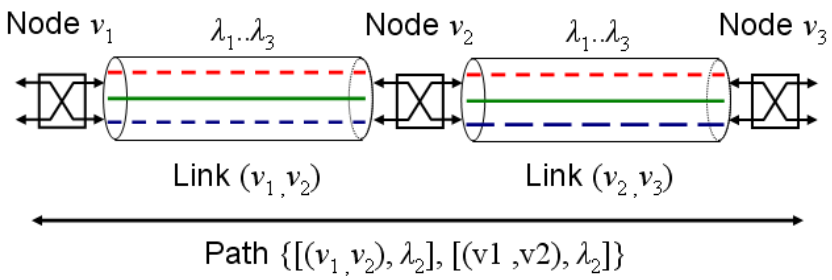

Figure 5.7: Simulation network model

reference signal power. For arbitrary cases, this can be expressed as:

$$OutXT = \frac{\sum_{j=1}^{N} \sum_{\lambda} P_{XT,j,\lambda} N_{XT,j,\lambda}}{P_{sig}} \tag{5.18}$$

where N is each node in the network path, and λ enumerates the interfering channels along each link in the path. If it is assumed that the inter-channel crosstalk power per channel at each node is the same for all interfering channels throughout the network, (5.18) reduces to a function of the total number of interfering channels:

$$OutXT = \frac{P_{XT}}{P_{sig}} \left(\sum_{j=1}^{N} \sum_{\lambda} N_{XT,j,\lambda} \right) \tag{5.19}$$

Assuming the system uses NRZ modulation with bit rate 10 Gbit/sec and 0 dBm launch powers per channel, it is possible to use the methods developed in chapters 3 and 4 to calculate associated BERs and outage probabilities for individual links and multi-link paths. Arbitrarily accurate computation of the outage probability can be computationally time consuming, so a set of lookup tables, based on the relationships in section 4.3, was produced offline that mapped the various combinations of $OSNR_{ave}$, DGD_{ave} and RCD_{ave} and $OutXT$ to a figure for outage probability. Inter-channel crosstalk was included to provide an estimate of the effect of the physical layer interdependence between network connections.

Intra-channel crosstalk and non-linear effects such as SPM/XPM and FWM can similarly be accounted for by altering the OSNR and RCD to ECP relationship depending on the number of interfering wavelengths and transmitter power, but this was not implemented in the simulation due to time constraints.

Traffic generating processes are specified as pairs of nodes ($v_{s.}$, v_d) with an associated arrival rate α_{sd}, and departure rate μ_{sd}. Each node pair has counters to keep track of the number of connections attempted, blocked and outaged between the two nodes.

Figure 5.8 is a flow chart detailing the operation of the generalised MCMC failure probability simulation. In the initialisation phase, the outage probability lookup tables are loaded, along with the network topology. When a connection arrival event occurs, the simulation attempts to find an available path through the network between the source and destination nodes. This is done in the "RWA Calculation" step, where any routing and wavelength assignment algorithm may be used, such as the "First Fit", or "Least Loaded" schemes [137]. If no available wavelength continuous path between the source and destination nodes can be found, the connection is blocked due to lack of available wavelengths, and the counters incremented accordingly. If a path can be found, then one of two things may occur, dependent on the simulation mode:

1. If the simulation is set to run using the outage probability as the physical layer blocking metric then the path outage probability is found using lookup tables and the path impairment values calculated using (5.15)-(5.19). In this case, the path impairment values are treated as *mean* values of distributions as outlined in chapter 4. A random process then determines whether the path experiences an outage (physical layer blocking), and if so rejects the

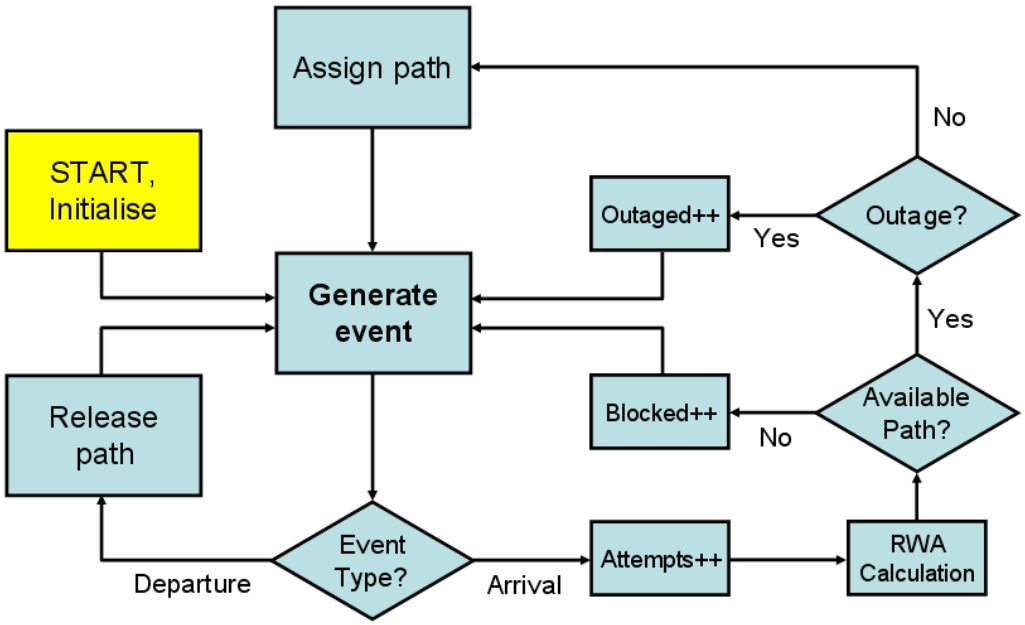

Figure 5.8: Generalised MCMC failure probability simulation flow chart

connection and increments the outage counter.

2. If the simulation is set to run using the static BER as the physical layer blocking metric, then the BER is calculated using the relationships and curve fits found in chapter 3. In this case, the path impairment values are treated as *instantaneous static* values. If the BER exceeds the minimum BER threshold, the connection is rejected and the outage counter incremented.

If no physical layer blocking is experienced, the connection is provisioned, and the corresponding wavelengths on the relevant set of links are marked as busy. When a connection departs the system, the wavelengths on the links that it occupied are freed and marked as idle.

5.5 GENERALISED SIMULATIONS

The algorithms and relationships detailed in section 5.4.1 were implemented in a generalised MCMC simulation. This section demonstrates the use of the developed simulation for determining the failure probability of incoming connections in various standard network topologies, in the presence of ASE, PMD, RCD and inter-channel crosstalk. It is possible to extend the simulation to include additional impairments that can be related to the ECP.

The common simulation parameters for all simulations are shown in Table 5.3.

Table 5.3: Failure probability simulation parameters

Parameter	**Value**
Modulation format	NRZ
Connection bit rates	10 Gbit/sec
Wavelengths per link	8
Fibre chromatic dispersion	17.3 ps/nm/km
Dispersion compensation per 80km span	-1200 ps/nm
EDFA Noise Figure	7 dB
EDFA spacing	80 km
Fibre PMD	0.2 $ps/km^{0.5}$
Channel bandwidth	100 GHz
Inter-channel crosstalk power per channel	-30 dBm
BER threshold	10^{-12}
Mean connection inter-arrival rate	0.1 to 1.2 connections/unit time
Mean connection departure rate	1 connection/unit time

Connection inter-arrival and departure rates were exponentially distributed. The departure rate was set to unit mean so that the offered load could more easily be expressed in Erlangs [136]. The offered load per source-destination pair (S-D pair) was thus varied from 0.1 to 1.2 Erlangs.

The simulations for each topology were run in four different modes, summarised in Table 5.4:

Table 5.4: Simulation modes

RWA "distance" metric	**Wavelength conversion used**	**Physical layer metric**
Distance	Full	None
	None	None
		Static BER
		Outage Probability

The "first fit" routing and wavelength assignment (RWA) [137] algorithm was used for path selection. The "distance" metric used was the physical path distance between the nodes. Full wavelength conversion was used in certain cases to provide baseline best-case performance results for comparison.

Physical layer blocking due to signal quality was either:

1. ignored,
2. applied using the path static BER with threshold of BER < 10^{-12} for connection admission, or
3. applied probabilistically using the outage probability computed from the techniques and parameters covered in section 4.5.1, with BER threshold of 10^{-12}.

The purpose of using both the static BER and the outage probability is to demonstrate that the two metrics should be used for different purposes.

The static BER gives an instantaneous measure of signal quality for the case where the link impairments are at particular levels. When using the static BER as the physical layer blocking mechanism, the network topology can be considered a "snapshot" of the entire time-varying system. The static BER should be used in online routing algorithms, as its computation only requires the evaluation of curve fit equations.

The outage probability should be used in the context of network dimensioning, as it takes into account longer term variations in the BER due to the time-varying nature of the physical layer impairments. Here, the link impairments in the topology are characterised by probability distributions with the specified values considered to be *mean* values. The outage probability requires comparatively more computation than the static BER and is not as suitable for online dynamic path selection (without the use of lookup tables).

In these simulations, the probability distributions for all paths were specified as in section 4.3. In real networks, these distributions are likely to vary for different paths, so characterisation of these paths should be facilitated by optical performance monitors that can track distinct paths, using wavelength tracking technology [138], for example.

In the following results, blue bars represent the connection blocking probability due to lack of available wavelengths. Red bars represent connections that were successfully allocated a path that satisfied the WCC, but had a static BER or that exceeded the minimum BER threshold or probabilistically experienced an outage. The value represented by the height of the red bars is not exactly the physical layer blocking (or outage) probability. This is because a number of blocked connections would experience outages had they been admitted to the system, but this was not measured in this particular simulation implementation. The combined heights of the red and blue bars represent the overall failure probability for connections between specific source-destination pairs.

5.5.1 LINEAR TOPOLOGY

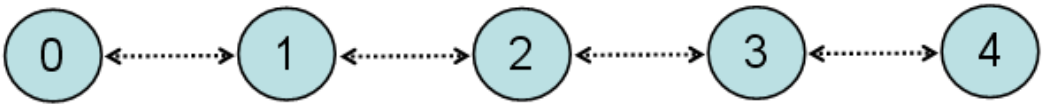

Figure 5.9: 5 node linear topology network

The first network topology investigated was a linear 5 node network connected by bi-directional links, shown in Figure 5.9. The traffic flows in different directions are completely independent and the system could be analysed considering flow in only one direction. The total capacity of the network was 64 wavelengths. In this simple topology, there was only one possible path between each pair of nodes. For the longest path, between nodes 0 and 4, the worst case computed BER was only 1.1×10^{-15} and the worst case computed outage probability was 0, so for a BER threshold of 10^{-12} there should be no instances of physical layer blocking (represented by red bars) for any connections.

The main variation in the results was due to the wavelength continuity constraint (WCC) imposed by the absence or presence of wavelength conversion capability. Figure 5.10 shows a graphical representation of the failure probability matrices for two cases - (a) with and (b) without WCC. The entries in the matrices correspond to the failure probability for all connections attempted between the source nodes (rows, enumerated starting from “node 0”) and the destination nodes (columns, also starting from “node 0”) in the network. For these cases, the offered load between each source-destination pair was 1.2 Erlangs, for a total network offered load of 24 Erlangs.

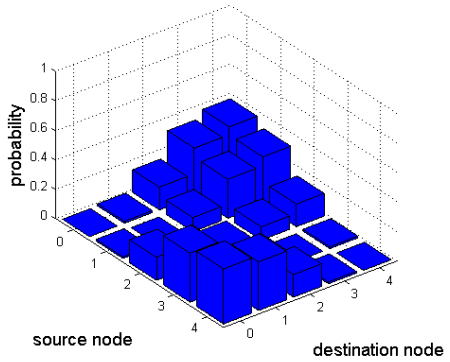

p_{block} (blue bars)

$$\begin{bmatrix} 0 & 0.012 & 0.157 & 0.333 & 0.374 \\ 0.014 & 0 & 0.093 & 0.269 & 0.331 \\ 0.154 & 0.096 & 0 & 0.093 & 0.154 \\ 0.329 & 0.265 & 0.090 & 0 & 0.012 \\ 0.382 & 0.326 & 0.154 & 0.013 & 0 \end{bmatrix}$$

(a)

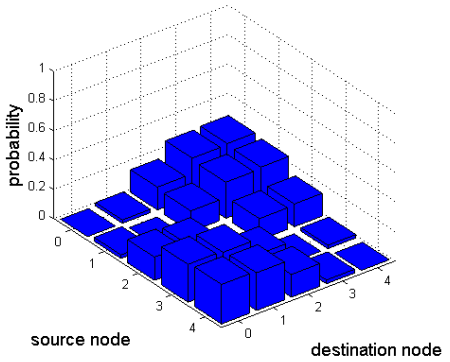

p_{block} (blue bars)

$$\begin{bmatrix} 0 & 0.025 & 0.158 & 0.257 & 0.268 \\ 0.022 & 0 & 0.145 & 0.247 & 0.256 \\ 0.155 & 0.141 & 0 & 0.141 & 0.155 \\ 0.260 & 0.245 & 0.146 & 0 & 0.026 \\ 0.269 & 0.257 & 0.155 & 0.023 & 0 \end{bmatrix}$$

(b)

Figure 5.10: (a) Failure probability with WCC, (b) without WCC, offered load of 1.2 Erlangs/connection

In the case where the WCC was imposed, it can be seen that there is a higher failure probability for the longest paths in comparison to the case where the constraint was relaxed. The average failure probability across all connections was 0.183 in Figure 5.10a and 0.168 in Figure 5.10b, indicating that the use of full wavelength conversion would result in a reduction of the average failure probability in this network. Comparing the failure probability matrices, however, shows that the failure probability for short (1 link) paths increased.

These results can be explained intuitively by fact that the WCC makes it more difficult for connections requesting longer paths to obtain the same coloured wavelength across all links, increasing the failure probability. Short paths are not affected by the WCC, but as more connections with longer paths are admitted into the network, there are less free wavelengths, resulting in an overall increase in the failure probability of the short paths.

5.5.2 RING TOPOLOGY

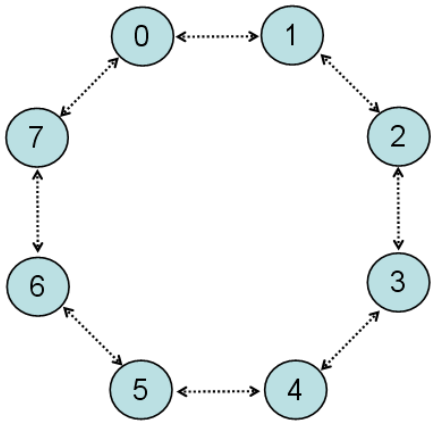

Figure 5.11: 8 node ring topology network

An eight node ring topology, shown in Figure 5.11, was simulated using the same parameters in Table 5.3. This network had a total capacity of 128 wavelengths. In this topology, the longest 4 link paths between opposite nodes had computed worst case outage probabilities of 0 and worst case static BERs were 1.06×10^{-16}, so at first glance, there should be no instances of physical layer blocking.

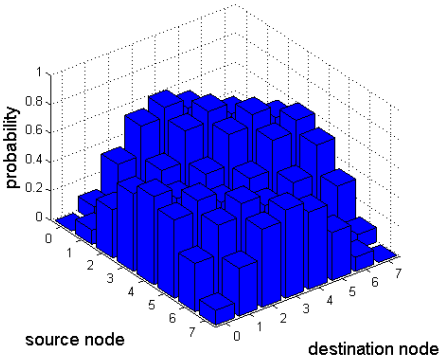

0	0.103	0.336	0.538	0.605	0.539	0.341	0.101
0.099	0	0.104	0.324	0.536	0.608	0.530	0.328
0.332	0.102	0	0.102	0.330	0.542	0.618	0.535
0.534	0.331	0.100	0	0.096	0.331	0.533	0.609
0.607	0.533	0.338	0.094	0	0.099	0.333	0.531
0.539	0.611	0.537	0.324	0.101	0	0.101	0.340
0.332	0.534	0.621	0.547	0.338	0.102	0	0.100
0.102	0.330	0.537	0.608	0.532	0.329	0.097	0

(a)

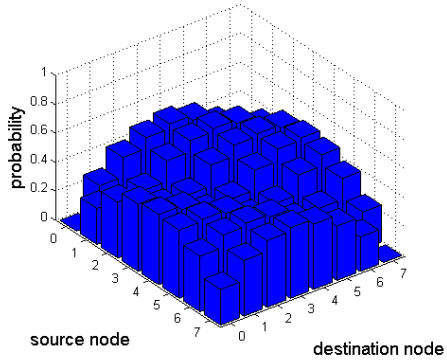

0	0.251	0.384	0.458	0.492	0.456	0.367	0.238
0.249	0	0.249	0.393	0.469	0.491	0.464	0.383
0.384	0.243	0	0.248	0.393	0.469	0.486	0.466
0.463	0.387	0.242	0	0.253	0.390	0.473	0.489
0.484	0.457	0.379	0.240	0	0.253	0.388	0.465
0.470	0.483	0.462	0.375	0.240	0	0.250	0.394
0.382	0.467	0.487	0.468	0.382	0.239	0	0.255
0.246	0.384	0.460	0.486	0.450	0.374	0.238	0

(b)

Figure 5.12: Offered load: 1.2 Erlangs/connection
Failure probability (a) with WCC, (b) without WCC

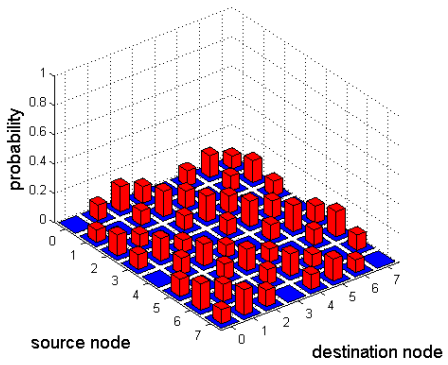

$p_{failure} - p_{block}$ (red bars)

$$\begin{bmatrix} 0 & 0.104 & 0.170 & 0.112 & 0 & 0.104 & 0.149 & 0.087 \\ 0.085 & 0 & 0.097 & 0.172 & 0.117 & 0 & 0.101 & 0.148 \\ 0.143 & 0.086 & 0 & 0.097 & 0.175 & 0.118 & 0 & 0.101 \\ 0.101 & 0.152 & 0.082 & 0 & 0.102 & 0.173 & 0.117 & 0 \\ 0 & 0.111 & 0.148 & 0.082 & 0 & 0.105 & 0.178 & 0.116 \\ 0.119 & 0 & 0.104 & 0.147 & 0.090 & 0 & 0.104 & 0.172 \\ 0.180 & 0.118 & 0 & 0.102 & 0.150 & 0.087 & 0 & 0.104 \\ 0.097 & 0.173 & 0.112 & 0 & 0.101 & 0.150 & 0.085 & 0 \end{bmatrix}$$

Figure 5.13: Failure probability with WCC, offered load 0.1 Erlangs/connection, physical layer blocking by static BER.

For the cases where physical layer blocking was not considered, the system behaviour with and without the WCC, is shown in Figure 5.12. As can be seen in Figure 5.12b, without the WCC, longer paths have a lower failure probability at the expense shorter paths. However, a key difference to the results in section 5.5.1 is that in the case where the WCC was imposed, the overall average failure probability was 0.364, and without the WCC was 0.382. In this particular topology, the WCC actually reduces the overall failure probability in the absence of physical layer blocking. This is because it is more difficult for connections requiring long paths to obtain a path that satisfies the WCC. As a result, these connections are blocked, meaning that there are many more wavelengths available to connections that require only short paths.

When the physical layer blocking was considered, it was found that there were significant numbers of connections that did not meet the minimum BER threshold of 10^{-12}. In this particular case, the offered load was extremely low, so there were no instances of blocking due to lack of wavelengths.

It was previously shown that the static BER for a 4 link path between opposing nodes did not exceed the minimum BER threshold, so the result in Figure 5.13 was intriguing. A deeper investigation of the simulation setup revealed that this was a result of the implementation of the naïve "first fit" path allocation algorithm.

Figure 5.14a shows the network in a state where a connection already exists from node 0 to node 7 using the red wavelength. Consider the case where a new connection requests a path from node 0 to node 6. In this case, because the red wavelength from node 0 to node 7 is already in use, the path between node 0 and node 6, using the *first available* wavelength (red), must traverse the links shown in Figure 5.14b. This is a valid path according to the RWA algorithm, but when the physical layer blocking check is applied, the path BER is found to exceed the minimum BER threshold and the connection attempt is prematurely marked as "blocked due to physical layer". To overcome this, the path allocation algorithm should attempt to allocate a new path using the next available wavelength if the BER of the currently allocated wavelength is unacceptable. In this example, when the connection from node 0 to node 6 using the red wavelength exceeds the BER threshold, a new attempt is made on the next available (e.g. blue) wavelength that gives an acceptable path BER, shown in Figure 5.14c.

Applying this modification to the path allocation algorithm in the simulation eliminated virtually all instances of physical layer blocking at low offered loads. At higher offered loads (e.g. 1.2 Erlangs/connection) such as in Figure 5.15, even the improved RWA algorithm can sometimes find paths that have unacceptably high BER, reflected in the red bars. This is due to the higher occupancy of feasible wavelengths by the higher volume of offered traffic.

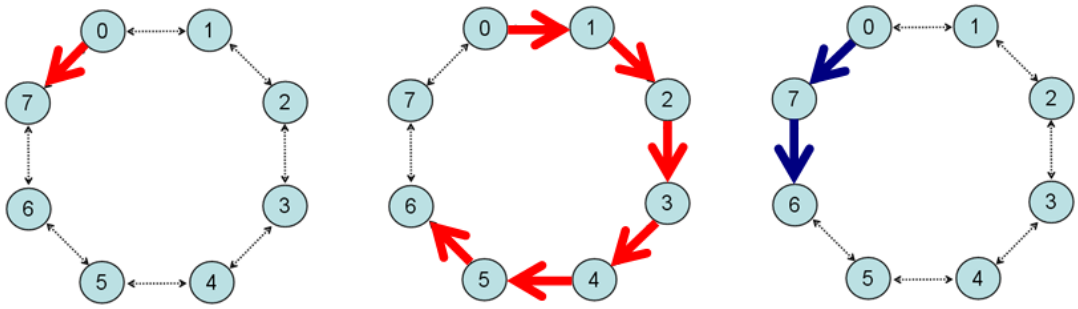

Figure 5.14: Effect of route allocation on naïve implementation of the "first fit" RWA algorithm.

Interestingly, the average failure probability across all connections was 0.355, of which 0.347 was due to wavelength availability and 0.008 was due to physical layer blocking. This was actually less than in the case where physical layer blocking was not considered. When physical layer blocking is not imposed, more connections using long paths with unacceptable BER would be admitted to the network, occupying more wavelengths and increasing the failure probability of connections using shorter paths. When physical layer blocking is imposed, these long paths would be rejected due to unacceptable BERs, freeing those wavelengths for more, shorter path connections.

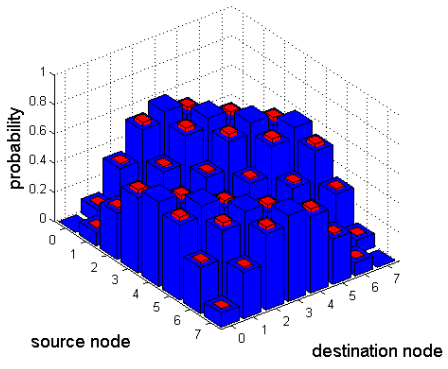

p_{block} (blue bars)

$$\begin{bmatrix}
0 & 0.096 & 0.318 & 0.524 & 0.589 & 0.511 & 0.316 & 0.094 \\
0.091 & 0 & 0.095 & 0.329 & 0.517 & 0.579 & 0.511 & 0.319 \\
0.316 & 0.092 & 0 & 0.088 & 0.324 & 0.510 & 0.581 & 0.507 \\
0.515 & 0.311 & 0.089 & 0 & 0.093 & 0.316 & 0.513 & 0.584 \\
0.578 & 0.510 & 0.317 & 0.091 & 0 & 0.089 & 0.321 & 0.513 \\
0.513 & 0.585 & 0.512 & 0.323 & 0.093 & 0 & 0.093 & 0.313 \\
0.315 & 0.506 & 0.580 & 0.517 & 0.310 & 0.088 & 0 & 0.092 \\
0.096 & 0.315 & 0.519 & 0.587 & 0.523 & 0.310 & 0.087 & 0
\end{bmatrix}$$

$p_{failure} - p_{block}$ (red bars)

$$\begin{bmatrix}
0 & 0.001 & 0.006 & 0.021 & 0 & 0.021 & 0.008 & 0.002 \\
0.002 & 0 & 0.001 & 0.007 & 0.023 & 0 & 0.022 & 0.008 \\
0.007 & 0.001 & 0 & 0.001 & 0.006 & 0.023 & 0 & 0.021 \\
0.022 & 0.006 & 0.001 & 0 & 0.001 & 0.006 & 0.022 & 0 \\
0 & 0.022 & 0.007 & 0.001 & 0 & 0.001 & 0.007 & 0.021 \\
0.022 & 0 & 0.020 & 0.006 & 0.001 & 0 & 0.002 & 0.007 \\
0.008 & 0.025 & 0 & 0.022 & 0.007 & 0.001 & 0 & 0.001 \\
0.001 & 0.006 & 0.018 & 0 & 0.021 & 0.006 & 0.001 & 0
\end{bmatrix}$$

Figure 5.15: Failure probability with WCC, offered load 1.2 Erlangs/connection, physical layer blocking by static BER, with modified "first fit" RWA algorithm

5.5.3 GRID TOPOLOGY

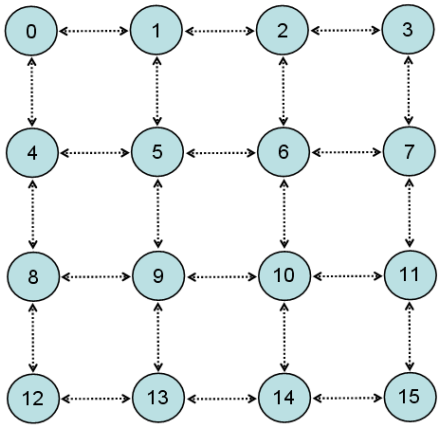

Figure 5.16: 16 node grid topology network

The third network topology examined using the MCMC simulation was a 16 node grid topology, shown in Figure 5.16. The link parameters were the same as in the previous simulations, taken from Table 5.3. Simulations were initially run without physical layer blocking, but with and without the WCC, to verify that the simulation behaviour was consistent with theory. These results are shown in Figure 5.17 and Figure 5.18.

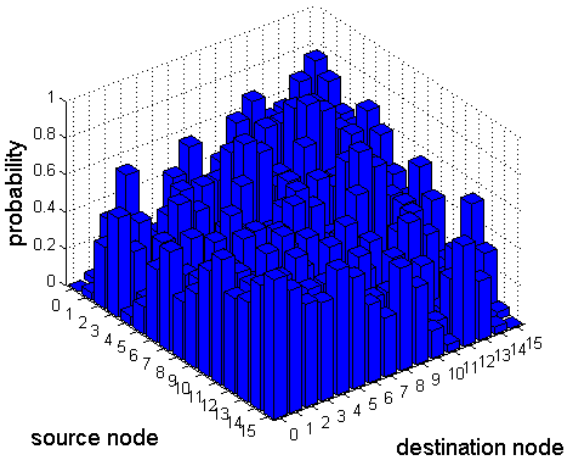

$p_{failure} = p_{block}$ (blue bars)

0	0.04	0.32	0.53	0.04	0.16	0.42	0.56	0.31	0.41	0.59	0.67	0.54	0.56	0.68	0.76
0.04	0	0.11	0.32	0.11	0.05	0.24	0.39	0.39	0.33	0.48	0.57	0.57	0.51	0.60	0.69
0.33	0.11	0	0.04	0.37	0.23	0.05	0.12	0.58	0.49	0.33	0.37	0.69	0.59	0.53	0.56
0.54	0.32	0.04	0	0.55	0.41	0.14	0.04	0.68	0.60	0.38	0.33	0.76	0.69	0.56	0.54
0.05	0.11	0.38	0.56	0	0.05	0.32	0.53	0.11	0.22	0.45	0.61	0.31	0.38	0.58	0.67
0.15	0.04	0.23	0.42	0.04	0	0.12	0.33	0.22	0.12	0.32	0.47	0.41	0.33	0.48	0.59
0.40	0.22	0.05	0.15	0.34	0.13	0	0.03	0.47	0.32	0.11	0.22	0.59	0.46	0.33	0.42
0.54	0.38	0.11	0.04	0.53	0.33	0.04	0	0.60	0.49	0.22	0.12	0.68	0.57	0.38	0.34
0.32	0.40	0.57	0.68	0.11	0.23	0.49	0.61	0	0.05	0.33	0.53	0.04	0.11	0.38	0.55
0.41	0.33	0.49	0.60	0.24	0.12	0.32	0.47	0.05	0	0.13	0.32	0.12	0.04	0.23	0.42
0.58	0.47	0.32	0.42	0.47	0.32	0.11	0.24	0.34	0.11	0	0.05	0.39	0.23	0.04	0.14
0.68	0.58	0.37	0.34	0.61	0.47	0.22	0.11	0.52	0.32	0.04	0	0.54	0.39	0.12	0.04
0.52	0.56	0.69	0.75	0.32	0.40	0.60	0.68	0.03	0.13	0.41	0.56	0	0.04	0.32	0.54
0.54	0.53	0.61	0.68	0.39	0.35	0.48	0.56	0.10	0.05	0.24	0.38	0.03	0	0.11	0.31
0.68	0.59	0.52	0.56	0.56	0.48	0.33	0.38	0.38	0.24	0.04	0.12	0.32	0.12	0	0.04
0.76	0.67	0.56	0.53	0.68	0.60	0.42	0.32	0.56	0.42	0.15	0.04	0.55	0.32	0.04	0

Average $p_{block} = 0.3597$

Figure 5.17: Failure probabilities for grid topology with WCC, offered load 0.65 Erlangs/connection.

The traffic matrix and plot show that the blocking probability is proportional to the connection path length. This is a direct consequence of the WCC, as it is more difficult to allocate long wavelength continuous paths as opposed to short ones.

Figure 5.18 shows the traffic matrix and blocking probability plot for the case where the WCC is not imposed. Consistent with previous behaviour and theory, connections with longer paths have a much reduced blocking probability (~0.27 less for the furthest nodes) at the expense of higher blocking probability for shorter path connections (~0.1 more for connections between adjacent nodes).

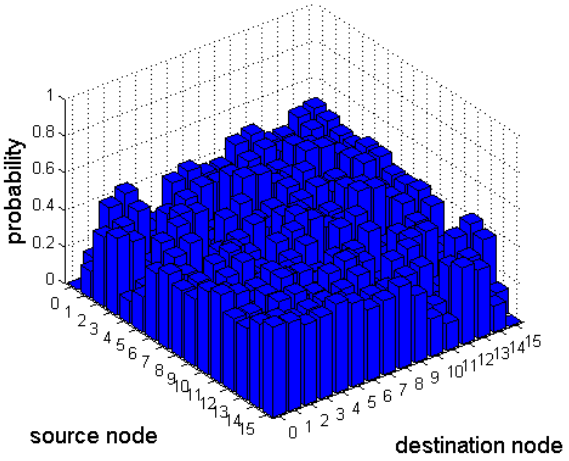

$p_{failure} = p_{block}$ (blue bars)

0	0.14	0.38	0.42	0.12	0.21	0.38	0.41	0.36	0.36	0.46	0.48	0.40	0.40	0.48	0.49
0.14	0	0.32	0.37	0.18	0.16	0.34	0.37	0.36	0.35	0.41	0.45	0.40	0.40	0.45	0.47
0.38	0.32	0	0.14	0.37	0.32	0.18	0.19	0.45	0.41	0.36	0.38	0.48	0.44	0.41	0.43
0.42	0.37	0.14	0	0.42	0.39	0.21	0.15	0.48	0.47	0.39	0.39	0.50	0.48	0.42	0.42
0.12	0.16	0.37	0.43	0	0.15	0.37	0.42	0.30	0.33	0.41	0.46	0.35	0.36	0.44	0.46
0.19	0.16	0.34	0.38	0.16	0	0.30	0.35	0.31	0.30	0.39	0.43	0.37	0.35	0.46	0.46
0.37	0.33	0.15	0.20	0.35	0.31	0	0.15	0.41	0.41	0.33	0.34	0.43	0.41	0.37	0.40
0.41	0.37	0.20	0.15	0.41	0.35	0.18	0	0.46	0.41	0.33	0.33	0.46	0.44	0.36	0.40
0.37	0.37	0.44	0.47	0.31	0.32	0.42	0.45	0	0.15	0.37	0.41	0.12	0.19	0.37	0.41
0.36	0.34	0.42	0.46	0.32	0.28	0.38	0.43	0.16	0	0.30	0.37	0.20	0.16	0.32	0.38
0.45	0.41	0.36	0.37	0.43	0.40	0.33	0.32	0.37	0.32	0	0.15	0.37	0.32	0.15	0.21
0.48	0.45	0.38	0.38	0.44	0.43	0.35	0.33	0.41	0.36	0.16	0	0.39	0.40	0.20	0.15
0.40	0.39	0.46	0.52	0.37	0.37	0.44	0.48	0.14	0.20	0.38	0.41	0	0.15	0.37	0.42
0.39	0.39	0.47	0.48	0.35	0.36	0.40	0.45	0.16	0.15	0.34	0.36	0.14	0	0.31	0.38
0.46	0.45	0.42	0.44	0.45	0.42	0.36	0.38	0.39	0.33	0.16	0.20	0.38	0.32	0	0.13
0.49	0.48	0.44	0.44	0.48	0.45	0.39	0.40	0.44	0.36	0.20	0.14	0.42	0.37	0.14	0

Average $p_{block} = 0.3490$

Figure 5.18: Failure probabilities for grid topology without WCC, offered load 0.65 Erlangs/connection.

The average blocking probability for all source-destination pairs is also reduced in the case where the WCC does not need to be satisfied from 0.3597 to 0.3490. Physical layer blocking was introduced in the system, using either the static BER or the dynamic outage probability.

In this topology, the shortest path between the two furthest nodes (e.g. 0 and 15, 3 and 12) is comprised of 6 links. For a BER threshold of 10^{-12}, the best case static BER (with no crosstalk from other channels) for a six-link path is 5.3×10^{-9}, while the worst case static BER is 5.7×10^{-8} which both exceed the minimum BER threshold. The best and worst case calculated outage probability were both 1.00. This

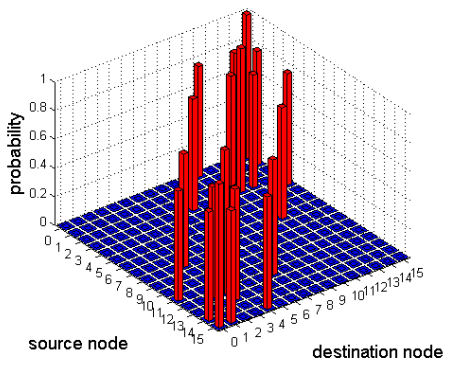

$p_{failure}$ (combined blue and red bars)

Source Node	Destination Node	Failure Probability
0	11	0.77
0	14	0.76
0	15	1
15	1	0.78
12	2	0.77
8	3	0.79
12	3	1
13	3	0.77
15	4	0.78
12	7	0.80
8	3	0.78
11	0	0.77
12	2	0.76
12	3	1
12	7	0.77
13	3	0.78
14	0	0.77
15	0	1
15	1	0.79

Figure 5.19: Failure probabilities for grid topology with WCC, offered load 0.10 Erlangs/S-D pair and physical layer blocking by static BER.

indicates that it should not be possible for any connections to be made between the furthest separated source-destination pairs when physical layer blocking is taken into account, regardless of the traffic loading in the network.

For the five-link paths between slightly closer nodes (e.g. 0 and 11, 0 and 14 etc), the corresponding best and worst case static BER is 5.7×10^{-13} and 1.4×10^{-10} and the best and worst case outage probabilities are 0.1308 and 1.00. This means that connections between these sets of nodes should be blocked by the physical layer some of the time, dependent on the level of inter-channel crosstalk interfering with the connection path.

In order to verify these calculations, the simulation was run using the static BER for physical layer blocking with minimal traffic (0.1 Erlangs/S-D pair), with results shown in Figure 5.19. In this case the usual traffic matrix was very sparse, so the failure probabilities were presented in table form for easier readability. The low offered load ensured there would be no wavelength blocking, (which was verified by checking the blocking probability matrix) so that the failure probability was entirely attributable to physical layer outage. It can be seen that for connections between the furthest nodes, it was impossible to find a connection that satisfied the minimum

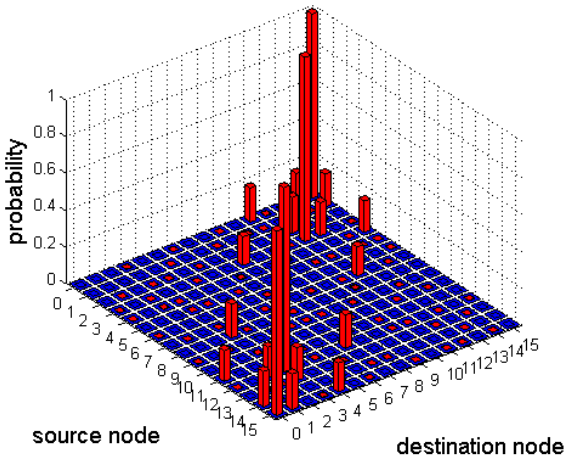

$p_{failure}$ (combined blue and red bars)

0	0	0	2.4E-03	0	0	9.8E-04	0	0	4.7E-04	0	0.19	2.8E-03	0	0.17	1
0	0	0	0	0	4.5E-04	0	0	9.5E-04	0	5.2E-03	0	0	7.6E-03	0	0.18
0	4.8E-04	0	4.7E-04	9.9E-04	0	4.8E-04	0	0	1.9E-03	0	9.2E-04	1.9E-01	0	4.6E-03	0
1.4E-03	0	0	0	0	1.4E-03	0	0	0.16	0	2.3E-03	0	1	0.18	0	2.9E-03
4.8E-04	0	1.9E-03	0	0	0	0	4.4E-03	0	0	3.7E-03	0	0	0	0	0.17
0	0	0	9.6E-04	4.8E-04	0	4.8E-04	0	0	4.7E-04	0	2.4E-03	9.2E-04	0	1.9E-03	0
1.4E-03	0	0	0	0	4.8E-04	0	4.8E-04	2.3E-03	0	0	0	0	3.3E-03	0	1.4E-03
0	4.6E-04	0	9.8E-04	5.5E-03	0	0	0	0	2.9E-03	0	4.8E-04	0.16	0	1.4E-03	0
0	0	0	0.18	1.4E-03	0	1.5E-03	0	0	0	0	4.8E-03	0	0	0	0
9.3E-04	0	2.3E-03	0	0	0	0	1.4E-03	0	0	1.9E-03	0	0	9.2E-04	0	0
0	1.4E-03	0	2.0E-03	3.3E-03	0	0	0	0	0	0	0	9.8E-04	0	1.5E-03	0
0.17	0	0	0	0	3.3E-03	0	0	4.1E-03	0	4.7E-04	0	0	0	0	0
9.2E-04	0	0.17	1	0	1.5E-03	0	0.18	0	0	4.8E-04	0	0	4.6E-04	0	1.4E-03
0	5.3E-03	0	0.18	0	0	2.9E-03	0	0	0	0	0	0	0	4.6E-04	0
0.19	0	4.6E-03	0	0	2.4E-03	0	4.7E-04	4.7E-04	0	0	0	0	0	0	0
1	0.19	0	3.2E-03	0.15	0	1.4E-03	0	0	9.4E-04	0	4.7E-04	1.9E-03	0	4.9E-04	0

Figure 5.20: Failure probabilities for grid topology with WCC, offered load 0.10 Erlangs/S-D pair and physical layer blocking by outage probability.

BER requirement of 10^{-12}. It was found that for those connections between nodes that were a minimum of 5 links apart, that the failure probability was approximately 0.75-0.80. This is because the best case BER of these connections, when there are no inter-channel crosstalk interferers, does not exceed the threshold, but in instances where the network becomes more loaded, the inter-channel crosstalk causes the BER to exceed the threshold.

Figure 5.20 shows the result of the simulation where the outage probability was used as the physical layer blocking mechanism. There are some interesting features compared Figure 5.19, the most clear being that the connection failure probability for the minimum five-link path node pairs is much less than in Figure 5.19. This is

because the outage probability accounts for the time-varying nature of the path ASE, RCD and PMD – at some times the BER will exceed the threshold, while at other times will be below it. In this particular network topology, it happens that the static BER for the connections with minimum five-link path is close the BER threshold.

Another interesting feature in Figure 5.20 is that there are many small, non-zero entries in the failure probability matrix. Closer inspection of the results revealed that many connections between "close" nodes (e.g. nodes 0 to 3) were made via paths of greater than the minimum number of required links. This was possible because of the highly connected nature of the grid topology – nodes in the centre of the grid have four possible egress links, edge nodes have three while corner nodes still have two. As the network load increases, longer, more circuitous paths need to be allocated to satisfy the WCC. The static BER of these paths came close to the BER threshold, but did not exceed it in Figure 5.19, but the outage probability of these paths was small, but non-zero, as seen in Figure 5.20.

To verify this effect, the offered load was increased to 0.65 Erlangs/S-D pair, with results shown in Figure 5.21. Here, it becomes apparent that the physical layer blocking is a significant factor in the grid topology – while more paths can be found that satisfy the WCC, these paths do not necessarily meet physical layer requirements.

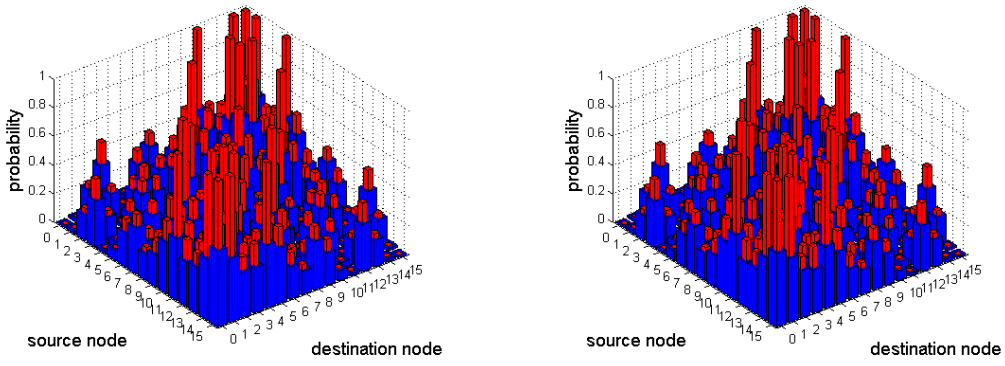

(a) (b)

Figure 5.21: Failure probabilities with WCC, offered load 0.65 Erlangs/S-D pair, physical layer blocking by (a) static BER, (b) outage probability

5.5.4 AUSTRALIA TOPOLOGY

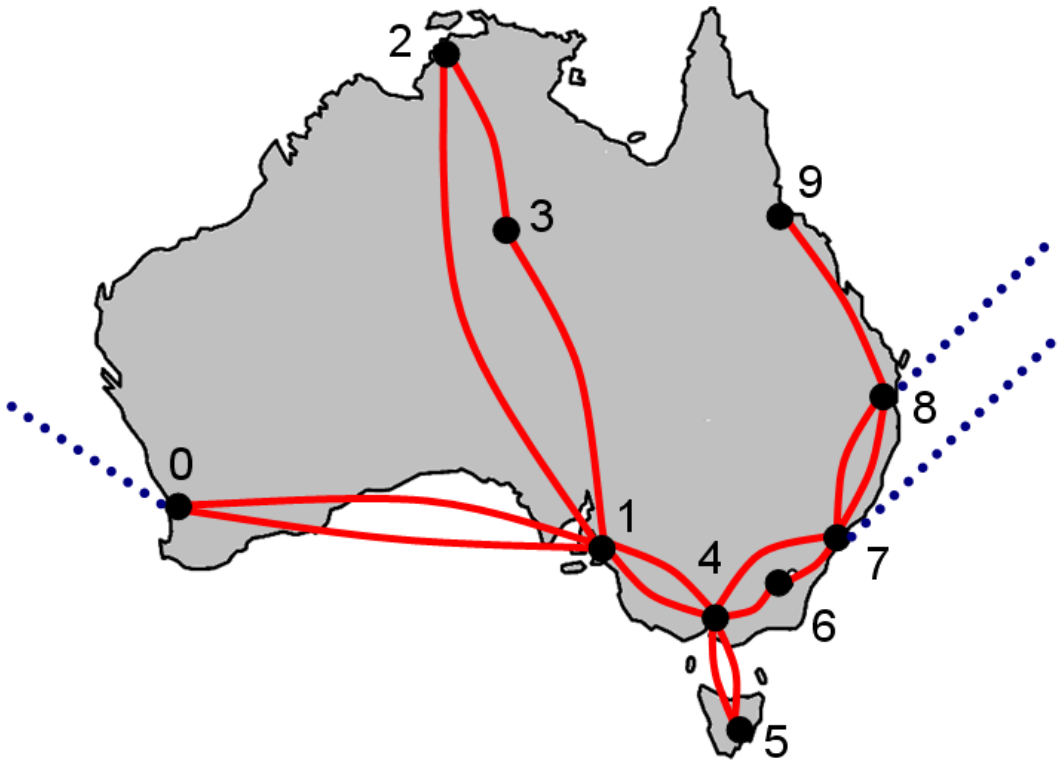

Figure 5.22: 10 node Australian network topology

In this section, a hypothetical network topology based on Australia's Academic and Research Network (AARNet) topology [139] was used as input for the developed failure probability simulation and is shown in Figure 5.22. In this diagram, the solid red lines represent 10 Gbit/sec NRZ links, while the dotted blue lines represent international links egressing Australia from nodes 0, 7 and 8. Note that the international links are not a part of the simulation, and are shown only to emphasise the key Australian international gateway nodes. The distance between the cities represented by the nodes was used as the physical link length.

The simulation parameters that were different from sections 5.5.1-5.5.3 are summarised in Table 5.5. The BER threshold, 10^{-3}, was chosen with the assumption that end to end connections employ forward error correction (FEC) [93].

Table 5.5: Simulation parameters for Australia topology

Parameter	Value
Uncompensated dispersion per 80km span	10 ps/nm
EDFA Noise Figure	5 dB
Fibre PMD	0.1 ps/km$^{0.5}$
BER threshold	10^{-3}

A traffic matrix was constructed using population statistics for Australia [140], and the simple assumptions that:

- The quantities of connection requests are proportional to city population.
- Two thirds of connection requests are to international destinations. One third through Brisbane (node 8) and one third through Sydney (node 7). Perth (node 0) uses its own international link for all international connections.
- The remaining third of connection requests are to domestic destinations. The number of connection requests to a particular destination is proportional to the destination city population.

The connection arrival rates for all source-destination pairs were then normalised to the (maximum) Melbourne to Sydney connection arrival rate as shown in Table 5.6. To ensure that some wavelength blocking and physical layer outage could be observed, the connection departure rates were then set to be identical and varied, so that the offered load to the network was varied in proportion to the original traffic matrix. For example, when connection departure rates are set to 1 connection/unit time, the offered load is defined by the traffic matrix in Table 5.6. If the departure rates are all set to 0.5 or 0.25 connections/unit time, then the offered load would be defined by the original traffic matrix scaled by a factor of 2 or 4 respectively.

Table 5.6: Traffic loading matrix ratios for Australia topology

	Dest Node	0	1	2	3	4	5	6	7	8	9
Source Node	City	Perth	Adelaide	Darwin	Alice Springs	Melbourne	Hobart	Canberra	Sydney	Brisbane	Cairns
0	Perth	0	0.0265	0.0027	0.0005	0.0880	0.0047	0.0078	0.0995	0.0440	0.0022
1	Adelaide	0.0265	0	0.0020	0.0004	0.0644	0.0035	0.0057	0.3011	0.2605	0.0016
2	Darwin	0.0027	0.0020	0	4.1E-05	0.0066	0.0004	0.0006	0.0310	0.0268	0.0002
3	Alice Springs	0.0005	0.0004	4.1E-05	0	0.0013	0.0001	0.0001	0.0061	0.0053	3.3E-05
4	Melbourne	0.0880	0.0644	0.0066	0.0013	0	0.0115	0.0190	1	0.8652	0.0054
5	Hobart	0.0047	0.0035	0.0004	0.0001	0.0115	0	0.0010	0.0538	0.0465	0.0003
6	Canberra	0.0078	0.0057	0.0006	0.0001	0.0190	0.0010	0	0.0887	0.0767	0.0005
7	Sydney	0.0995	0.0728	0.0075	0.0015	0.2416	0.0130	0.0214	0	0.9780	0.0061
8	Brisbane	0.0440	0.0322	0.0033	0.0007	0.1068	0.0057	0.0095	0.4999	0	0.0027
9	Cairns	0.0022	0.0016	0.0002	3.3E-05	0.0054	0.0003	0.0005	0.0253	0.0219	0

It was found that the original traffic matrix needed to be scaled by a factor of 5 for observable effects. The simulation was run using the static BER and outage probability as the physical layer blocking mechanism, with the results shown in Figure 5.23 and Figure 5.24.

This topology is a good example of a network that would function adequately with optical regeneration at each node, but would encounter problems when migrated to an all-optical architecture. Figure 5.23 shows significant physical layer blocking for connections to and from nodes 0 and 2 (Perth and Darwin) due to the extended physical length of all-optical paths to nodes that are separated by more than one link. The reason that the instances of physical layer blocking do not bring the failure probabilities to one is because the levels of inter-channel crosstalk observed by incoming connections vary with the instantaneous network loading. This means that when the network is lightly loaded, connections that satisfy the physical layer constraints can be established more often.

Figure 5.24 gives an overall impression of how the network would perform across an extended period of time. This is because outage probability metric captures probabilistically the time-varying nature of the physical layer impairments with the link impairments characterised by mean values. In contrast, the results in Figure 5.23 show how the network would perform if the link impairments were characterised by instantaneous values.

While the results in Figure 5.23 show which pairs of nodes will have difficulty meeting the BER requirement for the link values at the instant the network is defined, Figure 5.24 gives a more detailed analysis that includes the time-varying nature of the physical layer impairments. For instance, while Figure 5.23 shows that there is no physical layer blocking between nodes 0 and 4 (Perth and Melbourne), Figure 5.24 detects that over an extended time scale, some physical layer blocking does actually occur when time-varying impairment values happen to cause the BER to exceed 10^{-12}. Conversely, Figure 5.23 shows that for connections between nodes 0 and 7 (Perth and Sydney), there is significant (~0.60) physical layer blocking, but Figure 5.24 shows this to be much less significant (~0.06) when factoring in longer time scales.

This additional information available to network operators can assist in more cost effective decision making in deciding where and when to upgrade capacity or to install optical regeneration.

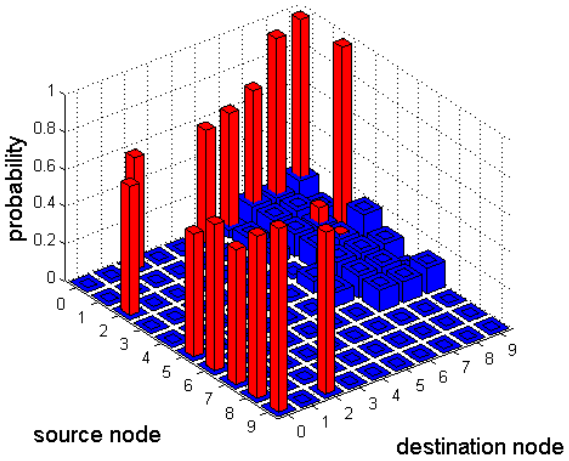

p_{block} (blue bars)

0	0	0	0	0	0	0.04	0.12	0.11	0.16
0	0	0	0	0	0	0.07	0.12	0.12	0.08
0	0	0	0	0	0	0.06	0.12	0.11	0
0	0	0	0	0	0	0	0.12	0.12	0.20
0	0	0	0	0	0	0.06	0.12	0.12	0.12
0	0	0	0	0	0	0.08	0.12	0.12	0.04
0	0	0	0	0	0	0	0.12	0.11	0.14
0	0	0	0	0	0	0	0	0	0
0	0	0	0	0	0	0	0	0	0
0	0	0	0	0	0	0	0	0	0

$p_{failure} - p_{block}$ (red bars)

0	0	0.60	0	0	0.60	0.60	0.60	0.83	0.84
0	0	0	0	0	0	0	0	0	0
0.69	0	0	0	0	0	0	0	0.08	1
0	0	0	0	0	0	0	0	2.2E-3	0
0	0	0	0	0	0	0	0	0	0
0.66	0	0	0	0	0	0	0	0	0
0.78	0	0	0	0	0	0	0	0	0
0.72	0	0	0	0	0	0	0	0	0
0.87	0	0	0	0	0	0	0	0	0
0.98	0	0.87	0	0	0	0	0	0	0

$p_{failure}$ (combined blue and red bars)

0	0	0.60	0	0	0.60	0.64	0.72	0.95	1.00
0	0	0	0	0	0	0.07	0.12	0.12	0.08
0.69	0	0	0	0	0	0.06	0.12	0.19	1
0	0	0	0	0	0	0	0.12	0.12	0.20
0	0	0	0	0	0	0.06	0.12	0.12	0.12
0.66	0	0	0	0	0	0.08	0.12	0.12	0.04
0.78	0	0	0	0	0	0	0.12	0.11	0.14
0.72	0	0	0	0	0	0	0	0	0
0.87	0	0	0	0	0	0	0	0	0
0.98	0	0.87	0	0	0	0	0	0	0

Average $p_{failure} = 0.1488$

Figure 5.23: Failure probability with WCC, scaled maximum offered load of 5 Erlangs/S-D pair, physical layer blocking by static BER.

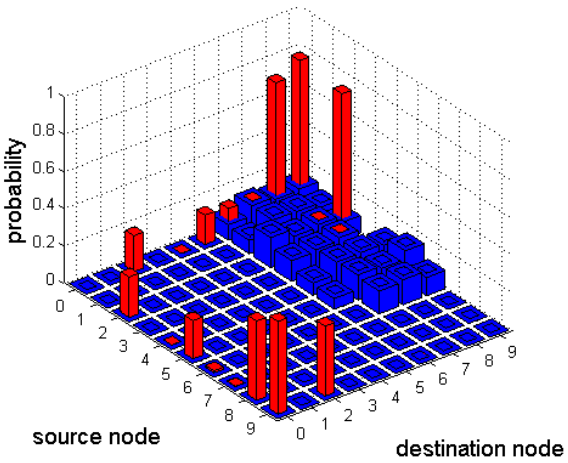

p_{block} (blue bars)

0	0	0	0	0	0	0.08	0.13	0.12	0.13
0	0	0	0	0	0	0.07	0.13	0.13	0.10
0	0	0	0	0	0	0.16	0.12	0.13	0.10
0	0	0	0	0	0	0.11	0.12	0.14	0
0	0	0	0	0	0	0.07	0.13	0.13	0.12
0	0	0	0	0	0	0.06	0.13	0.12	0.17
0	0	0	0	0	0	0	0.12	0.13	0.10
0	0	0	0	0	0	0	0	0	0
0	0	0	0	0	0	0	0	0	0
0	0	0	0	0	0	0	0	0	0

$p_{failure} - p_{block}$ (red bars)

0	0	0.19	0	2.5E-04	0.16	0.06	1.2E-03	0.60	0.66
0	0	0	0	0	0	0	0	0	0
0.22	0	0	0	0	0	0	0	4.1E-04	0.67
0	0	0	0	0	0	0	0	2.0E-03	0
2.4E-04	0	0	0	0	0	0	0	0	0
0.21	0	0	0	0	0	0	0	0	0
0.01	0	0	0	0	0	0	0	0	0
1.2E-03	0	0	0	0	0	0	0	0	0
0.43	0	0	0	0	0	0	0	0	0
0.50	0	0.38	0	0	0	0	0	0	0

$p_{failure}$ (combined blue and red bars)

0	0	0.19	0	2.5E-04	0.16	0.14	0.14	0.72	0.79
0	0	0	0	0	0	0.07	0.13	0.13	0.10
0.22	0	0	0	0	0	0.16	0.12	0.13	0.76
0	0	0	0	0	0	0.11	0.12	0.14	0
2.4E-04	0	0	0	0	0	0.07	0.13	0.13	0.12
0.21	0	0	0	0	0	0.06	0.13	0.12	0.17
0.01	0	0	0	0	0	0	0.12	0.13	0.10
1.2E-03	0	0	0	0	0	0	0	0	0
0.43	0	0	0	0	0	0	0	0	0
0.50	0	0.38	0	0	0	0	0	0	0

Average $p_{failure} = 0.0793$

Figure 5.24: Failure probability with WCC, scaled maximum offered load of 5 Erlangs/S-D pair, physical layer blocking by outage probability.

5.6 SUMMARY, DISCUSSION & CONCLUSIONS

5.6.1 SUMMARY

In this chapter, techniques were used from the field of queuing theory and teletraffic engineering to evaluate the combined effect of wavelength and physical layer blocking from multiple dynamic optical impairments in all-optical networks. An overview of basic Markov chain theory was presented.

For small networks it was shown how this could be achieved analytically using the outage probability metric developed in chapter 4 and a restricted accessibility Markov Chain system. For more complex networks a generalised Markov Chain Monte Carlo (MCMC) simulation framework was required and developed. This simulation enabled cross verification of results with the analytic technique in smaller networks, as well as evaluation of the failure probability in larger networks.

The simulation was then executed on different network topologies to demonstrate the different situations where either the outage probability or static BER computed from multiple optical impairments would be useful. It was shown that the developed signal quality metrics can give network operators additional useful information about the state of their network over longer time scales (for network dimensioning), as well as at any instant in time (for dynamic path allocation).

5.6.2 DISCUSSION

In this section, a number of key assumptions were made to simplify the analysis and development of the simulation. Firstly, identical probability mass functions (defined in section 4.3) were used for the optical impairments throughout the network to enable the computation of path outage probability. In real networks, links would have different impairment probability mass functions, so this would need to be accounted for, either by real time calculation, or extended lookup tables. There is also much scope for code optimisation, particularly in the computation of the outage probability, and searching of the outage probability lookup tables. The accuracy of the outage probability lookup tables could also be improved with more bins (see section 4.4.4) and smaller impairment increments.

Secondly, the effect of new connection arrivals on the signal quality of existing connections was not accounted for. This would not be difficult to implement – a matter of reassessing if existing connections exceed the BER threshold with increased inter-channel crosstalk, but was left out in the interests of reducing simulation execution time.

Finally, different RWA algorithms were not investigated. As the purpose of this chapter was to highlight the applications of the developed metrics in chapters 3 and 4, only the simplest "first fit" algorithm was used in the simulation.

5.6.3 CONCLUSIONS

A number of contributions and conclusions were made in this chapter, listed below.

- A method to analytically combine the physical layer outage probability from multiple optical impairments, with the wavelength blocking probability in single link and simple networks.
- Development of a generalised Markov Chain Monte Carlo simulation framework that accounts for wavelength blocking, physical layer signal quality interaction between channels via inter-channel crosstalk and multiple time varying physical layer impairments.
- Insight into the effect of multiple time-varying physical layer impairments in comparison with static impairments on various standard network topologies as well as a hypothetical topology based on the AARNet network.

The next chapter concludes the thesis and outlines possible future work that could be conducted based on this work.

6

Conclusions, Future Work

6.1 CONCLUSIONS

This work contributes to the field of network management in next generation intelligent all-optical networks. The main focus of this thesis is the development of a method, demonstrated by computer simulation, to accurately combine the effects on signal quality of multiple physical layer impairments on 10 Gbit/sec NRZ modulated signals. The distinguishing feature of this work is that a quantitative analysis of the accuracy of the method has been conducted using an accurate commercially deployed optical system simulation package (VPI WDMTransmissionMaker), giving excellent results particularly for linear impairments. The secondary objective of this work is to demonstrate applications of the developed method in the computation of connection outage probability and combined traffic and physical layer blocking probability in all optical networks.

This work is important because of the emergence of intelligent all-optical networks in which physical layer impairments become limiting factors in path selection. Path selection algorithms using multiple routing metrics are computationally complex, while a single routing metric encompassing all effects is much more implementable within in existing standards.

The combined effect of multiple optical impairments was calculated using known relationships between optical impairments and the signal degradation metric; the Eye Closure Penalty (ECP). A relationship was then derived between the ECP and the well known Q-factor signal quality metric which is related to the Bit Error Rate (BER) experienced by a connection subjected to optical impairments.

It was found that while the ECP value calculated from different impairments may have the same numerical value, their effect on the Q-factor was not identical. The

"Ideal ECP" quantity that was developed to account for this involves using the measured Q-factors and equation (3.19). This signal quality estimation method captured the relative impacts of amplified spontaneous emission (ASE) from optical amplifiers, residual chromatic dispersion (RCD) and polarisation mode dispersion (PMD) accumulated in a signal travelling through optical fibre and showed excellent accuracy in predicting the actual Q-factor of 10, 40 and 100 Gbit/sec NRZ and 10 Gbit/sec DPSK modulated signals in the presence of these impairments.

The effects of intra-channel and inter-channel crosstalk, as well as non-linear impairments such as four-wave mixing (FWM) and self and cross phase modulation (SPM/XPM) were also considered for 10 Gbit/sec NRZ signals. Results from these experiments show that the developed method can estimate the effect of these degradations, though further work is required to more accurately model these mechanisms.

It is known that the effects of both RCD and SPM on signal quality are not independent. It was found in this work that ECP due to SPM and RCD could be jointly estimated using a two-dimensional curve-fit of transmitter power and RCD. It was also found that the dispersion map for the optical path needs to be taken into account. For impairments that are not independent, it is conjectured that a method such as this could be used to estimate the ECP for those impairments.

The Q-factor estimation method developed in this thesis was shown to be very accurate for the majority of impairments considered. Coupled with the emergence of ubiquitous optical performance monitoring, the method will be particularly useful in the context of automated path selection in all optical networks.

In chapter 3, the signal quality had only been applied to static (non-varying) impairment values. In real networks, where factors such as seasonal changes in ambient temperature, time varying performance in optical network elements, and fundamental physical mechanisms could cause variations in instantaneous measured impairment values. In such situations, the overall effects of physical layer impairments are evaluated in terms of the "outage probability" – the probability that impairments exceeded a certain threshold value. Prior work in this area relates

mainly to PMD and to a lesser extent RCD and polarisation dependent loss (PDL). Chapter 4 showed how to extend the developed Q-factor estimation method to enable the calculation of the outage probability from multiple simultaneous time-varying optical impairments, an achievement not previously accomplished.

Using data provided by optical performance monitors, impairment histograms corresponding to probability mass functions (PMF) can be constructed. It was shown that these PMFs can be combined, using methods presented in this thesis, into a single PMF of the BER. The outage probability can then be determined as the sum of the BER probabilities in the PMF that exceed a specified BER threshold, e.g. 10^{-12} or 10^{-3} in systems using FEC. It was recognised that time-correlated impairments require special treatment and in such cases, joint histograms should be taken for any such time-correlated impairments. It was also found that values as small as 2 or 3 ps of DGD, or 2 to 3 ps/nm of RCD, can cause significant outage probability in high bit-rate systems, highlighting the need for dynamic PMD and RCD compensation and/or more robust advanced modulation formats.

The ability to accurately estimate the outage probability of paths in all-optical networks enables network operators to better gauge long term path sustainability and to offer better service level agreements with customers. Extending this, it was shown how the outage probability metric could be used to calculate the probability that an incoming connection would experience blocking due to lack of available resources (wavelengths) or an outage due to poor signal quality in the presence of time varying physical layer impairments. This probability was termed the "failure probability" in this work.

Using teletraffic engineering theory, it was shown that the failure probability could be exactly analytically calculated for single link, single trunk or very simple, small networks in the presence of the wavelength continuity constraint (WCC). For larger, more complex networks with dynamic route allocation, this becomes difficult, and evaluation of the failure probability will generally require computer simulation. This is because the physical layer impairments must be considered on a per-path basis but the allocation of traffic resources must be considered on a per-link basis.

Recognising this, a generalised Markov Chain Monte Carlo simulation was developed that accounted for the physical layer impairments of ASE, RCD, PMD and inter-channel crosstalk, as well as the wavelength continuity constraint. The simulation used a modified "first fit" routing and wavelength assignment (RWA) algorithm though any RWA algorithm could be used. The simulation could apply physical layer blocking using the BER calculated from static values of physical layer impairments, or using the outage probability calculated from time-varying impairment PMFs. The former method has very fast computation time and gives an accurate indication of path signal quality at the connection set up time, making it more suited to dynamic path selection. Conversely, computing the outage probability is more time consuming, but gives a longer term stochastic overview of network behaviour and so is more suited to network dimensioning.

Finally, simulations of combined traffic and physical layer blocking were conducted on a variety of standard network topologies (linear, ring, grid), as well as a hypothetical "Australia topology" based on the AARNet network. The outputs of these simulations demonstrated the usefulness of both the static BER and dynamic outage probability metrics calculated from multiple physical layer impairments, reinforcing the fact that these must be considered in next generation all-optical networks.

6.2 FUTURE WORK

The work presented in this thesis presents network operators with a simple, accurate technique of estimating the signal quality of connections through all-optical networks, enabling dynamic path selection as well as providing tools for longer term network analysis. The method could be readily used in its current form with linear network impairments using NRZ or DPSK modulation, but there are a number of areas that could be investigated further:

- Experimental validation of the techniques presented would be useful, although the main three impairments investigated (ASE, RCD, PMD) are very well understood in theory and simulations.

- First order PMD was studied in this thesis using the worst-case 45° polarisation angle. Future work could investigate higher order PMD and arbitrary polarisation angles.
- Non-linear effects are notoriously difficult to account for, their investigation in this thesis is very basic. Improving their relationships with the ECP and Q-factor could be the subject of future work.
- This work has been shown to be effective for NRZ and DPSK modulation formats, the former being the most widely used and the latter being a probable successor in next generation networks. Future work could further investigate the applicability of the method in DPSK and on more advanced modulation formats.
- The computation of outage probability could be much improved using faster convolution algorithms to combine the impairment probability mass functions, possibly removing the need for lookup tables in the generalised Markov Chain Monte Carlo simulation.
- The developed signal quality metric and simulation framework can aid in the development of new impairment aware dynamic routing algorithms and analytic impairment aware blocking probability techniques.

7 Supporting Publications and Bibliography

7.1 SUPPORTING PUBLICATIONS

The following supporting publications, directly involved with this thesis, were completed during the time taken to produce this work:

- J. C. Li, K. Hinton, S. D. Dods and P. M. Farrell, "Eye closure penalty based signal quality metric," *in preparation*.
- K. Hinton, J. C. Li, P. M. Farrell and W. V. Sorin, "A New Design Technique for Optical Links," to be presented at IEEE Photonics Society, 22nd Annual Meeting of, 2009.
- J. C. Li, K. Hinton, S. D. Dods and P. M. Farrell, "Optical impairment outage computation," in *Optics Express*, vol. 16, issue 14, pp. 10529-10534, 2008.
- J. C. Li, K. Hinton, S. D. Dods and P. M. Farrell, "Novel Outage Probability Based RWA Algorithm," presented at Optical Fiber Communication Conference, 2008 and the 2008 National Fiber Optic Engineers Conference, 2008.
- J. C. Li, K. Hinton, S. D. Dods, P. M. Farrell, M. Ivanovich and P. Fitzpatrick, "Outage and Capacity based Path Selection in Optical Networks," presented at Optical Communication, 2007. ECOC 2007. 33rd European Conference on, 2007.
- J. C. Li, K. Hinton, S. D. Dods and P. M. Farrell, "Enabling ASON Routing via Novel Signal Quality Metrics," presented at Optical Fiber Communication Conference, 2007 and the 2007 National Fiber Optic Engineers Conference, 2007.
- J. Li, K. Hinton, S. Dods and P. Farrell, "Automatically Switched Optical Network Path Selection Using Eye Closure Penalty," Australian Telecommunication Networks and Applications Conference, 2006.

The following publications, not directly involved with this thesis, were completed during the time taken to produce this work:

- T. B. Anderson, S. D. Dods, A. Kowalczyk, K. Clarke, D. Hewitt, J. C. Li, "Asynchronous Delay-Tap Sampling," in *Optical Performance Monitoring: Advanced Techniques for Next-Generation Photonic Networks,* eds C. Chan, Academic Press, 2010**.**
- T. Anderson, D. Beaman, J. C. Li, O. Jerphagnon, E. Le Rouzic, F. Neddam and S. Salaün, "Demonstration of Simultaneous OSNR and CD Monitoring using Asynchronous Delay Tap Sampling on an 800 km WDM Test Bed," to be presented at Optical Communication, 2009. ECOC 2009. 35th European Conference on, 2009.
- T. Anderson, J. C. Li, D. Hewitt and O. Jerphagnon, "Optical Performance Monitoring for Intelligent Networks," to be presented at Optical Communication, 2009. ECOC 2009. 35th European Conference on, 2009.
- T. B. Anderson, A. Kowalczyk, K. Clarke, S. D. Dods, D. Hewitt and J. C. Li, "Multi Impairment Monitoring for Optical Networks," accepted in *Journal of Lightwave Technology*, 2009.
- M. Ivanovich, P. Bickerdike, J. Li*, "On TCP Performance Enhancing Proxies in a Wireless Environment," *Communications Magazine*, *IEEE,* vol. 46, pp. 76-83, 2008. * acknowledged as first author.

7.2 BIBLIOGRAPHY

[1] K. Tse, "AT&T's Photonic Network," presented at OFC/NFOEC 2008, San Diego, 2008.

[2] B. Mukherjee, *Optical WDM Networks; Chapter 6.6*. New York: Springer Science+Business Media, Inc., 2006.

[3] R. Ramaswami and K. N. Sivarajan, *Optical Networks: A Practical Perspective; Chapter 1.* San Francisco: Morgan Kaufmann, 2002.

[4] ITU-T, Rec G.8080, "Architecture of the Automatic Switched Optical Network (ASON)," International Telecommunications Union, 2006.

[5] D. Brungard (Ed), "RFC4258: Requirements for Generalized MPLS (GMPLS) Routing for Automatically Switched Optical Network (ASON)," Internet Engineering Task Force, RFC4258, 2005. [Online] Available: http://www.ietf.org/rfc/rfc4258.txt. [Accessed Apr 15 2006].

[6] A. Jaiszczyk, "Automatically switched optical networks: benefits and requirements," *Communications Magazine, IEEE*, vol. 43, pp. S10-S15, 2005.

[7] G. Bernstein, B. Rajagopalan, D. Saha, *Optical Network Control: Architecture, Protocols & Standards; Chapter 11.* Boston: Addison-Wesley Longman Publishing Co., Inc., 2004.

[8] J. Strand, A. L. Chiu, and R. Tkach, "Issues for routing in the optical layer," *Communications Magazine, IEEE*, vol. 39, pp. 81-87, 2001.

[9] I. Tomkos, D. Vogiatzis, C. Mas, I. Zacharopoulos, A. Tzanakaki, and E. Varvarigos, "Performance engineering of metropolitan area optical networks through impairment constraint routing," *Communications Magazine, IEEE*, vol. 42, pp. S40-S47, 2004.

[10] S. Sygletos I. Tomkos and J. Leuthold, "Technological challenges on the road toward transparent networking," *Optical Network, Journal of*, vol. 7, pp. 321-350, 2008.

[11] T. H. Maiman, "Stimulated Optical Radiation in Ruby," *Nature*, vol. 187, pp. 493-494, 1960.

[12] F. P. Kapron, D. B. Keck, and R. D. Maurer, "Radiation Losses In Glass Optical Waveguides," *Applied Physics Letters*, vol. 17, pp. 423-425, 1970.

[13] I. Hayashi, M. B. Panish, P. W. Foy, and S. Sumski, "Junction Lasers Which Operate Continuously At Room Temperature," *Applied Physics Letters,* vol. 17, pp. 109-111, 1970.

[14] T. J. Xia *et al*, "Transmission of 107-Gb/s DQPSK over Verizon 504-km Commercial LambdaXtreme® Transport System", presented at OFC/NFOEC 2008, San Diego, 2008.

[15] I. P. Kaminow and T. Li, *Optical Fiber Telecommunications IV-A; Chapter 15*. San Diego: Academic Press, 2002.

[16] G. P. Agrawal, *Fiber-Optic Communications Systems, Third Edition; Chapter 1*. New York: John Wiley & Sons, Inc., 2002.

[17] T. E. Stern and K. Bala, *Multiwavelength Optical Networks*, Reading: Addison Wesley, 1999.

[18] K. M. Sivalingam and S. Subramaniam, Eds., *Optical WDM Networks: Principles and Practice.* Norwell: Kluwer Academic Publishers, 2000.

[19] B. Mukherjee, *Optical WDM Networks*. New York: Springer Science+Business Media, 2006.

[20] S. Poole, D. Payne, R. Mears, M. A.-F. Fermann, M., and R. A.-L. Laming, R., "Fabrication and characterization of low-loss optical fibers containing rare-earth ions," *Lightwave Technology, Journal of*, vol. 4, pp. 870-876, 1986.

[21] P. C. Becker, N. A. Olsson, and J. R. Simpson, *Erbium-doped Fiber Amplifiers: Fundamentals and Technology.* San Diego: Academic Press, 1999.

[22] R. H. Stolen, "Nonlinearity in fiber transmission," *Proceedings of the IEEE*, vol. 68, pp. 1232-1236, 1980.

[23] K. M. Sivalingam and S. Subramaniam, *Emerging optical network technologies architectures, protocols, and performance; Chapter 2*. New York: Springer Science+Business Media, Inc., 2005.

[24] S. G. Grubb, D. F. Welch, D. Perkins, C. L. A.-C. Liou, and S. M. A.-S. Melle, "OEO versus All-Optical Networks," presented at LEOS 2006.

[25] J. E. Flood, *Telecommunication Networks; Chapter 4*. London: Institute of Electrical Engineers, 1997.

[26] ITU-T, Rec G.8080, "Architecture of the Automatic Switched Optical Network (ASON)" International Telecommunications Union, 2006.

[27] D. Brungard (Ed), "RFC4258: Requirements for Generalized MPLS (GMPLS) Routing for Automatically Switched Optical Network (ASON)," Internet Engineering Task Force,

RFC4258, 2005. [Online] Available: http://www.ietf.org/rfc/rfc4258.txt. [Accessed Feb 9 2006].

[28] A. Jaiszczyk, "Automatically switched optical networks: benefits and requirements," Communications Magazine, IEEE, vol. 43, pp. S10-S15, 2005.

[29] S. Tomic, B. Statovci-Halimi, A. Halimi, W. Muellner, and J. Fruehwirth, "ASON and GMPLS - Overview and Comparison," *Photonic Network Communications*, vol. 7, pp. 111-130, 2004.

[30] S. D. Dods and T. B. Anderson, "Optical performance monitoring technique using delay tap asynchronous waveform sampling," presented at Optical Fiber Communication Conference, 2006 and the 2006 National Fiber Optic Engineers Conference, 2006.

[31] ITU-T Rec. G.7715/Y.1706, "Architecture and Requirements for Routing in the Automatically Switched Optical Networks," International Telecommunications Union, 2002.

[32] D. Oran (Ed), "OSI IS-IS Intra-domain Routing Protocol," Internet Engineering Task Force, RFC1142, 1990. [Online] Available: http://www.ietf.org/rfc/rfc1142.txt. [Accessed Feb 9 2006].

[33] E. W. Dijkstra, "A note on two problems in connexion with graphs," *Numerische Mathematik*, 1 (1959), S. 269–271.

[34] M. Garey and D. Johnson, *Computers and Intractability; Chapter 1*. San Francisco, CA: Freeman, 1979.

[35] T. Cormen, C. Leiserson, R. Rivest and C. Stein, *Introduction to Algorithms, 2nd ed; Chapter 25*. London: MIT Press, 2001.

[36] R. E. Bellman, "On a Routing Problem," *Quarterly of Applied Mathematics*, 16(1), pp.87-90, 1958.

[37] L. R. Ford, Jr and D. R. Fulkerson, *Flows in Networks*. Princeton, NJ: Princeton University Press, 1962.

[38] R. Ramaswami and K. N. Sivarajan, *Optical Networks: A Practical Perspective; Chapter 2*. San Francisco: Morgan Kaufmann, 2002.

[39] J. C. Whitaker, *The Electronics Handbook*. CRC Press, 2005.

[40] B. E. A. Saleh and M. C. Teich, *Fundamentals of Photonics; Chapter 12.2*. New York: John Wiley & Sons, 1991.

[41] F. Träger, *Springer handbook of lasers and optics; Section 8.8.8*, Springer, 2007.

[42] G. Keiser, *Optical Fiber Communications, 3rd ed; Chapter 3*. Boston: Mcgraw-Hill, 2000.

[43] I. H. Malitson, "Interspecimen Comparison of the Refractive Index of Fused Silica," *Journal of the Optical Society of America*, vol. 55, pp. 1205, 1965.

[44] M. Brodsky, N. J. Frigo, M. Boroditsky, and M. A.-T. Tur, M., "Polarization Mode Dispersion of Installed Fibers," *Lightwave Technology, Journal of*, vol. 24, pp. 4584-4599, 2006.

[45] H. Dutton, *Understanding Optical Communications; Chapter 2*. New York: Prentice Hall PTR, 1998.

[46] R. Ramaswami and K. N. Sivarajan, *Optical Networks: A Practical Perspective; Chapter 5*. San Francisco: Morgan Kaufmann, 2002.

[47] G. Keiser, *Optical Fiber Communications, 3rd ed; Chapter 12*. Boston: Mcgraw-Hill, 2000.

[48] D. A. Fishman and J. A. Nagel, "Degradations due to stimulated Brillouin scattering in multi-gigabit intensity-modulated fiber-optic systems," *Lightwave Technology, Journal of,* vol. 11, pp. 1721-1728, 1993.

[49] I. T. Monroy and E Tangdiongga, *Crosstalk in WDM Communication Networks*. Boston: Springer, 2002.

[50] R. Ramaswami and K. N. Sivarajan, "Routing and wavelength assignment in all-optical networks," *Networking, IEEE/ACM Transactions on*, vol. 3, pp. 489-500, 1995.

[51] D. Banerjee and B. Mukherjee, "Practical approaches for routing and wavelength assignment in large all-optical wavelength routed networks," *Selected Areas in Communications, IEEE Journal on*, vol. 14, pp. 903-908, June 1996.

[52] G. N. Rouskas, "Routing and Wavelength Assignment in Optical WDM Networks." *Wiley Encyclopedia of Telecommunications*, John Proakis, Ed, John Wiley & Sons, 2001.

[53] B. Mukherjee, *Optical WDM Networks; Chapter 2.7*. New York: Springer Science+Business Media, Inc., 2006.

[54] J. M. H. Elmirghani and H. T. Mouftah, "All-optical wavelength conversion: technologies and applications in DWDM networks," *Communications Magazine, IEEE*, vol. 38, pp. 86-92, 2000.

[55] I. Chlamtac, A. Ganz & G. Karmi, "Lightpath communications: an approach to high bandwidth optical WAN's," *Communications, IEEE Transactions on*, vol.40, no.7, pp.1171-1182, 1992.

[56] B. Mukherjee, *Optical WDM Networks; Chapter 7*. New York: Springer Science+Business Media, Inc., 2006.

[57] H. Zang, J. P. Jue and B. Mukherjee, "A review of routing and wavelength assignment approaches for wavelength-routed optical WDM networks," *Optical Networks Magazine*, vol. 1, pp. 47-60, 2000.

[58] R. Sabella, E.Iannone, M.Listanti, M. Berdusco and S. Binetti, "Impact of transmission performance on path routing in all-optical networks," *Lightwave Technology, Journal of,* vol. 16, pp. 1965-1972, 1993.

[59] B. Ramamurthy, D. Datta, H. Feng, J. P. Heritage, and B. Mukherjee, "Impact of Transmission Impairments on the Teletraffic Performance of Wavelength-Routed Optical Networks", *Lightwave Technology, Journal of*, vol 10, p.1713, 1999.

[60] B. Mukherjee, *Optical WDM Networks; Chapter 15*. New York: Springer Science+Business Media, Inc., 2006.

[61] R. Martinez, C. Pinart, J. Comellas, and G. Junyent, "Routing Issues in Transparent Optical Networks," presented at Transparent Optical Networks, 2006 International Conference on, 2006.

[62] S. Azodolmolky, M. Klinkowski, E. Marin, D. Careglio, J.-S. Pareta, I. Tomkos, "A survey on physical layer impairments aware routing and wavelength assignment algorithms in optical networks," *Computer Networks*, Volume 53, Issue 7, 13 May 2009, Pages 926-944.

[63] A. Jukan and G. Franzl, "Path selection methods with multiple constraints in service-guaranteed WDM networks," *Networking, IEEE/ACM Transactions on*, vol. 12, pp. 59-72, 2004.

[64] G. S. Pavani, L. G. Zuliani, H. Waldman, and M. Magalhães, "Distributed approaches for impairment-aware routing and wavelength assignment algorithms in GMPLS networks," *Computer Networks Challenges and Opportunities in Advanced Optical Networking*, vol. 52, pp. 1905-1915, 2008.

[65] Y. Huang, J. P. Heritage, and B. Mukherjee, "Connection provisioning with transmission impairment consideration in optical WDM networks with high-speed channels," *Lightwave Technology, Journal of*, vol. 23, pp. 982-993, 2005.

[66] B. Mukherjee, Y. Huang, and J. P. Heritage, "Impairment-aware routing in wavelength-routed optical networks," presented at Lasers and Electro-Optics Society, 2004. LEOS 2004. The 17th Annual Meeting of the IEEE, 2004.

[67] R. Cardillo, V. Curri, and M. Mellia, "Considering transmission impairments in wavelength routed networks," presented at Conference on Optical Network Design and Modeling, 2005.

[68] J. He, M. Brandt-Pearce, Y. Pointurier, and S. Subramaniam, "QoT-Aware Routing in Impairment-Constrained Optical Networks," presented at Global Telecommunications Conference, 2007.

[69] I. Tomkos, D. Vogiatzis, C. Mas, I. Zacharopoulos, A. Tzanakaki, and E. Varvarigos, "Performance engineering of metropolitan area optical networks through impairment constraint routing," *Communications Magazine, IEEE*, vol. 42, pp. S40-S47, 2004.

[70] C. Mas, D. Vogiatzis, and I. Tomkos, "Impairment aware routing in metropolitan area optical networks," presented at Transparent Optical Networks, 2004. Proceedings of 2004 6th International Conference on, 2004.

[71] P. Kulkarni, A. Tzanakaki, C. M. Machuka, and I. Tomkos, "Benefits of Q-factor based routing in WDM metro networks," presented at Optical Communication, 2005. ECOC 2005. 31st European Conference on, 2005.

[72] I. Tomkos, S. Sygletos, A. Tzanakaki and G. Markidis, "Impairment Constraint Based Routing in Mesh Optical Networks," presented at Optical Fiber Communication Conference, 2007 and the 2007 National Fiber Optic Engineers Conference, 2007.

[73] V. Anagnostopoulos, C. T. Politi, C. Matrakidis, and A. Stavdas, "Physical layer impairment aware wavelength routing algorithms based on analytically calculated constraints," *Optics Communications*, vol. 270, pp. 247-254, 2007.

[74] C. Politi, V. Anagnostopoulos, C. Matrakidis, and A. Stavdas, "Physical layer impairment aware routing algorithms based on analytically calculated Q-factor," presented at Optical Fiber

Communication Conference, 2006 and the 2006 National Fiber Optic Engineers Conference, 2006.

[75] J. F. Martins-Filho, C. J. A. Bastos-Filho, S. C. Oliveira, E. A. J. Arantes, E. Fontana and F. D. Nunes, "Novel routing algorithm for optical networks based on noise figure and physical impairments", in *Proceedings of 29th European Conference on Optical Communication*, 2003, pp. 856-857, 2003.

[76] J. F. Martins-Filho, C. J. A. Bastos-Filho, E. A. J. Arantes, S. C. Oliveira, L. D. Coelho, J. P. G. de Oliveira, R. G. Dante, E. Fontana, and F. D. Nunes, "Novel routing algorithm for transparent optical networks based on noise figure and amplifier saturation," presented at Microwave and Optoelectronics Conference, 2003.

[77] H. A. Pereira, D. A. R. Chaves, C. J. A. Bastos-Filho, and J. F. Martins-Filho, "Impact of physical layer impairments in all-optical networks," presented at Microwave and Optoelectronics Conference, 2007.

[78] D. A. R. Chaves, D. O. Aguiar, H. A. Pereira, C. J. A. Bastos-Filho, and J. F. Martins-Filho, "Novel physical impairments aware adaptive weight function for routing in all optical networks," presented at Microwave and Optoelectronics Conference, 2007.

[79] A. Marsden, A. Maruta, and K.-i. Kitayama, "FWM-Aware Dynamic Routing and Wavelength Assignment for Wavelength-Routed Optical Networks," *IEICE Trans Commun*, vol. E91-B, pp. 2145-2151, 2008.

[80] A. Morea, N. Brogard, F. Leplingard, J. Antona, T. Zami, B. Lavigne and D. Bayart, "QoT function and A* routing: an optimized combination for connection search in translucent networks," in *Optical Network, Journal of*, vol. 7, pp. 42-61, 2008.

[81] J. C. Li, K. Hinton, S. D. Dods, P. M. Farrell, "Optical impairment outage computation, " in *Optics Express*, vol. 16, issue 14, pp. 10529-10534, 2008.

[82] J. C. Li, K. Hinton, S. D. Dods, P. M. Farrell, "Novel Outage Probability Based RWA Algorithm," presented at presented at Optical Fiber Communication Conference, 2008 and the 2008 National Fiber Optic Engineers Conference, 2008.

[83] J. C. Li, K. Hinton, S. D. Dods, P. M. Farrell, M. Ivanovich and P. Fitzpatrick, "Outage and Capacity based Path Selection in Optical Networks," Optical Communication, 2007. ECOC 2007. 33rd European Conference on, 2007.

[84] J. C. Li, K. Hinton, S. D. Dods, P. M. Farrell, "Enabling ASON Routing via Novel Signal Quality Metrics," presented at Optical Fiber Communication Conference, 2007 and the 2007 National Fiber Optic Engineers Conference, 2007.

[85] J. Li, K. Hinton, S. Dods, P. Farrell, "Automatically Switched Optical Network Path Selection Using Eye Closure Penalty," Australian Telecommunication Networks and Applications Conference, 2006.

[86] D. Derickson, *Fiber Optic Test and Measurement*. Upper Saddle River, N.J: Prentice Hall, 1997.

[87] G. Keiser, *Optical Fiber Communications, 3rd ed; Chapter 8*. Boston: Mcgraw-Hill, 2000.

[88] G. Keiser, *Optical Fiber Communications, 3rd ed; Chapter 6*. Boston: Mcgraw-Hill, 2000.

[89] G. Keiser, *Optical Fiber Communications, 3rd ed; Chapter 13*. Boston: Mcgraw-Hill, 2000.

[90] G. P. Agrawal, *Fiber-Optic Communications Systems, Third Edition; Chapter 4*. New York: John Wiley & Sons, Inc., 2002.

[91] P. B. Kahn, *Mathematical Methods for Scientists and Engineers; Chapter 2*. Courier Dover Publications, 2004.

[92] R. Ramaswami and K. N. Sivarajan, *Optical Networks: A Practical Perspective; Chapter 4.* San Francisco: Morgan Kaufmann, 2002.

[93] P. Kumar, M. Win, H. Lu and C. Geoghiades, "Error-Control Coding Techniques and Applications" in *Optical Fiber Telecommunications IVB: Systems and Impairments*, I. Kaminow, T. Li, Eds, Academic Press, 2002.

[94] A. F. Elrefaie, R. E. Wagner, D. A. Atlas, and D. G. Daut, "Chromatic dispersion limitations in coherent lightwave transmission systems," *Lightwave Technology, Journal of*, vol. 6, pp. 704-709, 1988.

[95] K. E. Cornick, M. Boroditsky, S. Finch, S. D. Dods, and P. M. Farrell, "Experimental comparison of PMD-induced system penalty models," *Photonics Technology Letters, IEEE*, vol. 18, pp. 1149-1151, 2006.

[96] S. D. Dods and T. B. Anderson, "Optical performance monitoring technique using delay tap asynchronous waveform sampling," presented at Optical Fiber Communication Conference, 2006 and the 2006 National Fiber Optic Engineers Conference, 2006.

[97] VPI TransmissionMaker WDM, http://www.vpiphotonics.com/ (2006).

[98] H. Rosenfeldt and E. Brinkmeyer, "PMD-compensation techniques," *Optical and Fiber Communications Research, Journal of*, vol. 2, pp. 32-55, 2005.

[99] G. Agrawal, *Lightwave technology; Chapter 6.* John Wiley and Sons, 2005.

[100] G. Agrawal, *Nonlinear fiber optics; Chapter 7*. Academic Press, 2007.

[101] T. Wuth, M. W. Chbat, V. F. Kamalov, "Multi-rate (100G/40G/10G) Transport Over Deployed Optical Networks," presented at Optical Fiber Communication Conference, 2008 and the 2008 National Fiber Optic Engineers Conference, 2008.

[102] P. J. Winzer and R.-J. Essiambre, "Advanced optical modulation formats," in *Optical Fiber Telecommunications V B*, I. Kaminow, T. Li, A. E. Willner, Eds, Academic Press, 2008.

[103] P. J. Winzer and R.-J. Essiambre, "Advanced Modulation Formats for High-Capacity Optical Transport Networks," *Lightwave Technology, Journal of*, vol. 24, pp. 4711-4728, 2006.

[104] A. H. Gnauck and P. J. Winzer, "Optical phase-shift-keyed transmission," *Lightwave Technology, Journal of*, vol. 23, pp. 115-130, 2005.

[105] C. Xu, X. Liu, L.F. Mollenauer and X. Wei, "Comparison of return-to-zero differential phase-shift keying and ON-OFF keying in long-haul dispersion managed transmission," *Photonics Technology Letters, IEEE*, vol. 15, pp. 617-619, 2003.

[106] Z. Pan, Y. Wang, Y. Song, R. Motaghian, S. Havstad and A. Willner, "Monitoring chromatic dispersion and PMD impairments in optical differential phaseshift-keyed (DPSK) systems," presented at Optical Fiber Communications Conference, 2003. OFC 2003.

[107] G. Bosco and P. Poggiolini, "On the Q factor inaccuracy in the performance analysis of optical direct-detection DPSK systems," *Photonics Technology Letters, IEEE*, vol. 16, pp. 665-667, 2004.

[108] X. Wei, X. Liu, and C. Xu, "Q-Factor in Numerical Simulations of DPSK With Optical Delay Demodulation," [Online] Available: http://arxiv.org/ftp/physics/papers/0304/0304002.pdf.

[109] H. Bulow, "System outage probability due to first- and second-order PMD," *Photonics Technology Letters, IEEE*, vol. 10, pp. 696-698, 1998.

[110] P. Lu, L. Chen, and X. Bao, "System outage probability due to the combined effect of PMD and PDL," *Lightwave Technology, Journal of*, vol. 20, pp. 1805-1808, 2002.

[111] M. Brodsky, N. J. Frigo, M. Boroditsky, and M. A.-T. Tur, M., "Polarization Mode Dispersion of Installed Fibers," *Lightwave Technology, Journal of*, vol. 24, pp. 4584-4599, 2006.

[112] H. Kogelnik and P. J. Winzer, "PMD Outage Probabilities Revisited," presented at Optical Fiber Communications Conference, 2007. OFC 2007.

[113] H. Kogelnik, R. M. Jopson and L. E. Nelson "Polarization-Mode Dispersion," in *Optical Fiber Telecommunications IVB: Systems and Impairments*, I. Kaminow, T. Li, Eds, Academic Press, 2002.

[114] H. C. Ji, J. H. Lee and Y. C. Chung, "System outage probability due to dispersion variation caused by seasonal and regional temperature variations," presented at Optical Fiber Communication Conference, 2005. OFC 2005.

[115] J.-K. K. Rhee, "Novel Statistical OSNR Budgeting for Optically Amplified DWDM Circuits With Polarization-Dependent Loss," *Photonics Technology Letters, IEEE*, vol. 19, pp. 354-356, 2007.

[116] M. I. Hayee and A. E. Willner, "Transmission penalties due to EDFA gain transients in add-drop multiplexed WDM networks," *Photonics Technology Letters, IEEE*, vol. 11, pp. 889-891, 1999.

[117] D. C. Kilper, R. Bach, D. J. Blumenthal, D. Einstein, T. Landolsi, L. Ostar, M. Preiss and A. E. Willner, "Optical performance monitoring," *Lightwave Technology, Journal of*, vol. 22, pp. 294-304, 2004.

[118] A. Walter and G. S. Schaefer, "Chromatic dispersion variations in ultra-long-haul transmission systems arising from seasonal soil temperature variations," presented at Optical Fiber Communication Conference and Exhibit, 2002. OFC 2002.

[119] N. P. Cheremisinoff, *Practical statistics for engineers and scientists: Chapter 2*. CRC Press, 1987.

[120] F. Cugini, P. Ghelfi, A. Bogoni, L. Valcarenghi and P. Castoldi, "RWA for Mitigating Power Excursion Effects in EDFA-based all-Optical Metro Networks," presented at Optical Communication, 2007. ECOC 2007. 33rd European Conference on, 2007.

[121] A. Mecozzi and M. Shtaif, "The statistics of polarization-dependent loss in optical communication systems," *Photonics Technology Letters, IEEE*, vol. 14, pp. 313-315, 2002.

[122] A. Papoulis, *Probability, Random Variables and Stochastic Processes: Chapter 5*, McGraw-Hill, 2002.

[123] A. K. Srivastava and Y. Sun, "Advances in Erbium-Doped Fiber Amplifiers," in *Optical Fiber Telecommunications IVB: Systems and Impairments*, I. Kaminow, T. Li, Eds, Academic Press, 2002.

[124] ITU-T Study Group 2, *Teletraffic Engineering Handbook*, [Online] Available: http://www.com.dtu.dk/teletraffic/handbook/telenook.pdf.

[125] S. M. Ross, *Introduction to probability model: Chapter 5*. Academic Press, 2007.

[126] M. Kijima, *Markov processes for stochastic modelling*: *Chapter 1*. CRC Press, 1997.

[127] L. Kleinrock, Queueing *Systems: Theory, Volume I*, Wiley, 1975.

[128] R. G. Gallager, *Discrete stochastic processes: Chapter 2*. Springer, 1996.

[129] F. Kelly, "Loss Networks," *The Annals of Applied Probability*, vol. 1, pp. 319-378, 1991.

[130] S. Subramaniam, M. Azizoglu and A. K. Somani, "All-optical networks with sparse wavelength conversion," *Networking, IEEE/ACM Transactions on*, vol. 4, pp. 544-557, 1996.

[131] A. Sridharan and K. N. Sivarajan, "Blocking in all-optical networks," *Networking, IEEE/ACM Transactions on*, vol. 12, pp. 384-397, 2004.

[132] J. Xiong, W. Gong and C. Qiao, "An effective method for blocking performance analysis of WDM all-optical networks," *Lightwave Technology, Journal of*, vol. 21, pp. 1421-1434, 2003.

[133] R. A. Barry and P. A. Humblet, "Models of blocking probability in all-optical networks with and without wavelength changers," *Selected Areas in Communications, IEEE Journal on*, vol. 14, pp. 858-867, 1996.

[134] Y. Zhu, G. N. Rouskas, H. G. Perros, "A path decomposition approach for computing blocking probabilities in wavelength-routing networks," *Networking, IEEE/ACM Transactions on*, vol. 8, pp. 747-762, 2000.

[135] Y. Pointurier, M. Brandt-Pearce and S. Subramaniam, "Analysis of Blocking Probability in Noise and Crosstalk Impaired All-Optical Networks," presented at INFOCOM 2007.

[136] J. L. Miller and E. Friedman, *Optical communications rules of thumb: Chapter 6.* McGraw-Hill Professional, 2002.

[137] J. Zheng, H. T. Mouftah , *Optical WDM networks: Chapter 3.* Wiley-IEEE, 2004.

[138] P. W. Wan, D. Remedios, D. Jin and P. C. Chimfwembe, "Channel identification in communications networks" Canadian Patent 2 358 382, Oct. 5, 2001.

[139] AARNet network, [Online] Available: http://www.aarnet.edu.au/aarnet3.aspx, 2009.

[140] Australian Bureau of Statistics, "3218.0 - Regional Population Growth, Australia, 2007-08," [Online] Available: http://www.abs.gov.au/AUSSTATS/abs@.nsf/DetailsPage/3218.02007-08?OpenDocument.

University Library

A gateway to Melbourne's research publications

Minerva Access is the Institutional Repository of The University of Melbourne

Author/s:
Li, Jonathan Chi-Fai

Title:
Eye closure penalty based signal quality metric for intelligent all-optical networks

Date:
2009

Citation:
Li, J. C. (2009). Eye closure penalty based signal quality metric for intelligent all-optical networks. PhD thesis, Department of Electrical and Electronic Engineering, The University of Melbourne.

Publication Status:
Unpublished

Persistent Link:
http://hdl.handle.net/11343/35290

File Description:
Eye closure penalty based signal quality metric for intelligent all-optical networks

Terms and Conditions:
Terms and Conditions: Copyright in works deposited in Minerva Access is retained by the copyright owner. The work may not be altered without permission from the copyright owner. Readers may only download, print and save electronic copies of whole works for their own personal non-commercial use. Any use that exceeds these limits requires permission from the copyright owner. Attribution is essential when quoting or paraphrasing from these works.